

CHARACTERIZING LIQUID-ORDERED AND LIQUID-DISORDERED
PHASE PROPERTIES AND INTERFACES

A Dissertation

Presented to the Faculty of the Graduate School

of Cornell University

In Partial Fulfillment of the Requirements for the Degree of

Doctor of Philosophy

by

Rebecca Danae Usery

December 2018

© 2018 Rebecca Danae Usery

CHARACTERIZING LIQUID-ORDERED AND LIQUID-DISORDERED PHASE PROPERTIES AND INTERFACES

Rebecca Danae Usery, Ph. D.

Cornell University 2018

Specialized lipid microdomains, or "membrane rafts", are thought to be involved in many plasma membrane events like signaling, protein sorting, and viral entry and exit. The size and dynamics of membrane domains is governed by the energy penalty for domain interface, called line tension, making it an important quantity in the discussion of compartmentalization of functions for signaling at the plasma membrane via possible phase separation. Cells must also be able to maintain and change membrane shape. Curvature of the membrane can be influenced by lateral heterogeneities as well as a means to induce lateral heterogeneity. Thus both the line tension and membrane bending rigidity are important quantities for understanding "raft" behavior.

Mixtures of high-melting lipid, low-melting lipid(s), and cholesterol exhibit a region of liquid-ordered (Lo) + liquid-disordered (Ld) phase coexistence analogous to raft + non-raft behavior in cells. Line tension depends strongly on the lipids comprising the mixture, with a minimal line tension required for visible phase domains to form. I have shown that line tension, calculated in terms of pairwise lipid interactions, agrees with experimental values. I measured the bending modulus of the respective coexisting Ld and Lo phases and found that in the presence of near physiological amounts of transmembrane peptides the more ordered domains are not necessarily more rigid and may actually form highly curved structures more readily. As

cholesterol is increased and the coexisting phases become more compositionally similar, I found a slight rigidifying effect of cholesterol on Ld phases and a dramatic decrease in Lo rigidity. In a model with coexisting nanoscopic phases, I found that the continuous phase determines the membrane rigidity.

BIOGRAPHICAL SKETCH

Rebecca Usery grew up on a farm in Cave Springs, Arkansas. As a 4-Her, she volunteered over 1000 hours in community service projects. She was elected the Arkansas 4-H State President in 2008. At Bentonville High School, she served on student council, ran cross country, and played trumpet in the marching band. She graduated with High Honors in the top 10 of her class of 690 from Bentonville High School in 2008.

Rebecca went on to the University of Arkansas in Fayetteville where she studied Chemistry and Mathematics. She studied chloroplast signal recognition particle structure and stability using multi-dimensional nuclear magnetic resonance in the laboratory of Dr. T. K. S. Kumar. Rebecca graduated from the University of Arkansas with magna cum laude honors, receiving her Bachelors of Science in Chemistry and her Bachelors of Arts in Mathematics in May 2013.

Rebecca began her doctoral studies at Cornell University in 2013. She joined the lab of Dr. Gerald Feigenson. She received a Graduate Research Fellowship from the National Science Foundation.

To Ella Patricia Simpson

ACKNOWLEDGMENTS

I would like to thank my advisor Dr. Gerald Feigenson for the years of guidance and the opportunity to conduct research in his lab. Not many advisors make the time for listening to all the little problems that unavoidably crop up in performing research. His technical and editorial advice was essential to the completion of this dissertation.

I would like to thank my committee, Dr. Gerald Feigenson, Dr. Volker Vogt, and Dr. Warren Zipfel, for their input and a critical reading of this thesis. I appreciate the support of Dr. Volker Vogt and Dr. Bill Brown in difficult times as well.

These works could not have been made complete without the contributions of others. Discussions with Dr. David Ackerman were vital to getting my projects started. I'm grateful for the kindness and willingness to help of the extraordinarily busy Dr. Milka Doktorova. I was fortunate to work alongside Dr. Thais Enoki, whose collaboration and friendship I value immensely.

The work in Chapter 2 was made complete with collaboration with other groups. The guidance and collaboration of Dr. Roger Keoppe III and Dr. Denise Greathouse of the University of Arkansas were invaluable for our experiments with transmembrane peptides. The missing piece for that publication was circular dichroism and oriented circular dichroism that Dr. Francisco Barrera and Vanessa Nguyen graciously agreed to do and interpret for us.

Chapter 3 was a very large undertaking involving the efforts of Dr. Thais Enoki, Sanjula Wickramasinghe, Dr. Michael Weiner, Dr. Jacky Tsai, Mary Kim, Thomas Torng, Dr. David Ackerman, and Dr. Fred Heberle. Dr. Thais Enoki and I would not have been able to produce a cohesive manuscript without the guidance of Dr. Fred Heberle and Dr. David Ackerman. I owe the derivation in Chapter 4 to the input of Shinya Hiraki.

This work was supported by U.S. National Science Foundation grant No. MCB-1410926, U.S. National Institutes of Health grant No. GM105684, and the National Science Foundation Graduate Research Fellowship Program under grant No. DGE-1144153ESR.

The support of my family and in-laws has meant so much to me. I would also like to thank Gus Usery for being a good listener and endlessly upbeat. My better half, Jake Usery, deserves a very special thank you for his support and understanding throughout my graduate studies.

TABLE OF CONTENTS

BIOGRAPHICAL SKETCH.....	v
DEDICATION.....	vi
ACKNOWLEDGEMENTS.....	vii
TABLE OF CONTENTS.....	ix
LIST OF FIGURES.....	xiii
LIST OF TABLES.....	xvi
LIST OF ABBREVIATIONS.....	xvii
CHAPTER 1: INTRODUCTION.....	1
1.1 Overview.....	1
1.2 Lipid bilayers.....	2
1.3 Lipid raft hypothesis.....	3
1.4 Lipid bilayer phases.....	4
1.4.1 Lipid bilayer phase diagrams.....	5
1.5 Membrane domain size.....	8
1.6 Line tension.....	9
1.7 Membrane bending rigidity.....	12
1.8 Model transmembrane peptides.....	16
1.9 Thesis outline.....	17
1.10 References.....	19
CHAPTER 2: MEMBRANE BENDING MODULI OF COEXISTING LIQUID PHASES CONTAINING TRANSMEMBRANE PEPTIDE	
2.1 Abstract.....	29
2.2 Introduction.....	30
2.3 Materials and methods.....	33
2.3.1 Materials.....	33

2.3.2	GUV preparation.....	34
2.3.3	Membrane rigidity measurements.....	35
2.3.4	FRET trajectories for phase boundaries and K _p determination.....	36
2.3.5	Circular dichroism.....	37
2.3.6	Oriented circular dichroism.....	37
2.3.7	Electron paramagnetic resonance (EPR).....	38
2.4	Results.....	38
2.4.1	Coexisting L _d and L _o at the lower cholesterol tieline.....	39
2.4.2	High-cholesterol tieline L _d and L _o	50
2.4.3	Difference in L _d and L _o bending moduli of various models.....	53
2.5	Discussion.....	56
2.5.1	Coexisting L _d and L _o at the lower cholesterol tieline.....	56
2.5.2	GWALP23 incorporation and orientation in the bilayer.....	58
2.5.3	High-cholesterol tieline L _d and L _o	60
2.5.4	Increased membrane bending rigidity with GWALP23.....	61
2.5.5	Simplified mixtures are not representative of coexisting phases.....	62
2.6	Conclusions.....	63
2.7	Author Contributions.....	63
2.8	References.....	64
 CHAPTER 3: LINE TENSION CONTROLS LIQUID-DISORDERED + LIQUID- ORDERED DOMAIN SIZE TRANSITION IN LIPID BILAYERS		
3.1	Abstract.....	71
3.2	Introduction.....	72
3.3	Materials and methods.....	74
3.3.1	Materials.....	74
3.3.2	Composition conventions used.....	76

3.3.3	GUV preparation and phase morphology determination.....	77
3.3.4	Line tension measurements.....	78
3.3.5	Bending energy measurements.....	79
3.3.6	Partition coefficient measurements.....	80
3.3.7	Model for calculating equilibrium domain size.....	82
3.3.8	Nanodomain size measurements.....	84
3.3.9	Molecular dynamics simulations.....	85
3.4	Results	
3.4.1	Domain size exhibits an abrupt transition with composition that is correlated with line tension.....	88
3.4.2	Physical and chemical properties of Ld and Lo phases do not change at the abrupt domain size transition.....	92
3.4.3	Competing interactions could drive the domain size transition.....	96
3.4.4	Nanoscopic domains are not significantly influenced by vesicle size, but have a complex shape.....	99
3.5	Discussion.....	101
3.5.1	The domain size transition is correlated with line tension.....	102
3.5.2	Properties of Ld and Lo domains do not change abruptly despite the abrupt domain size transition.....	104
3.5.3	Competition between line tension and dipole repulsion drives the domain size transition.....	106
3.5.4	Hybrid and non-hybrid lipids have similar line activity.....	108
3.5.5	Nanodomains have a complex morphology.....	109
3.6	Summary and conclusion.....	110
3.7	Author contributions.....	111
3.8	References.....	112

CHAPTER 4: CALCULATION OF LIQUID-DISORDERED/LIQUID-ORDERED LINE TENSION FROM PAIRWISE LIPID INTERACTIONS	
4.1 Abstract.....	118
4.2 Introduction.....	119
4.3 Materials and Methods.....	122
4.3.1 Materials.....	122
4.3.2 Model.....	123
4.3.3 GUV preparation.....	128
4.3.4 Line tension measurements.....	129
4.4 Results.....	130
4.5 Discussion.....	138
4.6 Conclusion.....	145
4.7 Author Contributions.....	145
4.8 References.....	146
APPENDIX A: SUPPORTING MATERIAL FOR CHAPTER 2.....	151
APPENDIX B: SUPPORTING MATERIAL FOR CHAPTER 3.....	162
APPENDIX C: SUPPORTING MATERIAL FOR CHAPTER 4.....	202
APPENDIX D: BENDING RIGIDITY OF MEMBRANES CONTAINING NANODOMAINS IS DETERMINED BY THE PERCOLATING PHASE.....	212

LIST OF FIGURES

Figure 1.1	General phase diagram for highT _m /lowT _m /chol.....	7
Figure 1.2	Tetrahedral diagram depicting ρ	9
Figure 1.3	Thickness mismatch in a simulated Ld/ Lo bilayer.....	10
Figure 1.4	Fluctuating domain illustration.....	11
Figure 1.5	Model transmembrane peptide, F ^{4,5} GWALP23.....	17
Figure 2.1	Presence of GWALP23 does not change phase boundaries.....	42
Figure 2.2	GWALP23 partitions favorably into the Ld phase.....	44
Figure 2.3	GWALP23 increases the membrane bending rigidity of the Ld phase.....	46
Figure 2.4	The ratio of GWALP23:lipid does not change during GUV preparation.....	47
Figure 2.5	Structure and orientation of GWALP23 in DSPC/DOPC/chol Ld and Lo.....	49
Figure 2.6	The presence of 2 mol% GWALP23 does not change phase boundaries of DSPC/DOPC/chol at high cholesterol fraction	52
Figure 2.7	GWALP23 partitions into the Ld phase at high cholesterol fraction...	52
Figure 2.8	GWALP23 increases the rigidity of the Ld phase at the high cholesterol tieline for DSPC/DOPC/chol.....	53
Figure 2.9	Bending moduli of Ld and Lo phases in lipid-only mixtures.....	55
Figure 3.1	Phase diagrams and phase morphologies in four-component mixtures.....	73
Figure 3.2	Morphology of coexisting Ld + Lo domains changes with ρ	90
Figure 3.3	Line tension increases in a ρ trajectory.....	92
Figure 3.4	Lo and Ld bending moduli do not show abrupt transitions in a ρ	

	trajectory.....	93
Figure 3.5	Probe partition coefficients do not show abrupt transitions along a ρ trajectory.....	95
Figure 3.6	A model of competing interactions describes the domain size transition.....	98
Figure 3.7	SANS reveals domain size in the nanoscopic regime along ρ	100
Figure 3.8	Simulated nanodomains have a complex morphology.....	101
Figure 4.1	Phase diagram of DSPC/DOPC/chol.....	122
Figure 4.2	Ld/Lo bilayer contacting process.....	125
Figure 4.3	Pairwise interaction energies.....	134
Figure 4.4	Measured and calculated values of line tension.....	136
Figure 4.5	Relative contribution of terms in line tension calculations.....	138
Figure A.1	Compositions used for bending moduli measurements.....	153
Figure A.2	GWALP23 partitions into the Ld phase of mixtures with coexisting nanoscopic Ld + Lo domains.....	155
Figure A.3	C12:0 DiI fluorescence is directly proportional to the lipid concentration.....	156
Figure A.4	EPR spectra for Ld and Lo.....	157
Figure A.5	FAST DiO K_p decreases with increased cholesterol content.....	159
Figure A.6	GWALP23 increases the membrane bending rigidity of the DOPC membranes.....	160
Figure B.1	Snapshots of domains over time.....	169
Figure B.2	Light-induced effects can be detected by measuring line tension over time.....	170
Figure B.3	Domain exhibiting light induced artifacts.....	171
Figure B.4	Line tension measurement cooling controls.....	172

Figure B.5	DSPC/DPhPC/DLPC/chol line tension is independent of domain size and GUV size.....	173
Figure B.6	SANS reveals that nanodomain size is independent of vesicle size.....	175
Figure B.7	Size and connectivity of domains increases as ρ increases.....	177
Figure B.8	Fluctuation spectroscopy edge detection.....	179
Figure B.9	Phase diagram of bSM/POPC/chol and bSM/DOPC/chol.....	181
Figure B.10	Fluorescence self-quenching with increasing dye concentration.....	182
Figure B.11	Fluorescence emission of Bodipy-PC in bSM/POPC/chol.....	183
Figure B.12	Intensity profile measurements on GUVs.....	185
Figure B.13	ESR spectra change little along ρ for both Ld and Lo.....	187
Figure B.14	The direction and location of carbonyl dipoles in a bilayer.....	189
Figure B.15	Analytical solution for the pair-distance distribution function of a disk.....	194
Figure B.16	Sensitivity of the continuum model to dielectric constant.....	198
Figure B.17	Sensitivity of the continuum model to parameter values.....	199
Figure C.1	PSM/DOPC/chol trajectory.....	209
Figure C.2	PSM/POPC/chol trajectory.....	210
Figure D.1	Two-phase region of DSPC/POPC/chol.....	213
Figure D.2	DSPC/POPC/chol bending moduli traversing the two-phase region.....	215

LIST OF TABLES

Table 2.1	Bending moduli of Ld and Lo phases.....	40
Table 2.2	Bending moduli of high cholesterol Ld and Lo phases.....	51
Table 3.1	ESR reveals small changes of Ld and Lo phases along the domain size transition.....	96
Table 4.1	Partitioning of lipids in various mixtures.....	133
Table A.1	Emission (λ_{ex}) and excitation (λ_{em}) wavelengths for individual dye fluorescence.....	154
Table A.2	Emission (λ_{ex}) and excitation (λ_{em}) wavelengths for FRET pairs.....	154
Table A.3	DSPC/DOPC/chol Ld and Lo order parameters.....	158
Table B.1	Fast cooling techniques used in different four-lipid systems.....	164
Table B.2	Sample composition used in the line tension measurements for six different lipid mixtures.....	166
Table B.3	Sample composition used in bending modulus measurements.....	178
Table B.4	Parameters used in the dipole-dipole repulsion simulations.....	197
Table C.1	DSPC/DOPC/chol parameter sensitivity.....	206
Table C.2	DSPC/POPC/chol parameter sensitivity.....	206
Table C.3	bSM/DOPC/chol parameter sensitivity.....	206
Table C.4	bSM/POPC/chol parameter sensitivity.....	207
Table C.5	PSM/DOPC/chol parameter sensitivity.....	207
Table C.6	PSM/POPC/chol parameter sensitivity.....	207

LIST OF ABBREVIATIONS

16:0,18:2PC	1-palmitoyl-2-linoleoyl- <i>sn</i> -glycero-3-phosphocholine
16PC	1-palmitoyl-2-(16-doxyl stearoyl) phosphatidylcholine
7PC	1-palmitoyl-2-(7-doxyl stearoyl) phosphatidylcholine
BODIPY-PC	2-(4,4-difluoro-5,7-dimethyl-4-bora-3a,4adiaza-s-indacene-3-pentanoyl)-1-hexadecanoyl- <i>sn</i> -glycero-3-phosphocholine
bSM	brain sphingomyelin
C12:0 DiI	1,1'-didodecyl-3,3,3',3'-tetramethylindocarbocyanine perchlorate
CD	circular dichroism
chol	cholesterol
DHE	ergosta-5,7,9(11),22-tetraen-3 β -ol
DLPC	1,2-dilauroyl- <i>sn</i> -glycero-3-phosphocholine
DOPC	1,2-dioleoyl- <i>sn</i> -glycero-3-phosphocholine
DPhPC	1,2-diphytanoyl- <i>sn</i> -glycero-3-phosphocholine
DPPC	1,2-dipalmitoyl- <i>sn</i> -glycero-3-phosphocholine
DSPC	1,2-distearoyl- <i>sn</i> -glycero-3-phosphocholine
DUPC	1,2-dilinoleoyl- <i>sn</i> -glycero-3-phosphocholine
EDTA	ethylenediaminetetraacetic acid
EPR	electron paramagnetic resonance
eSM	egg sphingomyelin
F ^{4,5} GWALP23	acetyl-GGAFF(LA) ₆ LWLAGA-ethanolamide
FAST DiO	benzoxazolium, 3-(9,12-octadecadienyl)-2-[3-[3-(9,12-octadecadienyl)-2(3H)-benzoxazolylidene]-1-propenyl]-, perchlorate

FRET	Forster resonance energy transfer
GUV	giant unilamellar vesicle
highT _m	high melting temperature lipid
L β	gel (phase)
L _d	liquid-disordered (phase)
L _o	liquid-ordered (phase)
lowT _m	low melting temperature lipid
MD	molecular dynamics
PC	phosphatidylcholine
PG	phosphatidylglycerol
PIPES	piperazine-N,N'-bis(2-ethanesulfonic acid)
PM	plasma membrane
POPC	1-palmitoyl-2-oleoyl- <i>sn</i> -glycero-3-phosphocholine
PSM	N-palmitoyl-D- <i>erythro</i> -sphingosylphosphorylcholine
PUPC	1-palmitoyl-2-linoleoyl- <i>sn</i> -glycero-3-phosphocholine
OCD	oriented circular dichroism
SDPC	1-stearoyl-2-docosahexaenoyl- <i>sn</i> -glycero-3-phosphocholine
SM	spingomyelin
SOPC	1-stearoyl-2-oleoyl- <i>sn</i> -glycero-3-phosphocholine
TOE	Tryptophan oleoyl ester

Chapter 1:

Introduction

1.1 Overview

This work examines the properties of biomembrane models and domain interfaces. Our investigations of liquid-disordered (Ld) and liquid-ordered (Lo) properties include studies of partitioning of lipophilic probes, phase order, bending rigidity, as well as the partitioning, incorporation, and orientation of a model transmembrane peptide.

Membrane bending rigidity represents the energy that must be overcome for the many processes and structures requiring curvature. It is a significant factor in the kinetics of budding events and also has a role in membrane lateral heterogeneity. While much has been done prior to this work in the study of the bending rigidity of one- or two-component membranes, these mixtures do not reflect the compositions of coexisting Ld and Lo phases. Comparisons of coexisting phases prior to this work also did not extend to how a protein component alters the rigidity difference between phases, particularly in the presence of physiological fractions of a protein component. The elastic properties of a complex mixture more closely resembling the plasma membrane, which are fundamental for understanding events requiring curvature, are

introduced in this work. The energy penalty for interface, line tension, governs the size and dynamics of membrane domains. Domain size in the plasma membrane has profound implications for membrane signaling. This work explores how line tension relates to phase morphology and models for interactions that both contribute to and counter line tension.

In this chapter, I provide background information for Chapters 2-5: an introduction to lipid bilayers, plasma membrane rafts, lipid phase behavior, line tension, and membrane bending rigidity. The chapter ends with an outline of the particular questions addressed by this work.

1.2 Lipid bilayers

Membrane-forming lipids are amphipathic molecules consisting generally of a hydrophilic headgroup and two hydrophobic tails. The head groups are of varying shapes and charge states. The hydrophobic tails are fatty acid chains of varying lengths and degrees of unsaturation. These lipids form various structures depending on the lipid shape as defined by the relative size of the head group and chains. Of these structures, bilayers can spontaneously form in which head groups interact with external water molecules and shield the fatty acid chains from unfavorable interactions with water. This propensity for forming bilayers makes them ideal physical barriers for both delineating the cell and compartmentalizing functions at the subcellular level. However, their function extends far beyond that of a barrier; they must integrate

signals, and dynamically facilitate necessary functions like vesicular transport and protein sorting.

Sterols are an exception to the common lipid description, and are a common feature of cell membranes. In animal cells cholesterol levels increase throughout the secretory pathway, culminating at the plasma membrane. Animal cell plasma membranes are approximately 40 % cholesterol, making it the most abundant plasma membrane lipid (1). Cholesterol has a complex ring structure and a single hydroxyl group inadequate to shield the hydrophobic rings from water. Thus cholesterol interacts favorably with phospholipids- the flat face of the molecule packs well against saturated chains, and the headgroup shields the cholesterol, like an umbrella (2). The shielding required by cholesterol decreases the area per lipid, thereby also increasing the thickness of the membrane.

1.3 Lipid raft hypothesis

The idea that compartmentalization of the plasma membrane would facilitate the many necessary functions of the plasma membrane has been termed the “raft hypothesis”. Specialized domains in the membrane enriched in sphingolipid, or “rafts”, are thought to regulate protein localization and membrane bioactivity (3–5). The origin of this idea dates back to analyses of epithelial cell membranes in which the microvilli were found to be enriched with glycosphingolipids, or “raft” lipids and the basolateral sides were found to contain more phosphatidylcholine, or “non-raft” lipids (6). This organization has a role in trafficking components to the plasma membrane;

there are two distinct paths from the trans Golgi network to the plasma membrane, and the direct path is via raft-like carriers(7, 8). Assemblies nanometers in size have been detected in the plasma membrane by a variety of methods (9–14). In addition, cholesterol-dependent, micrometer-scale phase separation can be observed on vesicles derived from plasma membranes (15, 16).

While there are suggestive studies in cells, and while the overall composition of the plasma membrane raises the possibility of phase separation, the “raft hypothesis” has remained a hypothesis. Cell plasma membranes are difficult to study for a number of reasons. Domains in the plasma membrane are certainly small and likely very dynamic. Aside from the notable exceptions like red blood cells (17), the plasma membrane is a small fraction of the total cell membranes, making pure plasma membrane preparations difficult, if not impossible, to obtain. Preparations do not maintain the asymmetric distribution of components between inner and outer leaflets. The chemical complexity of the plasma membrane is also daunting. The plasma membrane has thousands of components, making study of the principles governing behavior intractable.

1.4 Lipid bilayer phases

For the purpose of studying the principles governing membrane behavior, chemically simplified and compositionally well-defined model membranes provide a means to deduce generalizable principles. Bilayers of phospholipids and sterols form various phases. Pure phospholipids can exist as solid ($L\beta$) or liquid (L_d) with a phase

transition occurring at a well-defined temperature, the melting temperature, T_m . High melting temperature (high T_m) and low melting temperature (low T_m) lipids, as referred to in this work, are classified relative to room temperature. Low T_m lipids form an L_d phase with low order and fast diffusion characteristic of a liquid. With the addition of cholesterol to a low T_m lipid, the physical properties change, including increased thickness and decreased permeability, but the mixture remains an L_d phase. At low cholesterol content, high melting lipids will be gel phase, L_β , with high order and slow diffusion characteristic of a solid. With sufficient cholesterol in high T_m lipid, the L_o phase can form. The L_o phase has remarkably high order like a crystal with fast diffusion like a liquid (18).

Mixtures of high T_m lipid, low T_m lipid, and cholesterol that model the outer leaflet of the plasma membrane exhibit rich phase behavior including coexistence of L_o and L_d phases. Coexistence of more and less ordered liquid compartments is analogous to the idea of raft + non-raft behavior in cells. The L_o , or raft-like, phase is enriched in high T_m lipid and has high acyl chain order, whereas the L_d , or non-raft, phase is enriched in low T_m lipid and has low acyl chain order. Though inner leaflet models do not exhibit raft + non-raft behavior, coupling between leaflets is thought to facilitate signaling functions (9, 19).

1.4.1 Lipid bilayer phase diagrams

The rich phase behavior of high T_m /low T_m /chol bilayers has been mapped for a number of mixtures (20–24). A general phase diagram for this type of mixture is

shown in Figure 1.1. Each vertex is 100 mol% of a particular component. At low cholesterol content, there are regions of Ld, L β , and Ld coexistence with L β . By the phase rule, adjacent regions have one more or one fewer phases. At higher cholesterol content, L α phase can form resulting in the three phase region of Ld, L α , and L β coexistence as well as coexistence of L β and L α at low lowT m mole fraction. On top of the three-phase region is the Ld + L α two-phase region.

Along a given thermodynamic tieline in the two-phase region, the compositions in equilibrium are fixed at the tieline endpoints and just phase fractions change. At the lowest tieline of the two-phase region, Ld and L α are the most different. With increasing cholesterol content, Ld and L α become more similar compositionally. The point in the Ld + L α region where the phases approach identity and Ld and L α spontaneously interconvert is referred to as the critical point. This occurs near 40 mol% cholesterol as marked in Figure 1.1.

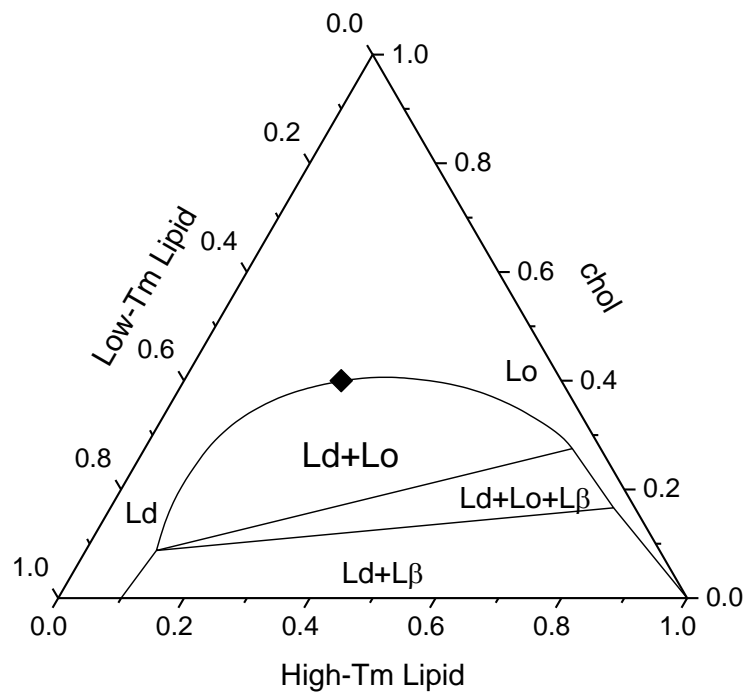


Figure 1.1 General phase diagram for highTm/lowTm/chol. The critical point of the Ld+Lo coexistence region is marked (◆). Figure adapted from (22).

Phase behavior of these mixtures can be resolved with methods based on Förster Resonance Energy Transfer (FRET) and on the partitioning of probes into a particular phase. Samples made along lines in compositional space, or trajectories, are used to systematically determine phase boundaries. When probes partition into the same phase, there is a region of increased FRET efficiency within the bounds of the phase boundaries. For probes that partition into separate phases, there is a region of decreased FRET efficiency corresponding to the coexistence of those phases, because the average distance between respective probes increases (24–26).

1.5 Membrane domain size

Ternary mixtures of the form highT_m/lowT_m/chol have phase separation with domains nanometers or many microns in diameter depending strongly on the lowT_m lipid. 1-palmitoyl-2-oleoyl-phosphatidylcholine (POPC), and other relatively abundant lowT_m lipids in the plasma membrane, give rise to nanometer-scale domains(24), termed nanoscopic phase separation. Giant unilamellar vesicles (GUVs) with such lipids appear uniform by optical microscopy. Nanodomains are observed by methods sensitive to that length scale, such as SANS, ESR, and FRET.

Dioleoylphosphatidylcholine, DOPC, a lipid present only in small amounts physiologically, is a lowT_m lipid that gives rise to micron-scale domains, or macroscopic phase separation observable by optical microscopy on GUVs (23).

Incremental replacement of POPC with DOPC in a four-component mixture with other components fixed can be described in terms of a replacement ratio, ρ , defined as the proportion of lowT_m lipid that is the macroscopic domain-generating lipid, or DOPC in this case.

$$\rho = \frac{\chi_{DOPC}}{\chi_{DOPC} + \chi_{POPC}} \quad (1.1)$$

An example of the compositional space traversed by ρ is shown in the four-component, tetrahedral diagram in Figure 1.2. Replacement, beginning at $\rho = 0$ or the nanoscopic face of the tetrahedron, increases the domain size, and initially, this increase is linear with ρ (27). However, at a higher value of ρ domains abruptly grow

over 100-fold larger over a narrow compositional range (28, 29). The abruptness of this transition implies that an interaction favoring large domains may be overcoming an interaction favoring small domains. Line tension, as discussed below, favors larger domains; for the smaller, nanometer-scale domains, aligned dipoles in the L_o phase could serve to break up domains, thereby decreasing dipole repulsion (30, 31).

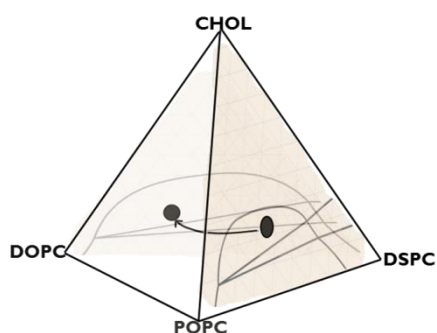


Figure 1.2. Tetrahedral diagram depicting ρ . Four-component phase diagram showing the compositional space traversed from $\rho = 0$ to $\rho = 1$. Figure adapted from (29).

1.6 Line tension

The size distribution and dynamics of membrane domains is governed by line tension, the energy penalty for domain interface. Simulation results implicate line tension as the primary control of domain size (32). Line tension favors coalescing domains since the total length of interface is decreased when domains are larger. Models of the origin of line tension prior to this work presented line tension as entirely

a function of physical parameters relating to adjustments at the Ld/Lo interface due to thickness mismatch (33). Higher order, meaning tighter packing of the chains, in the Lo phase renders it thicker than the coexisting Ld phase, Figure 1.3. However, thickness mismatch increases linearly from $\rho = 0$ to $\rho = 1$ (27), whereas domain size changes abruptly. This implies that thickness mismatch cannot explain the change in domain size over the full range of ρ . Measuring line tension with respect to ρ and determining how other factors, e.g. membrane proteins, change line tension is crucial to understanding how cells could possibly tune domain size in the plasma membrane by exercising precise compositional control.

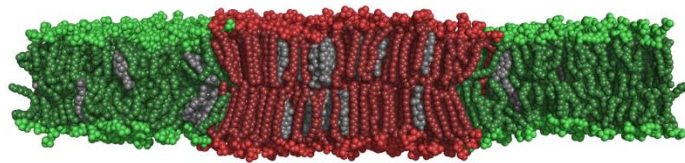


Figure 1.3 Thickness mismatch in a simulated Ld/ Lo bilayer. Molecular dynamics simulation of a bilayer with coexisting Ld and Lo phases, wherein highTm lipids are red, lowTm lipids are green, and cholesterol is grey. The Lo phase, enriched in highTm lipid, is thicker than the Ld phase, enriched in lowTm lipid. Simulation conducted and figure provided by D. Ackerman.

Domains in the membrane exhibit spontaneous, thermally-induced fluctuations, or flickering. Figure 1.4 provides an illustration of such fluctuations,

where $r(\theta)$ is the radius along the contour and R_o is the radius of a static domain of the same area. Expanding the contour coordinates in a Fourier series yields:

$$r(\theta) = R_o \left(1 + u_o + \frac{1}{2} \sum_n u_n e^{in\theta} \right) \quad (1.2)$$

where u_n is the amplitude of the mode number n .

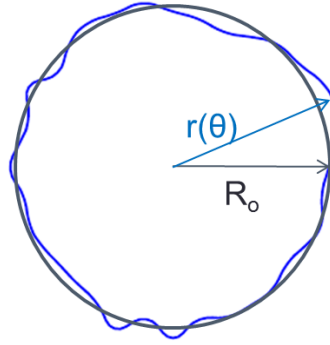


Figure 1.4. Fluctuating domain illustration. The domain is outlined in blue. R_o reflects the radius of a static domain and $r(\theta)$ is the radius along the contour.

Quantifying line tension from the domains fluctuations was accomplished using the methods of Esposito et al. (34) In brief, the spectrum of phase domain boundary fluctuations on a GUV can be decomposed into Fourier modes, which are related to line tension by the following equation:

$$\langle |u_n|^2 \rangle = \frac{2k_B T}{\sigma \pi R_0 (n^2 - 1)} \quad (3)$$

where u_n is the amplitude of the mode number n , k_B is the Boltzmann constant, T is the temperature, σ is the line tension, and r_o is the radius of a circle yielding the domain area. Implicitly, lower line tension describes a domain that fluctuates more.

Simulation work has suggested that line tension below 0.2 pN would render domains too unstable for the measurement of macroscopic phase separation(35, 36). Line tension has been found to decrease as the critical point is approached (29, 37), and lower values of line tension have been reported with higher cholesterol content or increased temperature (34, 38).

1.7 Membrane bending rigidity

A difference in bending rigidity between domains and the surrounding phase might act to limit domain size (32). Smaller domains allow more bending to be accommodated by the less rigid phase. Aside from implications for domain size, the rigidity of the membrane has important implications for the life a cell. Cellular membranes must accommodate curvature for budding events and movement, for example. The resistance of the membrane to bending is described by the bending modulus. Curvature changes of the membrane are required in cell division, endocytosis, autophagy, and other processes. Being able to understand such changes undergone by membranes requires knowledge of their elastic properties. The rigidity

of the membrane is a significant factor in the kinetics of budding events (39).

Curvature can induce sorting of lipids in model membranes such that curvature is accommodated by a less rigid phase (40). Integral membrane proteins are sorted by curvature as well (41). Given this, it is not surprising that highly curved regions in the membrane would differ compositionally from less curved regions.

However, the prevalence of highly curved membranes of raft-like composition seems paradoxical given the reported stiffness of “raft” phases. The observations that gave rise to the raft hypothesis are a primary example: The apical membrane surrounding highly-curved microvilli was found to have more glycosphingolipid and less PC than the basolateral sides(6). Other highly curved membranes having a raft-like composition are virus particles(42), synaptic vesicles(43), and even the dimples associated with cytoskeletal attachment(11). Similarly, in dendritic cells, inhibition of sphingolipid and cholesterol synthesis results in less curvature, i.e. less extensively branched dendritic trees consisting of shorter dendrites of larger diameter (44).

One of the methods with which rigidity can be measured is based on the spontaneous fluctuations of uniform GUVs. First described by Helfrich (45), the fluctuation spectrum is given by:

$$\langle |u(q)|^2 \rangle = \frac{k_B T}{\kappa q^4 + \sigma q^2} \quad (4)$$

where $u(q)$ is the displacement normal to the membrane, $q = (q_x, q_y)$ is the wave vector corresponding to the displacement, k_B is the Boltzmann constant, T is temperature, κ is the bending modulus, and σ is tension. The bending modulus describes the rigidity of the membrane. From equation 4, it can be seen that the tension-dominated regime ($\sigma q^2 \gg \kappa q^4$) corresponds to low q modes, meaning that tension will dominate for large fluctuations with slower relaxation, and rigidity will dominate for smaller, faster fluctuations. To apply deviations from circular in a single focal plane to a 3-dimensional object, the $u(q)$ values are treated as mean square amplitudes of spherical harmonic modes (46).

The rigidity of Lo phases has been observed to be greater than that of Ld phases in the context of single phases (40, 46, 47) and coexisting phases(48). These results together with a correlation between raft-like composition and curvature raise the questions, what is the rigidity difference between phases in models more closely resembling the plasma membrane, and how do the components of the membrane affect rigidity. Membrane rigidity decreases with increasing fractions of naturally-occurring, *cis* unsaturation (49), and correlates with hydrophobic thickness of the membrane(49, 50). The effect of cholesterol has been investigated. Cholesterol has been found to rigidify membranes composed of lowTm lipids with one saturated chain more than membranes composed of lowTm lipids with two unsaturated chains (46, 47, 51, 52). With respect to protein components, peripherally associated proteins like antimicrobial amphipathic helices and viral fusion peptides decrease membrane rigidity(53–56). In contrast, the reports on effects of a transmembrane protein component on membrane rigidity are mixed. Membrane rigidity was shown to be unaffected or slightly

decreased by gramicidin D in 1-stearoyl-2-oleoyl-phosphatidylcholine (SOPC) membranes, by an assortment of transmembrane domains in a proteolytically shaved red blood cell membrane, and by Ca^{2+} ATPase in SOPC membranes(46, 57, 58). The potassium channel, KvAP, which localizes to highly curved regions of some neurons, was found to be sorted by curvature and to moderately increase membrane rigidity (41).

The question of how more complex mixtures would be affected by the addition of physiological amounts of transmembrane protein has not been answered by previous studies. Additionally, these studies include the complexities of protein reconstitution, such as the uncertainty of how much protein is incorporated through the reconstitution, possible residual detergent in measured vesicles, and the heterogeneity of incorporated species. The shape of the protein inclusion is important as well since consideration of the tilt modulus, or resistance to changes in lipid tilt, may be necessary to describe effects of transmembrane proteins that are highly asymmetric with respect to the bilayer midplane (59). Additionally, the ability to study the effect of protein components at near a physiological level is a virtual impossibility for the proteins studied given the need to reconstitute and that the plasma membrane is crowded. Though the fraction of the plasma membrane that is protein by mass is approximately 0.5, the volume fraction of the bilayer interior that is protein is much less, ~0.15-0.20 (60, 61). Occupancy of the membrane interior by a similar fraction of transmembrane protein domains also holds for the case of synaptic vesicles (43).

1.8 Model transmembrane peptides

There is tremendous diversity of both lipid and protein components of the plasma membrane. As with lipids, chemically simplified and compositionally well-defined models provide a means to deduce generalizable principles. Model WALP (acetyl-GWW(AL)_nLWWA-ethanolamide) peptides have been a useful tool in the study of protein-lipid interactions. These highly-purified, hydrophobic, α -helical peptides have a core of alternating alanine and leucine residues, and aromatic residues at the ends to orient the peptide in the membrane (62–64). As a single helix spanning the membrane, they are also a useful model because single-pass proteins are the most common transmembrane anchor, accounting for ~40% of transmembrane domains.(65, 66) Because of the hydrophobic nature of the WALP peptides, incorporating the peptide is accomplished by simply including it in lipid mixtures dissolved in organic solvent. Our studies used a F^{4,5}GWALP (acetyl-GGAFF(LA)_nLWLAGA-amide) peptide, referred to as GWALP in later chapters, Figure 1.5. Like the parent WALP peptides, the GWALP peptides have a number, n, of leucine-alanine repeats. GWALP peptides differ in that they have a single tryptophan rather than the 2 or 4 tryptophan residues in the parent peptides to facilitate fluorescence studies peptides characterized by Sparks et al. (63, 64). The particular GWALP used here is the 23-mer, F^{4,5}GWALP23, or GWALP23, where n=6.

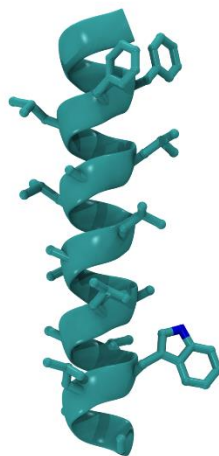


Figure 1.5 Model transmembrane peptide, F^{4,5}GWALP23. Model showing the aromatic residues at the ends of the α -helix and alternating alanine and leucine residues.

1.9 Thesis outline

Compared to line tension, membrane mechanical properties have been explored in greater depth both experimentally and theoretically. However, membrane bending rigidities for models that more closely approximate the plasma membrane are presented in Chapter 2. We show that those models differ markedly from simpler models. Prior to this work, little data was available for membrane domain line tension. This work includes the first systematic studies of line tension with respect to domain size in Chapter 3, which demonstrates that as domain size changes several orders of magnitude, physical properties other than the line tension change little. This finding is

counter to the prevailing theoretical model of line tension. An alternative model for the line tension of ternary mixtures based on pairwise lipid interactions and equilibrium phase compositions is presented in Chapter 4. The appendices contain supporting material for each of the chapters, and a brief investigation of the mechanical properties of membranes with nanoscopic domains showing that the continuous phase determines the overall rigidity of the membrane.

1.10 References

1. van Meer, G., D.R. Voelker, and G.W. Feigenson. 2008. Membrane lipids: where they are and how they behave. *Nat. Rev. Mol. Cell Biol.* 9: 112–124.
2. Huang, J., and G.W. Feigenson. 1999. A microscopic interaction model of maximum solubility of cholesterol in lipid bilayers. *Biophys. J.* 76: 2142.
3. Simons, K., and J. Sampaio. 2011. Membrane organization and lipid rafts. *Cold Spring Harb. Perspect. Biol.* 3: a004697.
4. Jacobson, K., O.G. Mouritsen, and R.G.W. Anderson. 2007. Lipid rafts: at a crossroad between cell biology and physics. *Nat. Cell Biol.* 9: 7–14.
5. Simons, K., and E. Ikonen. 1997. Functional rafts in cell membranes. *Nature.* 387: 569–72.
6. Simons, K., and G. Van Meer. 1988. Lipid sorting in epithelial cells. *Biochemistry.* 27: 6197–6202.
7. Klemm, R.W., C.S. Ejsing, M.A. Surma, H.-J. Kaiser, M.J. Gerl, J.L. Sampaio, Q. de Robillard, C. Ferguson, T.J. Proszynski, A. Shevchenko, and K. Simons. 2009. Segregation of sphingolipids and sterols during formation of secretory vesicles at the trans-Golgi network. *J. Cell Biol.* 185: 601–12.
8. Surma, M.A., C. Klose, and K. Simons. 2012. Lipid-dependent protein sorting at the trans-Golgi network. *Biochim. Biophys. Acta.* 1821: 1059–67.
9. Raghupathy, R., A.A. Anilkumar, A. Polley, P.P. Singh, M. Yadav, C. Johnson,

- S. Suryawanshi, V. Saikam, S.D. Sawant, A. Panda, Z. Guo, R.A. Vishwakarma, M. Rao, and S. Mayor. 2015. Transbilayer lipid interactions mediate nanoclustering of lipid-anchored proteins. *Cell*. 161: 581–94.
10. Roduit, C., F.G. van der Goot, P. De Los Rios, A. Yersin, P. Steiner, G. Dietler, S. Catsicas, F. Lafont, and S. Kasas. 2008. Elastic membrane heterogeneity of living cells revealed by stiff nanoscale membrane domains. *Biophys. J.* 94: 1521–32.
 11. Dinic, J., P. Ashrafzadeh, and I. Parmryd. 2013. Actin filaments attachment at the plasma membrane in live cells cause the formation of ordered lipid domains. *Biochim. Biophys. Acta - Biomembr.* 1828: 1102–1111.
 12. Pralle, A., P. Keller, E.L. Florin, K. Simons, and J.K. Hörber. 2000. Sphingolipid-cholesterol rafts diffuse as small entities in the plasma membrane of mammalian cells. *J. Cell Biol.* 148: 997–1008.
 13. Sezgin, E., I. Levental, S. Mayor, and C. Eggeling. 2017. The mystery of membrane organization: composition, regulation and roles of lipid rafts. *Nat. Rev. Mol. Cell Biol.* 18: 361–374.
 14. Moss, F.R., I. Id, and S.G. Boxer. 2016. Atomic Recombination in Dynamic Secondary Ion Mass Spectrometry Probes Distance in Lipid Assemblies: A Nanometer Chemical Ruler Graphical Abstract HHS Public Access. *J Am Chem Soc.* 138: 16737–16744.
 15. Baumgart, T., A.T. Hammond, P. Sengupta, S.T. Hess, D.A. Holowka, B.A.

- Baird, and W.W. Webb. 2007. Large-scale fluid/fluid phase separation of proteins and lipids in giant plasma membrane vesicles. *Proc. Natl. Acad. Sci. U. S. A.* 104: 3165–70.
16. Levental, I., F.J. Byfield, P. Chowdhury, F. Gai, T. Baumgart, and P.A. Janmey. 2009. Cholesterol-dependent phase separation in cell-derived giant plasma-membrane vesicles. *Biochem. J.* 424: 163–7.
17. Verkleij, A., R.F. Zwaal, B. Roelofsen, P. Comfurius, D. Kastelijn, and L.L. van Deenen. 1973. The asymmetric distribution of phospholipids in the human red cell membrane. A combined study using phospholipases and freeze-etch electron microscopy. *Biochim. Biophys. Acta - Biomembr.* 323: 178–193.
18. Marsh, D. *Handbook of Lipid Bilayers.* .
19. Kiessling, V., C. Wan, and L.K. Tamm. 2009. Domain coupling in asymmetric lipid bilayers. *Biochim. Biophys. Acta.* 1788: 64–71.
20. Marsh, D. 2009. Cholesterol-induced fluid membrane domains: A compendium of lipid-raft ternary phase diagrams. *Biochim. Biophys. Acta - Biomembr.* 1788: 2114–2123.
21. Petruzielo, R.S., F.A. Heberle, P. Drazba, J. Katsaras, and G.W. Feigenson. 2013. Phase behavior and domain size in sphingomyelin-containing lipid bilayers. *Biochim. Biophys. Acta.* 1828: 1302–13.
22. Konyakhina, T.M., J. Wu, J.D. Mastroianni, F.A. Heberle, and G.W. Feigenson. 2013. Phase diagram of a 4-component lipid mixture: DSPC/DOPC/POPC/chol.

- Biochim. Biophys. Acta. 1828: 2204–14.
23. Zhao, J., J. Wu, F. a Heberle, T.T. Mills, P. Klawitter, G. Huang, G. Costanza, and G.W. Feigenson. 2007. Phase studies of model biomembranes: complex behavior of DSPC/DOPC/cholesterol. *Biochim. Biophys. Acta.* 1768: 2764–76.
 24. Heberle, F.A., J. Wu, S.L. Goh, R.S. Petruzielo, and G.W. Feigenson. 2010. Comparison of three ternary lipid bilayer mixtures: FRET and ESR reveal nanodomains. *Biophys. J.* 99: 3309–18.
 25. Heberle, F.A., J.T. Buboltz, D. Stringer, and G.W. Feigenson. 2005. Fluorescence methods to detect phase boundaries in lipid bilayer mixtures. *Biochim. Biophys. Acta.* 1746: 186–92.
 26. Feigenson, G.W., and J.T. Buboltz. 2001. Ternary phase diagram of dipalmitoyl-PC/dilauroyl-PC/cholesterol: nanoscopic domain formation driven by cholesterol. *Biophys. J.* 80: 2775–88.
 27. Heberle, F.A., R.S. Petruzielo, J. Pan, P. Drazba, N. Kučerka, R.F. Standaert, G.W. Feigenson, and J. Katsaras. 2013. Bilayer thickness mismatch controls domain size in model membranes. *J. Am. Chem. Soc.* 135: 6853–9.
 28. Konyakhina, T.M., S.L. Goh, J. Amazon, F.A. Heberle, J. Wu, and G.W. Feigenson. 2011. Control of a nanoscopic-to-macroscopic transition: modulated phases in four-component DSPC/DOPC/POPC/Chol giant unilamellar vesicles. *Biophys. J.* 101: L8-10.
 29. Goh, S.L., J.J. Amazon, and G.W. Feigenson. 2013. Toward a better raft model:

- Modulated phases in the four-component bilayer, DSPC/DOPC/POPC/CHOL. *Biophys. J.* 104: 853–862.
30. Amazon, J.J., and G.W. Feigenson. 2014. Lattice simulations of phase morphology on lipid bilayers: Renormalization, membrane shape, and electrostatic dipole interactions. *Phys. Rev. E - Stat. Nonlinear, Soft Matter Phys.* 89: 1–11.
 31. Dhar, P., E. Eck, J.N. Israelachvili, D.W. Lee, Y. Min, A. Ramachandran, A.J. Waring, and J.A. Zasadzinski. 2012. Lipid-protein interactions alter line tensions and domain size distributions in lung surfactant monolayers. *Biophys. J.* 102: 56–65.
 32. Amazon, J.J., S.L. Goh, and G.W. Feigenson. 2013. Competition between line tension and curvature stabilizes modulated phase patterns on the surface of giant unilamellar vesicles: a simulation study. *Phys. Rev. E. Stat. Nonlin. Soft Matter Phys.* 87: 022708.
 33. Kuzmin, P.I., S.A. Akimov, Y.A. Chizmadzhev, J. Zimmerberg, and F.S. Cohen. 2005. Line tension and interaction energies of membrane rafts calculated from lipid splay and tilt. *Biophys. J.* 88: 1120–33.
 34. Esposito, C., A. Tian, S. Melamed, C. Johnson, S.-Y. Tee, and T. Baumgart. 2007. Flicker spectroscopy of thermal lipid bilayer domain boundary fluctuations. *Biophys. J.* 93: 3169–3181.
 35. Frolov, V.A.J., Y.A. Chizmadzhev, F.S. Cohen, and J. Zimmerberg. 2006.

- “Entropic traps” in the kinetics of phase separation in multicomponent membranes stabilize nanodomains. *Biophys. J.* 91: 189–205.
36. Brown, F.L.H. 2011. Continuum simulations of biomembrane dynamics and the importance of hydrodynamic effects. *Q. Rev. Biophys.* 44: 391–432.
 37. Tian, A., C. Johnson, W. Wang, and T. Baumgart. 2007. Line tension at fluid membrane domain boundaries measured by micropipette aspiration. *Phys. Rev. Lett.* 98: 208102.
 38. Honerkamp-Smith, A.R., P. Cicuti, M.D. Collins, S.L. Veatch, M. den Nijs, M. Schick, and S.L. Keller. 2008. Line tensions, correlation lengths, and critical exponents in lipid membranes near critical points. *Biophys. J.* 95: 236–46.
 39. Morlot, S., V. Galli, M. Klein, N. Chiaruttini, J. Manzi, F. Humbert, L. Dinis, M. Lenz, G. Cappello, and A. Roux. 2012. Membrane shape at the edge of the dynamin helix sets location and duration of the fission reaction. *Cell.* 151: 619–29.
 40. Roux, A., D. Cuvelier, P. Nassoy, J. Prost, P. Bassereau, and B. Goud. 2005. Role of curvature and phase transition in lipid sorting and fission of membrane tubules. *EMBO J.* 24: 1537–45.
 41. Aimon, S., A. Callan-Jones, A. Berthaud, M. Pinot, G.E.S. Toombes, and P. Bassereau. 2014. Membrane shape modulates transmembrane protein distribution. *Dev. Cell.* 28: 212–8.
 42. Brügger, B., B. Glass, P. Haberkant, I. Leibrecht, F.T. Wieland, and H.-G.

- Kräusslich. 2006. The HIV lipidome: a raft with an unusual composition. *Proc. Natl. Acad. Sci. U. S. A.* 103: 2641–6.
43. Takamori, S., M. Holt, K. Stenius, E.A. Lemke, M. Grønborg, D. Riedel, H. Urlaub, S. Schenck, B. Brügger, P. Ringler, S.A. Müller, B. Rammner, F. Gräter, J.S. Hub, B.L. De Groot, G. Mieskes, Y. Moriyama, J. Klingauf, H. Grubmüller, J. Heuser, F. Wieland, and R. Jahn. 2006. Molecular anatomy of a trafficking organelle. *Cell.* 127: 831–46.
44. Hering, H., C.-C. Lin, and M. Sheng. 2003. Lipid Rafts in the Maintenance of Synapses, Dendritic Spines, and Surface AMPA Receptor Stability. *J. Neurosci.* 23: 3262–3271.
45. Helfrich, W. 1973. Elastic properties of lipid bilayers: theory and possible experiments. *Z. Naturforsch. C.* 28: 693–703.
46. Gracià, R.S., N. Bezlyepkina, R.L. Knorr, R. Lipowsky, and R. Dimova. 2010. Effect of cholesterol on the rigidity of saturated and unsaturated membranes: fluctuation and electrodeformation analysis of giant vesicles. *Soft Matter.* 6: 1472.
47. Marsh, D. 2006. Elastic curvature constants of lipid monolayers and bilayers. *Chem. Phys. Lipids.* 144: 146–59.
48. Baumgart, T., S. Das, W.W. Webb, and J.T. Jenkins. 2005. Membrane Elasticity in Giant Vesicles with Fluid Phase Coexistence. *Biophys. J.* 89: 1067–1080.

49. Rawicz, W., K.C. Olbrich, T. McIntosh, D. Needham, and E. Evans. 2000. Effect of chain length and unsaturation on elasticity of lipid bilayers. *Biophys. J.* 79: 328–39.
50. Bermúdez, H., D.A. Hammer, and D.E. Discher. 2004. Effect of Bilayer Thickness on Membrane Bending Rigidity. *Langmuir.* 20: 540–543.
51. Pécrcéaux, J., H.G. Döbereiner, J. Prost, J.F. Joanny, and P. Bassereau. 2004. Refined contour analysis of giant unilamellar vesicles. *Eur. Phys. J. E.* 13: 277–290.
52. Pan, J., S. Tristram-Nagle, and J.F. Nagle. 2009. Effect of cholesterol on structural and mechanical properties of membranes depends on lipid chain saturation. *Phys. Rev. E. Stat. Nonlin. Soft Matter Phys.* 80: 021931.
53. Bouvrais, H., P. Méléard, T. Pott, K.J. Jensen, J. Brask, and J.H. Ipsen. 2008. Softening of POPC membranes by magainin. *Biophys. Chem.* 137: 7–12.
54. Tristram-Nagle, S., and J.F. Nagle. 2007. HIV-1 fusion peptide decreases bending energy and promotes curved fusion intermediates. *Biophys. J.* 93: 2048–55.
55. Khandelia, H., J.H. Ipsen, and O.G. Mouritsen. 2008. The impact of peptides on lipid membranes. *Biochim. Biophys. Acta.* 1778: 1528–36.
56. Settles, E.I., A.F. Loftus, A.N. McKeown, and R. Parthasarathy. 2010. The vesicle trafficking protein Sar1 lowers lipid membrane rigidity. *Biophys. J.* 99: 1539–45.

57. Méléard, P., C. Gerbeaud, P. Bardusco, N. Jeandaine, M.D. Mitov, and L. Fernandez-Puente. 1998. Mechanical properties of model membranes studied from shape transformations of giant vesicles. *Biochimie*. 80: 401–413.
58. Girard, P., J. Prost, and P. Bassereau. 2005. Passive or active fluctuations in membranes containing proteins. *Phys. Rev. Lett.* 94: 088102.
59. Fošnarič, M., A. Iglič, and S. May. 2006. Influence of rigid inclusions on the bending elasticity of a lipid membrane. *Phys. Rev. E*. 74: 051503.
60. Sheetz, M.P. 1993. Glycoprotein motility and dynamic domains in fluid plasma membranes. *Annu. Rev. Biophys. Biomol. Struct.* 22: 417–31.
61. Dupuy, A.D., and D.M. Engelman. 2008. Protein area occupancy at the center of the red blood cell membrane. *Proc. Natl. Acad. Sci. U. S. A.* 105: 2848–52.
62. Andersen, O.S., and R.E. Koeppe. 2007. Bilayer thickness and membrane protein function: an energetic perspective. *Annu. Rev. Biophys. Biomol. Struct.* 36: 107–130.
63. Gleason, N.J., V. V Vostrikov, D. V Greathouse, C. V Grant, S.J. Opella, and R.E. Koeppe. 2012. Tyrosine replacing tryptophan as an anchor in GWALP peptides. *Biochemistry*. 51: 2044–53.
64. Sparks, K.A., N.J. Gleason, R. Gist, R. Langston, D. V Greathouse, and R.E. Koeppe. 2014. Comparisons of interfacial Phe, Tyr, and Trp residues as determinants of orientation and dynamics for GWALP transmembrane peptides. *Biochemistry*. 53: 3637–45.

65. Almén, M.S., K.J. V Nordström, R. Fredriksson, and H.B. Schiöth. 2009. Mapping the human membrane proteome: a majority of the human membrane proteins can be classified according to function and evolutionary origin. *BMC Biol.* 7: 50.
66. Krogh, A., B. Larsson, G. von Heijne, and E.L. Sonnhammer. 2001. Predicting transmembrane protein topology with a hidden Markov model: application to complete genomes. *J. Mol. Biol.* 305: 567–80.

Chapter 2

Membrane bending moduli of coexisting liquid phases containing transmembrane peptide*

2.1 Abstract

A number of highly curved membranes *in vivo*, such as epithelial cell microvilli, have the relatively high sphingolipid content associated with “raft-like” composition. Given the much lower bending energy measured for bilayers with "non-raft" low sphingomyelin and low cholesterol content, observing high curvature for presumably more rigid compositions seems counterintuitive. To understand this behavior, we measured membrane rigidity by fluctuation analysis of giant unilamellar vesicles (GUVs). We found that including a transmembrane helical GWALP peptide increases the membrane bending modulus of the liquid-disordered (Ld) phase. We observed this increase at both low cholesterol fraction and higher, more physiological cholesterol fraction. We found that simplified, commonly-used Ld and liquid-ordered (Lo) phases are not representative of those that coexist. When Ld and Lo phases coexist, GWALP peptide favors the Ld phase with a partition coefficient of 3 - 10, depending on mixture composition. In model membranes at high cholesterol fractions, Ld phases with GWALP have greater bending moduli than the Lo phase that would coexist.

*Usery R, Enoki T, Wickramasinghe S, Nguyen V, Ackerman D, Greathouse D, Koeppe R, Barrera F, Feigenson G. 2018. Membrane bending moduli of coexisting liquid phases containing transmembrane peptide. *Biophysical Journal*. 114(9):2152-2164.

2.2 Introduction

Many cellular functions and structures require membrane deformation. For example, bending of the plasma membrane (PM) occurs in tubulation, fission, and fusion (1). In addition to transient membrane curvature in these processes, the membrane exhibits curvature extremes for structures such as microvilli, dendritic trees, small vesicles and virus particles. Membrane lipids and associated protein components can be sorted by curvature *in vitro*; a less rigid lipid composition can more readily accommodate curvature and proteins may prefer that curvature to varying extents (2, 3).

As an intrinsic plasma membrane organizing principle, ordered, functional platforms or “membrane rafts” are thought to have roles in signaling, cytoskeletal attachment, and virus budding. This membrane compartmentalization can be studied in chemically simplified and compositionally well-defined model membranes. Mixtures of high melting (highT_m) lipid, low melting (lowT_m) lipid, and cholesterol (chol) exhibit liquid-ordered (Lo) and liquid-disordered (Ld) phases, as well as Lo + Ld phase coexistence analogous to raft + non-raft behavior in cells (4–7). For coexisting Lo + Ld, domains are either microns or nanometers in diameter, termed macro- and nanoscopic phase separation, respectively. The rich phase behavior of mixtures of this type, including the regions of Ld + Lo phase coexistence, has been mapped (4–12). Precise determination of phase boundaries and the critical point allow estimation of compositions of coexisting phases, connected in the phase diagram via tielines.

Rafts are thought to be more rigid than their non-raft counterpart since the Lo bending moduli are greater than those of Ld phases (2, 13–15). More rigid membranes

would bend less for a given applied force, yet many highly curved membranes have raft-like compositions. Even the first demonstrations of lipid-based organization showed that proportionally more glycosphingolipids sort to the apical side of epithelial cells, leading to a “raft-like” composition accommodating the extreme curvature of microvilli (16). Highly curved virus particles have raft-like composition (17), as do synaptosomes (18). Dendritic cells, considered to be “raft-rich”, have less extensively branched dendritic trees with spines of larger diameter when sphingolipid synthesis and cholesterol synthesis are inhibited as a means to disrupt membrane rafts (19). Interaction with the actin cytoskeleton dimples the membrane and is associated with raft formation (20). A variety of cancer cells reprogram to be more "raft-rich" (21), but are softer mechanically (22). Other factors are likely involved in each of these examples, but their number and diversity suggest a problem with the view of rafts as rigid platforms compared to the non-raft component.

This apparent difference between membrane bending rigidity *in vitro* and *in vivo* may be connected to the significant protein component in the membrane, a contribution neglected by lipid-only models. As a model for occupancy of the membrane interior by protein, we have used a model transmembrane helical peptide. The family of WALP-like peptides has been designed to resemble α -helical transmembrane segments of membrane proteins and has proven useful in the elucidation of peptide-lipid interaction principles (23, 24). The peptides have a hydrophobic core of alternating leucine and alanine residues and have aromatic or charged residues at the ends of the peptide that prefer the aqueous membrane interface (25–27). Partial unwinding of the peptide terminals provides further stabilization at the membrane interface (28). As a single helix

spanning the membrane, the WALP-like peptides are a useful model of single-pass proteins that account for ~40% of transmembrane domains and are thereby the most common transmembrane anchor (29, 30). GWALP23, in particular, was used in this study because previous NMR studies demonstrated that the peptide had a well-defined transmembrane orientation, that exhibits modest dynamic averaging and is tilted from the bilayer normal in a manner that scales with the bilayer thickness, in various single component bilayers (27). The 23-residue length of GWALP23 is within the range of lengths observed for vertebrate PM transmembrane domains (31).

In this work, we have measured bending moduli of Ld and Lo phases. We have compared commonly-used, simplified 1- and 2-component models of Ld and Lo to 3-component Ld and Lo phases that actually coexist. In order to know the compositions of coexisting phases, we began with the most accurately determined thermodynamic tieline, which is the lower boundary of the two-phase liquid-liquid coexistence region. We prepared membranes of tieline endpoint compositions, and independently measured the bending moduli of these phases that would coexist for four different ternary mixtures including examples of both nanoscopic and macroscopic phase separation. We then investigated whether a model transmembrane helix affects phase behavior, how it partitions between Ld and Lo, how it is oriented in the bilayer, and how it affects bending moduli at relevant fractions. We have addressed these questions at low cholesterol fraction, where the Ld and Lo phase compositions are most different, and also at higher, more physiological cholesterol fraction. We found that the presence of a helical peptide causes the bending rigidity of the Ld phase to approach and, at physiological cholesterol concentrations, exceed that of the Lo phase. Our findings

provide a potential explanation for the raft-like lipid composition of a number of highly curved membranes, as well as a reason to reconsider raft + non-raft behavior in cells.

2.3 Materials and Methods

2.3.1 Materials

Brain sphingomyelin (bSM), 1,2-dioleoyl-sn-glycero-3-phosphocholine (DOPC), 1-palmitoyl-2-oleoyl-sn-glycero-3-phosphocholine (POPC), and 1,2-distearoyl-sn-glycero-3-phosphocholine (DSPC) were purchased from Avanti Polar Lipids (Alabaster, AL). PIPES (piperazine-N,N'-bis(2-ethanesulfonic acid)), KCl (potassium chloride), and EDTA (ethylenediaminetetraacetic acid) were obtained from Sigma-Aldrich (St Louis, MO, USA). Sucrose was from Fisher Scientific (Fair Lawn, NJ), and glucose from Teknova (Hollister, CA). Purity of phospholipids was found to be better than 99.5% using thin layer chromatography (TLC). Briefly, about 20 μg of lipid was spotted on washed and activated Adsorbosil TLC plates (Alltech, Deerfield, IL) and developed in chloroform/methanol/water = 65/25/4. Phospholipid concentrations were determined by inorganic phosphate assay (32), with an error < 1% from 10 replicates. Cholesterol was from Nu Chek Prep, Inc. (Elysian, MN), and stock solutions were made at defined concentrations using standard gravimetric procedures. The fluorescent dyes, 1,1'-didodecyl-3,3',3'-tetramethylindocarbocyanine perchlorate (C12:0 DiI), benzoxazolium, 3-(9,12-octadecadienyl)-2-[3-[3-(9,12-octadecadienyl)-2(3H)-benzoxazolylidene]-1-propenyl]-, perchlorate (FAST DiO), and 2-(4,4-difluoro-5,7-dimethyl-4-bora-3a,4-diazas-indacene-3-pentanoyl)-1-hexadecanoyl-sn-glycero-3-phosphocholine (BODIPY-PC) were from Invitrogen (Carlsbad, CA). Tryptophan

oleoyl ester (TOE) was synthesized in the laboratory of Erwin London, and ergosta-5,7,9(11),22-tetraen-3 β -ol (DHE) was from Sigma Aldrich (St. Louis, MO). Concentrations were determined by absorption spectroscopy using an extinction coefficient of 143,000 M⁻¹cm⁻¹ for C12:0 DiI, 153,000 M⁻¹cm⁻¹ for FAST DiO, 91,800 M⁻¹cm⁻¹ for BODIPY-PC, 5,600 M⁻¹cm⁻¹ for TOE, and 12,900 M⁻¹cm⁻¹ for DHE. Spin-labeled lipid 1-palmitoyl-2-(16-doxyl stearoyl) phosphatidylcholine (16PC) and 1-palmitoyl-2-(7-doxyl stearoyl) phosphatidylcholine (7PC) were a gift from Boris Dzikovski of the National Biomedical Center for Advanced ESR Technology at Cornell University. F^{4,5}GWALP23 (acetyl-GGAFF(LA)₆LWLAGA-ethanolamide)(27), hereafter referred to as GWALP23, was synthesized and purified according to (26). The peptide was dissolved in 2,2,2-trifluoroethanol from Sigma-Aldrich (St. Louis, MO), with the peptide concentration measured by tryptophan absorbance at 280 nm, using an extinction coefficient of 5,600 M⁻¹cm⁻¹.

2.3.2 GUV preparation

GUVs were made by gentle hydration (33) to produce GUVs with uniformly low membrane tension without adding salt, often needed for electrosweelled GUVs (13). Charged lipid provides repulsion between layers in the lipid films to improve hydration of the sample, so 2 mol% of the total lipid in each sample was replaced with the phosphatidylglycerol (PG) cognate of the major lipid. Each sample contained 250 nmol of a lipid or protein/lipid mixture in 200 μ L of 2:1 chloroform:methanol. A thin, even film was created in the bottom of glass tubes using a rotary evaporator. During solvent evaporation, sample tubes were heated to above the transition temperatures of all lipid

components, 45 °C or 55 °C for bSM- or DSPC-containing mixtures, respectively. Residual solvent was then removed by vacuum pumping for 2 hours at ~ 30 mTorr at room temperature. Films were hydrated with the temperature maintained above the transition temperature. GUVs were formed in sucrose solution as the films were cooled from above the transition temperature to 23 °C over 12 hours using a Digi-sense temperature controller R/S (Cole Palmer, Vernon Hills, IL). GUVs were harvested into glucose solution then allowed to settle for 1 h to remove debris before microscopy observations. Experiments were conducted using an inverted widefield microscope, Nikon Eclipse Ti (Nikon Instruments, Melville, NY) equipped with a 60x/1.2 NA phase contrast oil immersion objective and Sola solid-state white light excitation source (Lumencor Inc., Beaverton, OR), which was necessary to achieve sufficient contrast in short exposures for measuring bending moduli, particularly those of the Lo phases.

2.3.3 Membrane bending rigidity measurements

Bending moduli were measured as in (34) by fluctuation analysis of GUVs. Briefly, fluctuations at the GUV equator were observed by phase contrast microscopy. Fluctuation spectra from GUV contours were used to calculate the bending modulus through the relationship

$$\langle |u(q)|^2 \rangle = \frac{k_B T}{\kappa q^4 + \sigma q^2}, \quad (2.1)$$

where $u(q)$ is the displacement normal to the membrane, $q = (q_x, q_y)$ is the wave vector corresponding to the displacement, k_B is the Boltzmann constant, T is the absolute temperature, κ is the bending modulus, and σ is membrane tension. All measurements

were carried out at room temperature. The bending moduli of the coexisting phases were determined by measuring *single-phase GUVs* at the Ld and Lo tieline endpoint compositions. See supporting material in Appendix B for additional information on measurement methods.

2.3.4 FRET trajectories for phase boundaries and K_p determination

We prepared samples along a thermodynamic tieline by rapid solvent exchange (RSE) (35) and measured FRET at room temperature. Decreased FRET, as illustrated in Figure 1, is observed in the two-phase region when donor and acceptor probes partition into different phases. Phase boundaries are identified from the FRET curve shape as previously described (5, 7, 11). Briefly, boundaries are defined by the intersection of linear fits in the regions neighboring an abrupt change in the FRET signal. An internal normalization in the FRET profiles was used to correct variations between samples, such as small differences in sample concentration (36). The fluorescence emission of the acceptor stimulated by the energy transfer of the donor, FRET, was normalized by the donor and acceptor emission in each sample.

K_p determinations were conducted as previously described (34). Briefly, along a tieline, the FRET signal of probes that equilibrate between two phases can be expressed as (36),

$$FRET = \frac{F_{L_D} + \chi_{L_O}(F_{L_O}K_p^D K_p^A - F_{L_D})}{[1 + (K_p^D - 1)\chi_{L_O}][1 + (K_p^A - 1)\chi_{L_O}]} \quad (2.2)$$

where F_{L_d} and F_{L_o} are the intensities in Ld and Lo phases, χ_{L_o} is the phase fraction corresponding to Lo phase, K_p^D is the partition coefficient of the donor, and K_p^A is the

partition coefficient of the acceptor. The fraction of Lo phase, χ_{Lo} , corresponds to the independent variable of equation 2.2. $K_p > 1$ refers to preference for the Ld phase here. For GWALP23 partition coefficient determination, we used FRET between Trp residue of the peptide and DHE, a cholesterol analogue. Cholesterol K_p is known from the phase diagrams for the mixtures used in this work (7, 11). Experimental data were then fit to equation 2.2 with one free-parameter, the peptide K_p . Emission and excitation wavelengths for these experiments are summarized in Tables A.1 and A.2.

2.3.5 Circular Dichroism (CD)

Large unilamellar vesicles (LUVs) were prepared by extruding RSE samples using a miniextruder (Avanti Polar Lipids) assembled with a single polycarbonate filter of 100 nm diameter pore size. Measurements were performed on a Jasco J-815 spectropolarimeter (Easton, MD) at 25°C with a scan rate of 100 nm/min and 25 accumulations. The peptide:lipid molar ratio was 1:50 with a final peptide concentration of 5 μ M. Raw data were converted into mean residue ellipticity according to $[\Theta] = \Theta/(10lcN)$ where Θ is the measured ellipticity, l is the path length of the cell, c is the protein concentration, and N is the number of amino acids. The lipid background was subtracted from the experimental spectra.

2.3.6 Oriented Circular Dichroism (OCD)

Dried lipid or peptide-lipid (peptide:lipid = 1:50 molar ratio) films were resuspended in methanol and deposited onto two circular quartz slides (Hellma Analytics, Germany). The solvent was evaporated by air flow for three hours. The dried samples were rehydrated with 10 mM Na_3PO_4 pH 7 for 15 hours at room temperature at 96% relative

humidity, obtained by using saturated K_2SO_4 . The OCD cell was sealed by the two quartz slides with the deposited samples and contained an inner cavity filled with saturated K_2SO_4 to humidify the sample throughout the experiment. To limit potential linear dichroism artifacts, the sample was rotated through 45° intervals, and the eight measurements were averaged for the final spectrum. Measurements were performed on a Jasco J-815 spectropolarimeter at room temperature. Similar to the CD measurements, the respective lipid blanks were subtracted, and raw data were converted into mean residue ellipticity. The theoretical transmembrane and peripheral peptide spectra were adapted from Wu et al (37). The theoretical spectra were obtained for the fractional helicity of the peptide in each lipid-peptide condition, which was calculated from the CD data by comparing the values at 222 nm to the theoretical values of a complete alpha helix and a random coil (38).

2.3.7 Electron paramagnetic resonance (EPR)

Ld and Lo samples with 16PC or 7PC spin probes were prepared by rapid solvent exchange. Before measurement, samples were pelleted and transferred to 1.5–1.8 x 100-mm glass capillaries. Spectra were recorded on a Bruker ELEXSYS E500 CW EPR Spectrometer operated at X-band frequency (9.4 GHz) with 0.8 Gauss modulation for the 16PC probe and 1.2 Gauss modulation for the 7PC probe. Spectra shown are the average of 20 scans obtained at 22 °C.

2.4 Results

We first measured the rigidity of the Ld phase and the Lo phase using single-phase GUVs for various lipid-only mixtures. Lipid mixtures in this study include:

bSM/DOPC/choI, bSM/POPC/choI, DSPC/DOPC/choI, and DSPC/POPC/choI. Along a thermodynamic tieline, the fractions of Ld and Lo phases are described by the Lever Rule. By measuring the bending moduli of the tieline endpoint compositions, the rigidity of phases that would coexist can be compared. We used existing phase diagrams with high compositional resolution, previously determined for the mixtures DSPC/DOPC/choI, DSPC/POPC/choI, bSM/POPC/choI, and bSM/DOPC/choI (7, 11). With this set of mixtures, we can compare bending energies of the pure Ld and Lo phases that would exhibit nanoscopic or macroscopic phase separation if they coexisted. Whereas mixtures in which the lowT_m lipid is entirely DOPC exhibit domains that are many microns in diameter, those with POPC have similar phase diagrams but with phase domains that are nanometers in diameter (6). We begin with endpoints of the lowest tieline of the Ld + Lo region. Lipid compositions examined in this work are shown in Figure A.1.

2.4.1 Coexisting Ld and Lo at the lower cholesterol tieline

The bending moduli of Lo phases were 2 to nearly 10 times greater than Ld phases, as shown in Table 2.1. The values for the Ld phases we examined range between 1.1 and 3.2 x 10⁻¹⁹J. The bSM-containing Ld phases have greater bending moduli than the DSPC-containing Ld phases. For the Lo phases, measured bending moduli from 6.4 to 10.2 x 10⁻¹⁹J. For the four mixtures studied, the bSM-containing Lo phases have lower bending moduli than the DSPC-containing Lo phases.

TABLE 2.1 Bending moduli of Ld and Lo phases. Ld bending moduli, κ_{Ld} , and Lo bending moduli, κ_{Lo} , for lower tieline Ld and Lo of bSM/DOPC/chol, bSM/POPC/chol, DSPC/DOPC/chol, and DSPC/POPC/chol. SE in parentheses.

	κ_{Ld} (10^{-19} J)	κ_{Lo} (10^{-19} J)
bSM/DOPC/chol	2.6 (0.4)	6.4 (0.3)
bSM/POPC/chol	3.2 (0.4)	6.7 (0.3)
DSPC/DOPC/chol	1.1 (0.2)	10.2 (0.5)
DSPC/POPC/chol	2.3 (0.3)	7.3 (0.4)

These lipid-only mixtures provide a baseline for modeling the influence of transmembrane proteins. To model the plasma membrane with a significant protein component, we include the helical peptide, GWALP23 in the lipid mixtures studied. We first examined whether the peptide changed the phase boundaries for nanoscopic and macroscopic systems by measuring FRET along a compositional trajectory. Sample compositions followed a line parallel to the lower tieline as depicted in Figure 2.1.A. For the purpose of closely replicating all experimental conditions, compositional trajectories with and without peptide were prepared from the same lipid stocks, Figure 2.1.B-2.1.D.

The trajectories with (grey) and without (black) GWALP23 for DSPC/DOPC/chol are shown in Figure 2.1B. FRET between DHE (donor, favors Lo) and FAST DiO (acceptor, favors Ld) is plotted with respect to DSPC fraction. For this system and this dye pair, both boundaries are clearly visible, marked by the shaded regions. Because the boundaries can be difficult to define for nanoscopic systems containing peptide, additional information is useful; thus trajectories in Figure 2.1.C,

2.1.D correspond to the same trajectory in DSPC/POPC/chol but with an additional FRET pair. The boundary at the left-hand side is visible in FRET between Trp and DHE along the trajectory shown in Figure 2.1.C. The lipid-only trajectory contains TOE rather than GWALP23. The shapes of the two curves differ markedly, which can be attributed to differences in the photophysics of energy transfer between the different probes and DHE. FRET between DHE and FAST DiO was simultaneously collected, shown in Figure 2.1.D.

These data show that phase boundaries for both nanoscopic and macroscopic mixtures do not change within experimental uncertainty with addition of up to 2 mol% peptide. Therefore peptide can be added to the same single-phase mixtures as the lipid-only mixtures in order to compare the Ld and Lo phases that would coexist.

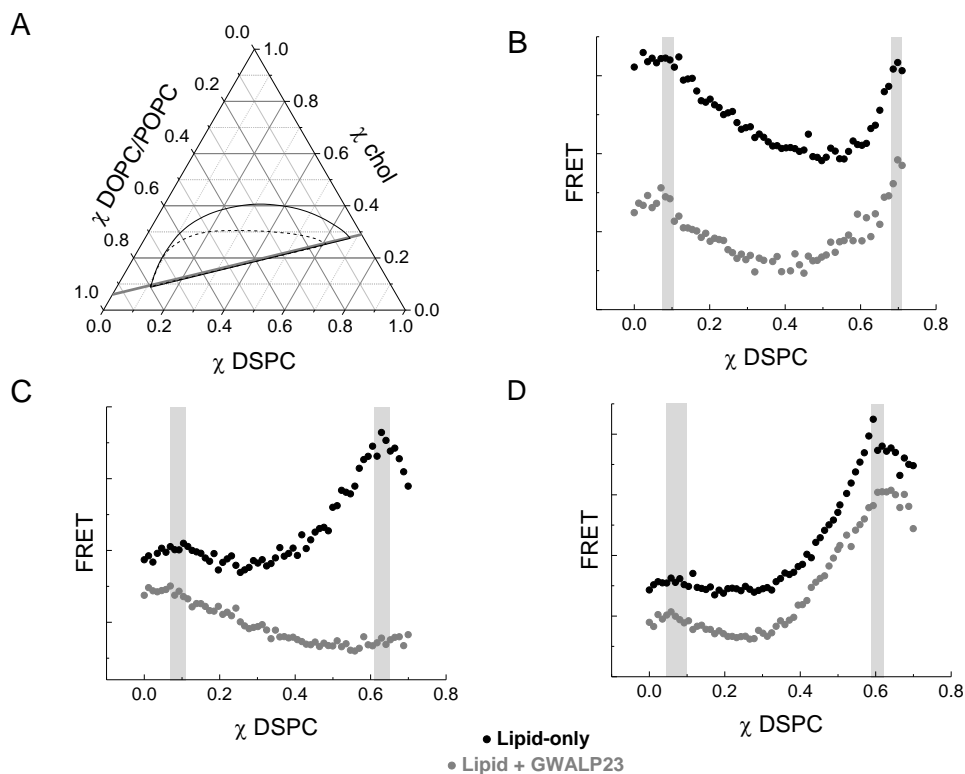


FIGURE 2.1 Presence of GWALP23 does not change phase boundaries. (A) Compositional trajectory (grey line) along which 70 samples were made and the phase coexistence region (Ld+Lo) for DSPC/DOPC/chol (black outline) and DSPC/POPC/chol (dashed line) at 23°C. (B) FRET from DHE to FAST DiO in DSPC/DOPC/chol along the trajectory in (A), in the absence and in the presence of 2 mol% GWALP23. The FRET intensity (in arbitrary units, AU) along the trajectory is shown in black for the lipid-only case and in grey in the presence of peptide (shifted lower for clarity). Phase boundaries correspond to the shaded regions. The width of each shaded region depicts the fitting error. (C) FRET trajectories using Trp and DHE in DSPC/POPC/chol for both the lipid-only trajectory (black) wherein the Trp is that of TOE, and the trajectory with 2 mol% GWALP23 (grey). (D) FRET trajectories using DHE and BODIPY-PC in DSPC/POPC/chol for both the lipid-only trajectory (black) and the trajectory with 2 mol% GWALP23 (grey).

To determine the fraction of peptide in each phase that would occur at equilibrium with coexisting Ld + Lo, and thus should be compared for rigidity measurements, we next investigated the partitioning of the peptide. As described above, partition coefficients can be determined by fitting FRET along the compositional trajectory to Equation 2.2. The sample trajectory for DSPC/DOPC/chol parallel to the lower tieline as shown in Figure 2.1A and analogous trajectory for bSM/DOPC/chol were prepared with 1 mol% peptide. FRET between the GWALP23 tryptophan donor and DHE acceptor were fit to Equation 2.2 to determine K_p . For both DSPC/DOPC/chol and bSM/DOPC/chol, the peptide partitioned favorably into the Ld phase, Figures 2.2.A and 2.2.B, respectively. The K_p of GWALP23 is 13 ± 2 in DSPC/DOPC/chol and 8 ± 1 in bSM/DOPC/chol. Thus, for lipid compositions along the lower tieline of the two-phase region, the Ld phase contains 13 or 8-fold more peptide than the Lo phase for DSPC and bSM mixtures, respectively.

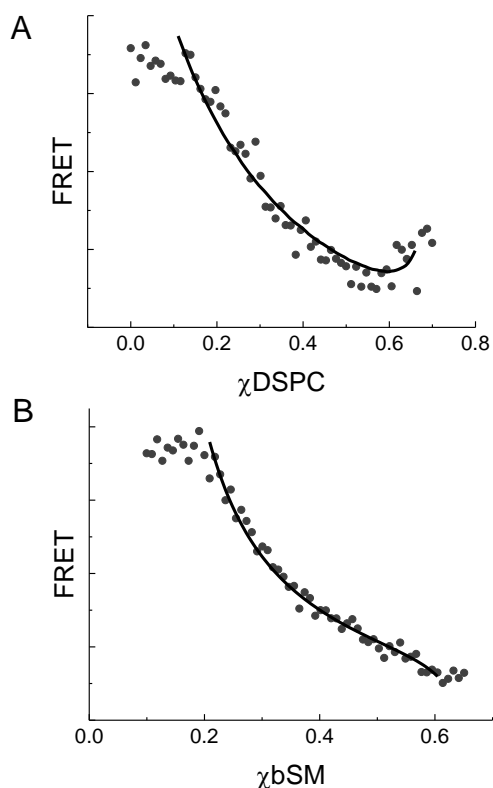


FIGURE 2.2 GWALP23 partitions favorably into the Ld phase. (A) FRET (solid circles, AU) from the GWALP23 tryptophan to DHE is plotted with respect to DSPC fraction along the trajectory for DSPC/DOPC/chol shown in Figure 2.1.A. The best fit to Equation 2.2 (solid line) yielded $K_p = 13 \pm 2$. (B) FRET (solid circles, AU) from the GWALP23 tryptophan to DHE is plotted with respect to bSM fraction along a trajectory parallel to the lower tieline of the two-phase region for bSM/DOPC/chol (11), with the best fit to Equation 2.2 (solid line) yielding $K_p = 8 \pm 1$. Trajectories included 1 mol% GWALP23.

For DSPC/POPC/chol and bSM/POPC/chol, determining the K_p of GWALP23 between Ld and Lo is less straightforward because the domains are nanoscopic. Domains on DSPC/POPC/chol vesicles were previously measured to have a radius of 6.8 nm by small angle neutron scattering, SANS (39). For bSM/POPC/chol, SANS

measurements suggest domains with radii less than 7 nm (11). Since domain size is near the magnitude of the Förster Radius, R_0 , the FRET efficiency is affected. Although Equation 2.2 does not account for the size of domains, we estimated the GWALP23 partition coefficient in lipid mixtures that form nanodomains. To investigate K_p for these nanoscopic mixtures, we again studied sample trajectories parallel to the lower tieline. Trajectories using FRET from GWALP23 tryptophan to BODIPY-PC for DSPC/POPC/chol and for bSM/POPC/chol are shown in Figure A.2. Because both probes partition into the Ld phase, the shapes differ from those in Figure A.2. Without correcting for the small size of the domains, the best fit solid lines in Figure A.2 for the K_p of the peptide for DSPC/POPC/chol and bSM/POPC/chol is 4 ± 1 and 3 ± 1 , respectively. The actual preference of the peptide for Ld would be larger than this fitting suggests because small domain size acts to reduce the influence on FRET of fluorophores separating or co-localizing.

With increasing peptide content, Ld bending moduli increase several-fold for all four mixtures examined, Figure 2.3. The highest concentration of peptide that we could examine in GUVs was 4 mol%. Thus, the maximum peptide concentration that would be in the Lo phase would be 0.5 and 0.3 mol% for the coexisting lower tieline phases of bSM and DSPC mixtures given 8- and 13-fold preference for the Ld phase, respectively. This amount of peptide did not change the bending rigidity of the Lo phase, Figure 2.3. The bending moduli of DSPC/DOPC/chol and DSPC/POPC/chol Ld phases increase with peptide but the bending moduli are much less than those of the respective Lo phases. The bending moduli of bSM/DOPC/chol and bSM/POPC/chol Ld phases approach the bending moduli of the respective Lo phases with increasing peptide

content. For bSM/POPC/chol, the rigidity of the Ld phase with transmembrane peptide exceeds that of the Lo phase.

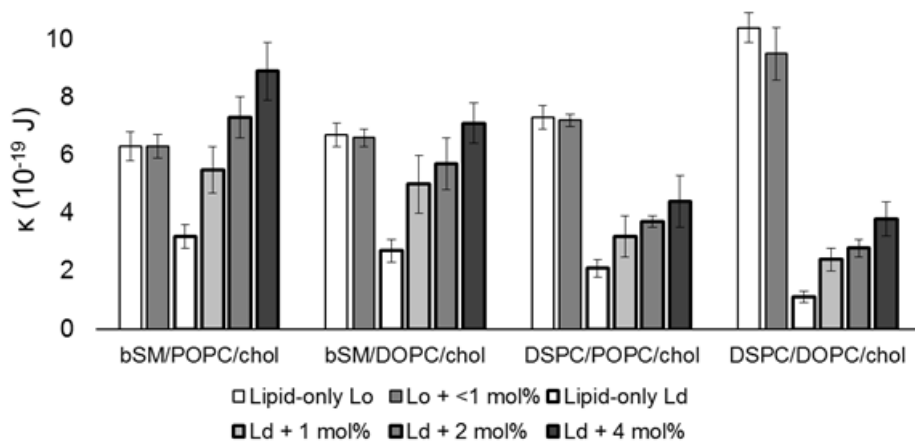


FIGURE 2.3 GWALP23 increases the membrane bending rigidity of the Ld phase. Bending moduli, κ , in 10^{-19} J for Ld (shaded bars), and Lo (patterned bars) with GWALP23 measured for bSM/POPC/chol, bSM/DOPC/chol, DSPC/POPC/chol, and DSPC/DOPC/chol.

We monitored the steady state fluorescence of Trp and C12:0 DiI to evaluate the peptide incorporation in the final aqueous suspension of GUVs. In vesicles containing peptide, the intensity of the tryptophan fluorescence relative to the lipid concentration should be directly proportional to the peptide:lipid ratio. This ratio would be altered during sample preparation if peptide fails to incorporate into the bilayer. We measured tryptophan fluorescence at $ex/em = 280/330$ nm in GUV samples like those used for the rigidity measurements, but vortexed and diluted to reduce the contribution of light scattering. The observed tryptophan emission maximum of 330 nm is consistent with

the peptide being in a hydrophobic environment for both Ld and Lo GUVs. Samples ranged from no peptide up to 4 mol% peptide. At the amount included in our GUV samples, 0.1 mol%, C12:0 DiI fluorescence is directly proportional to the lipid concentration as determined by inorganic phosphate assay (32), Figure A.3. The ratio of tryptophan fluorescence to C12:0 DiI fluorescence is plotted with respect to the mol% of peptide included in sample preparation in Figure 2.4. The relationship is highly linear for Ld (Figure 2.4.A), thus the peptide:lipid ratio in Ld samples does not deviate from expected values. In contrast, the peptide:lipid ratio decreases for Lo phase samples with greater than 1 mol% GWALP23, Figure 2.4.B. The deviation from linearity for the 2 and 4 mol% Lo samples implies that the peptide is depleted during sample preparation. Thus, we limited our bending moduli observations for Lo phase to 1 mol% peptide or less.

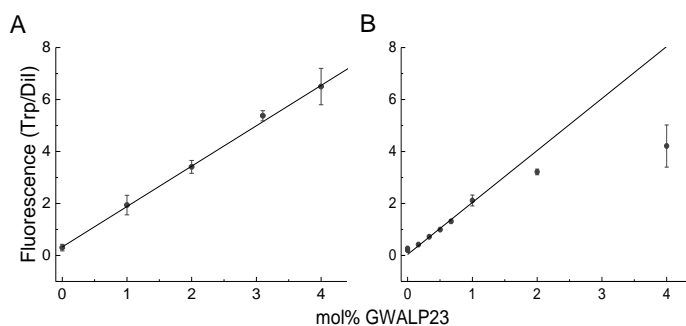


FIGURE 2.4 The ratio of GWALP23:lipid does not change during GUV preparation for DSPC/DOPC/chol Ld up to 4 mol% GWALP23, and for Lo up to 1 mol% GWALP23 in Lo. (A) Ratio of Trp to C12:0 DiI fluorescence in DSPC/DOPC/chol Ld; (B) Ratio of Trp to C12:0 DiI fluorescence in DSPC/DOPC/chol Lo.

We examined the structure and orientation of the peptide with circular dichroism (CD) and oriented circular dichroism (OCD). WALP-like peptides typically acquire helical structure when embedded in lipid membranes (40, 41). We observed clearly helical features in the CD spectrum of the GWALP23 peptide in the Ld phase, with minima at 222 and 208 nm, and a maximum at 195 nm (42), Figure 2.5.A. However, the CD spectrum obtained in Lo lipids was strikingly different. While the same helical features were observed, the spectrum showed a large intensity decrease. The helicity of GWALP23 in Ld and Lo was estimated to be 56 % and 7%, respectively (38). While the former value is expected for a transmembrane peptide, and is consistent with solid-state ^2H NMR measurements for GWALP23 (28), the latter value was too low to be compatible with a transmembrane peptide. Consistent with the results in Figure 2.4.B, the CD in Lo lipids implies that at 2 mol%, GWALP23 is not efficiently incorporating into the Lo phase of these extruded vesicles.

We then performed OCD experiments in hydrated supported bilayers, which inform on the orientation of helical structures with respect to the bilayer. The OCD spectrum of GWALP23 in Ld bilayers overlapped with the corresponding theoretical transmembrane curve, demonstrating that the peptide indeed adopted a transmembrane orientation in Ld. However, the spectrum of GWALP23 in Lo bilayers indicated that the peptide no longer adopted a transmembrane state. In fact, the OCD spectrum in Lo lipids was closer to the theoretical curve corresponding to a helix on the membrane surface, implying that in these conditions GWALP23 was a surface-bound helix. Thus, the OCD spectra revealed that the insertion propensity of GWALP23 shifted from an inserted alpha helix configuration in Ld lipids (Figure 2.5.B) towards a non-inserted one

in Lo lipids (Figure 2.5.C). Figure 2.4 implies that the peptide:lipid ratio is as expected up to 1 mol%. From the characteristic shape of the FRET curves for partition coefficient determination with 0.5 mol% (Figures 2.2 and A.2), we conclude that the peptide is participating in FRET with the cholesterol analogue, DHE, implying insertion. Higher concentrations seem to exceed the capacity of the Lo phase for peptide based on the OCD data at 2 mol% and Figure 2.4.B.

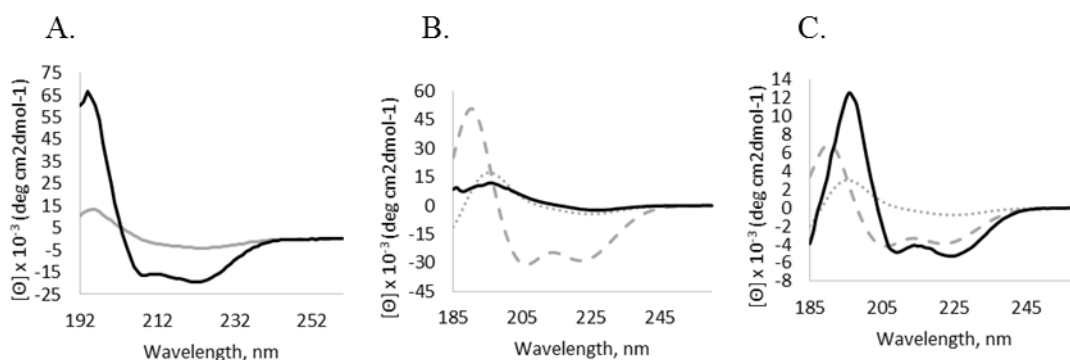


FIGURE 2.5 Structure and orientation of GWALP23 in DSPC/DOPC/chol Ld and Lo. (A) CD spectra of GWALP23 in Ld phase (black) and Lo phase (grey). (B & C) OCD spectra of GWALP23 in hydrated stacked Ld (B) and Lo (C) lipid bilayers. The dotted and dashed lines correspond to theoretical OCD spectra for an ideal α -helix aligned parallel (dotted) and perpendicular (dashed) to the membrane normal, which correspond to transmembrane and peripheral helical peptides, respectively. The significant difference in helicity (7% versus 56%) resulted in the variation in the theoretical curves for GWALP23 in Ld (B) and Lo (C).

In an effort to understand how the peptide affects the Ld and Lo phases, we conducted EPR experiments using 7PC and 16PC probes, wherein the paramagnetic

labels are located near the middle or end of the hydrocarbon chain, respectively. We measured the order parameter at these positions of the acyl chains in DSPC/DOPC/chol. Changes in the phases caused by the peptide could inform our interpretation of bending modulus measurements and insertion. We found that the peptide does not affect order of Ld lipids; see Figure A.4 and Table A.3. This finding implies that the peptide changes the Ld bending modulus without changing the local ordering in the phase. Though this differs from biologically unusual, but well-studied, peptides like gramicidin (43), it is consistent with unchanged phase boundaries and previous studies of WALP peptides in bilayers without cholesterol (44).

2.4.2 High-cholesterol tieline Ld and Lo

From existing phase diagrams, the lowest tieline endpoint compositions correspond to the coexisting Ld and Lo phases that differ the most in composition. As cholesterol content increases, tieline length decreases, becoming zero at the critical point where Ld and Lo do not differ compositionally and spontaneously interconvert. To compare the bending rigidity of the more similar Ld and Lo phases, we examined tieline endpoints at higher cholesterol content. Assuming the tielines fan out evenly between the slope of the lower boundary and the slope of the tangent line at the critical point (45), we interpolated between the slope of the lower boundary of the two-phase region and the slope of the line tangent to the boundary at the putative critical point. The compositions chosen are shown in Figure A.1. Near the critical points for each of the four mixtures, the bending moduli of Ld and Lo are closer in magnitude than the lower tieline compositions, Table 2.2.

TABLE 2.2 Bending moduli of high cholesterol Ld and Lo phases. Ld bending moduli, κ_{Ld} , and Lo bending moduli, κ_{Lo} , for high cholesterol Ld and Lo of bSM/DOPC/chol, bSM/POPC/chol, DSPC/DOPC/chol, and DSPC/POPC/chol. SE in parentheses.

	κ_{Ld} (10^{-19} J)	κ_{Lo} (10^{-19} J)
bSM/DOPC/chol	2.5 (0.4)	3.1 (0.3)
bSM/POPC/chol	2.7 (0.2)	3.1 (0.2)
DSPC/DOPC/chol	2.4 (0.4)	2.8 (0.3)
DSPC/POPC/chol	2.3 (0.1)	3.1 (0.3)

We investigated the effects of the peptide on phase behavior and membrane bending moduli of the more compositionally similar Ld and Lo phases of DSPC/DOPC/chol at higher cholesterol fractions. We continued our investigations with DSPC/DOPC/chol because we have a greater confidence in the critical point location determined for this mixture in previous work (7), and as a result, the appropriate tieline slope to use for higher tieline measurements. We again used FRET trajectories to define phase boundaries and to determine the K_p of the peptide at these higher cholesterol fractions. The slope of the high cholesterol trajectory was determined as described above. We found the phase boundaries were unchanged by the presence of 1 mol% peptide, Figure 2.6. The K_p of the peptide was found to be 3 ± 1 favoring the Ld phase, Figure 2.7. The K_p of DHE approaches 1 at this higher cholesterol tieline, and for that reason, the shape of the FRET curve in Figure 2.7 differs markedly from those in Figure 2.2. Consistent with this decrease of DHE K_p as cholesterol fraction increases, a decrease in K_p of ~ 3 -fold from the lower to the higher tieline in the two-phase region was also observed for FAST DiO, Figure A.5.

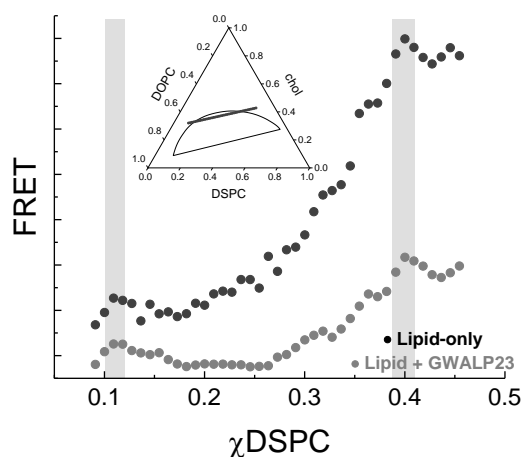


FIGURE 2.6 The presence of 2 mol% GWALP23 does not change phase boundaries of DSPC/DOPC/chol at high cholesterol fraction. FRET from DHE to FAST DiO along the trajectory in the inset in the absence (black, upper) and in the presence of 1 mol% GWALP23 (grey, shifted lower for clarity). Boundaries correspond to the shaded regions. The width of each shaded region is the fitting error.

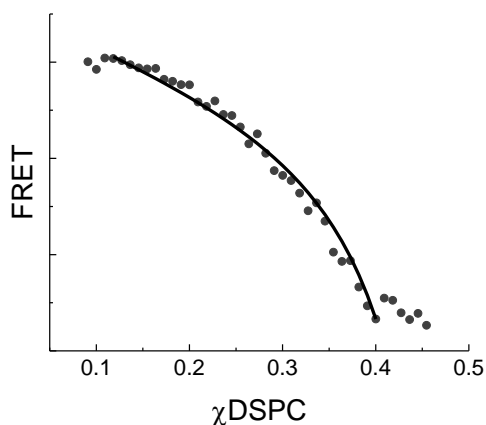


FIGURE 2.7 GWALP23 partitions into the Ld phase at high cholesterol fraction. FRET from the GWALP23 tryptophan to DHE is plotted with respect to DSPC fraction along the trajectory for DSPC/DOPC/chol shown in Figure 2.6, inset, with 1 mol% GWALP23. The best fit (solid line) to Equation 2.2 yields $K_p = 3 \pm 1$.

Given the smaller K_p of the peptide between Ld and Lo phases at high cholesterol fraction, we compared the Ld phase with increasing concentrations of peptide to the Lo phase with no peptide and with 1 mol% GWALP23 in Figure 2.8. The peptide increases the bending modulus of the Ld phase, and at 2 mol% peptide, the bending modulus of the Ld phase is greater than that of the Lo phase with 1 mol% peptide.

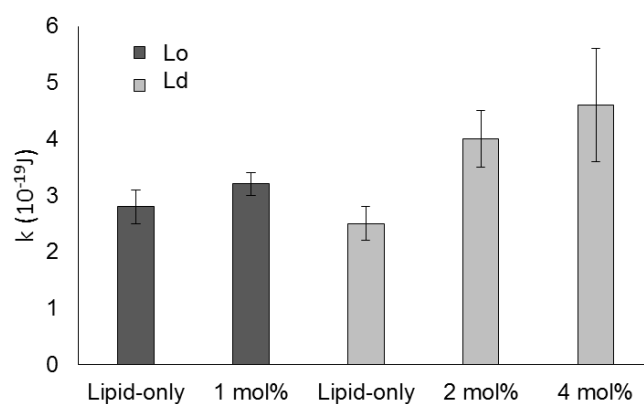


FIGURE 2.8 GWALP23 increases the rigidity of the Ld phase at the high cholesterol tieline for DSPC/DOPC/chol. Bending moduli, κ , of Ld (light bars) and Lo (dark bars) at these higher tieline endpoint compositions were measured. The bending modulus is shown for the Ld phase with 2 and 4 mol% GWALP23. Error bars reflect SE.

2.4.3 Difference in Ld and Lo bending moduli of various models

As we have shown, the membrane bending moduli of Ld and Lo become very similar at higher cholesterol fractions. A separate issue is how well commonly-used, simplified mixtures model the behavior of coexisting phases. We simplify the mixtures by using pure lowTm lipid, DOPC or POPC, for Ld, and a binary highTm lipid/chol for

Lo. In Figure 2.9, simplified, lower tieline, and high cholesterol Ld and Lo compositions are shown by the line endpoints on the representative diagram. Simplified mixtures are at extremes of the diagram, coinciding with the lowT_m vertex for Ld and the highT_m/chol binary axis for Lo. The lower tieline compositions are shown at the bottom of the two phase region and high cholesterol compositions are near the top. Compositions were chosen based on published phase diagrams for each mixture [5, 6] and are plotted in Figure A.1. The difference in bending moduli, $\Delta\kappa = \kappa_{Lo} - \kappa_{Ld}$, for each set of simple, lower tieline, and high cholesterol for bSM/POPC/chol, bSM/DOPC/chol, DSPC/POPC/chol, and DSPC/DOPC/chol is plotted with respect to distance in compositional space. This distance is calculated as a three-dimensional Euclidean distance normalized to one side of the ternary diagram. Thus, the simplified mixtures are the furthest apart in both composition and in bending moduli, and the high cholesterol tieline endpoints are the closest. For comparison to the ternary mixtures, we measured the bending moduli of a simplified Ld phase, DOPC, with peptide. We found the bending modulus increased with peptide concentration, and this increase was more gradual than in the ternary Ld compositions, Figure A.6.

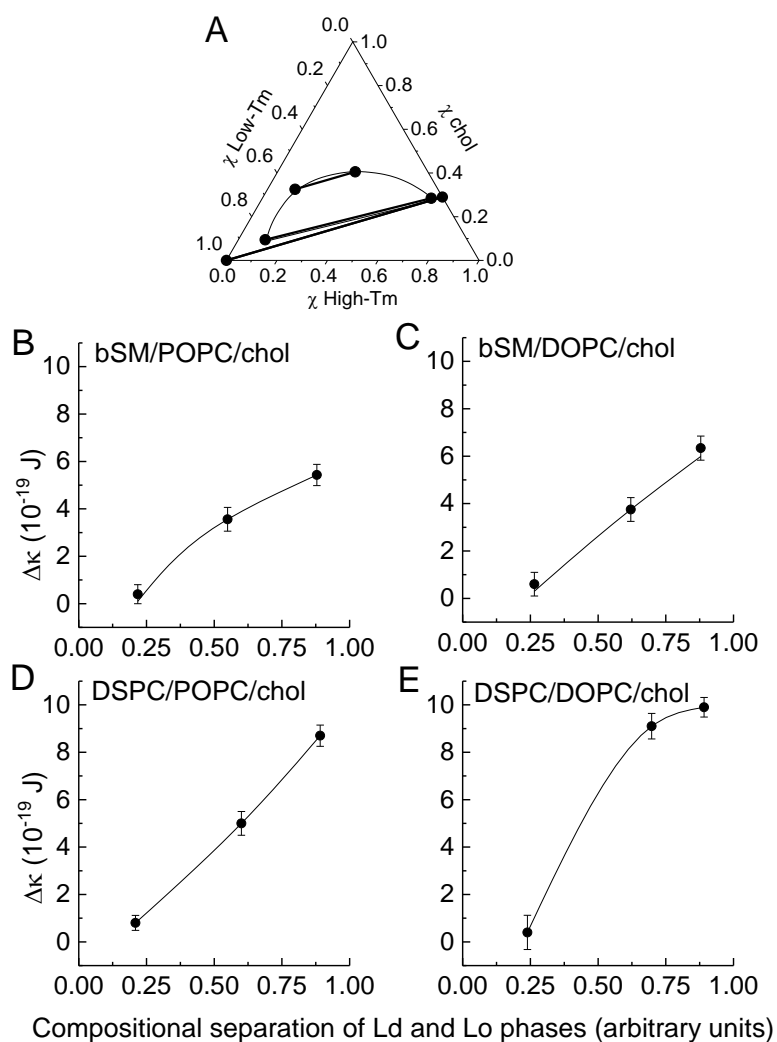


FIGURE 2.9 Bending moduli of Ld and Lo phases in lipid-only mixtures. (A) The compositions we compared are shown representatively as line endpoints on the generic phase diagram above. Simplified, lower tieline, and high cholesterol Ld and Lo compositions for bSM/POPC/chol, bSM/DOPC/chol, DSPC/POPC/chol, and DSPC/DOPC/chol are plotted in Figure A.1. The difference in bending moduli, $\Delta\kappa = \kappa_{\text{Lo}} - \kappa_{\text{Ld}}$, between simple, lower tieline, and high cholesterol Lo and Ld phases for bSM/POPC/chol (A), bSM/DOPC/chol (B), DSPC/POPC/chol (C), and DSPC/DOPC/chol (D) is plotted with respect to distance in composition space, or the compositional separation of Ld and Lo phases.

2.5 Discussion

Many cellular functions and structures require membrane deformation subjecting the membrane to mechanical stress. As expected, others have found raft-like Lo phases to have membrane bending moduli greater than those of Ld for both single phases (2, 13, 14) and coexisting phases (15). These results together with a correlation between raft-like composition and curvature raise questions about what the rigidity difference is between phases in models that more closely resemble the plasma membrane and how the components of the membrane affect rigidity. Membrane bending moduli decrease with increasing degree of *cis* unsaturation (46), and increase with hydrophobic thickness of the membrane (46, 47). Cholesterol has been found to rigidify membranes composed of lowT_m lipids in which at least one chain is saturated, but not membranes in which both chains are unsaturated, such as DOPC (13, 14, 48, 49). The mixtures used in this study offer a range of physiological relevance. bSM as the highT_m lipid is more representative than DSPC, POPC is naturally more abundant than DOPC in animal cell PMs, and the higher cholesterol content we examined is physiologically more relevant than that of the lower tieline endpoints (50–52). For each mixture we have focused on Ld and Lo phases that would coexist, and we sought to address the effects of a peptide component in the context of these phases.

2.5.1 Coexisting Ld and Lo at the lower cholesterol tieline

The bending moduli of lower tieline Lo phases are much greater than those of the corresponding Ld phases, Table 2.1. Others have also suggested or measured the

bending rigidity of the Lo phase to be several times greater than that of the Ld phase (53–55). With ternary mixtures, the accuracy of the measurement is limited somewhat by the variation between vesicles. Our measurement of the DSPC/DOPC/choL Ld phase is consistent with measurements by other groups and other methods (54), and in only this case, near to measurements for one-component membranes of the major component, DOPC (13, 56). When overall composition is similar, the mixtures containing POPC have greater membrane bending moduli than those containing DOPC, consistent with the findings of others (14). The presence of cholesterol likely increases this rigidity difference since POPC has a saturated acyl chain and DOPC does not (49, 57). For the Ld compositions in Table 2.1, it can be seen that DOPC mixtures are less rigid than the corresponding mixtures with POPC. This trend does not hold for the DSPC Lo compositions due to the difference in phase boundaries between DSPC/DOPC/choL and DSPC/POPC/choL. The DSPC/POPC/choL Lo phase has 15 mol% lowT_m lipid while the corresponding DOPC mixture has only 3 mol%.

Comparing the DSPC mixtures to the bSM mixtures at the lowest tieline, the length of the tieline for bSM mixtures is shorter than that of the DSPC mixtures, meaning that the bSM Ld and Lo phases are compositionally more similar. In contrast to the respective DSPC Lo phases with a 5-fold difference in the amount of lowT_m lipid, the difference in the amount of lowT_m lipid is less than two-fold, with 7 mol% lowT_m lipid in the bSM/POPC/choL Lo phase and 4 mol% in the bSM/DOPC/choL Lo phase. This similarity in the overall Lo composition for bSM/DOPC/choL and bSM/POPC/choL results in similar bending moduli. For the Ld phases, while the DSPC-containing Ld phases have 80% lowT_m lipid (Figure A.1), bSM/DOPC/choL and bSM/POPC/choL

contain only 70 mol% low T_m lipid, consistent with their higher bending moduli (Table 2.1).

The GWALP peptide used in this study partitions favorably into the Ld phase. In the mixtures for which we can conclusively determine the K_p as described, the peptide concentration is ~ 10-fold greater in the Ld phase when Ld and Lo coexist in these mixtures. Preference for Ld phase is usual for transmembrane proteins (58). Though commonly considered “raftophilic”, GPI anchored proteins are, at best, not excluded from the more ordered phase (59, 60). In giant plasma membrane vesicles, inclusion of transmembrane helices in the more ordered phase is dependent on palmitoylation, and even palmitoylated peptides still have a K_p near 1, i.e. they do not strongly favor the more ordered phase (61).

We find that GWALP23 peptide increases the rigidity of the Ld phase. With increasing peptide content, the bending moduli of the Ld phase approaches that of the Lo phase, and in the case of the bSM/POPC/chol mixture with 4 mol% peptide, the rigidity of the Ld phase exceeds that of the Lo phase. The increases in the Ld bending moduli with 4 mol% peptide compared to the lipid-only Ld were 2.8-, 2.6-, 2.1-, and 3.4-fold for bSM/POPC/chol, bSM/DOPC/chol, DSPC/POPC/chol, and DSPC/DOPC/chol, respectively. With peptide included in an amount consistent with the K_p and below 1 mol%, the Lo bending moduli are unchanged.

2.5.2 GWALP23 incorporation and orientation in the bilayer

Whereas proteins make up about half of the total mass of the PM, the volume of the bilayer *interior* that is protein is closer to 20% (2, 3). A similar volume fraction of

transmembrane peptide in our vesicle preparations would be ~9 mol% GWALP23 (62, 63). We could not prepare GUVs with such a high fraction of peptide. The highest concentration of peptide that we could examine in Ld GUVs was 4 mol%. Perhaps the increased membrane rigidity inhibits the spontaneous formation of GUVs. Consistent with this possibility, we could prepare GUVs of DOPC, which are less rigid than those having the ternary compositions, with up to 6 mol% peptide, Figure A.6.

In our investigations of GWALP23 structure using CD, we found low signal amplitude for the peptide in Lo. The OCD measurements to examine the orientation of the peptide revealed that while the peptide was inserted with a low tilt angle from the bilayer normal in the Ld phase, this was not the case for the Lo phase. In Ld, the extent of helix and the helix tilt are consistent with NMR measurements in single-component bilayers (28). In Lo, the OCD spectrum is consistent with the peptide being oriented perpendicular to the membrane normal. Given the shift away from inserted to surface-bound for oriented Lo bilayers with 2 mol% peptide, an ensuing loss of peptide after extrusion of the vesicles to form 100 nm LUVs is likely due to GWALP23 not being inserted. As the theoretical oriented CD curves depend on the percentage of helical residues, the significant difference in helicity resulted in the variation in the theoretical curves for GWALP23 in Lo (Figure 2.5.B) and Ld (Figure 2.5.C).

Our observations with OCD are consistent with the findings in Figure 2.4. The peptide:lipid ratio appears to be as anticipated up to 4 mol% in Ld, but this is not the case with Lo GUV preparations. The apparent peptide:lipid ratio in Lo begins to deviate from expected values with greater than 1 mol% (Figure 2.4). FRET curves we could fit

to a partition coefficient required 1 mol% GWALP23 or less. FRET measurements between GWALP23 Trp and membrane-bound DHE or BODIPY-PC reveal a characteristic shape that can only occur if the peptide is located within the bilayer of these non-extruded vesicles. We conclude the peptide is inserted at this low concentration. Because GWALP23 partitions ~ 3- to 10-fold favoring the Ld phase, we compare the bending energy of an Ld phase containing peptide with an Lo phase containing ~ 3- to 10-fold less peptide. Given the peptide concentrations for which we could obtain Ld GUVs and our conclusions regarding incorporation in the Lo phase, our Lo phases for the bending moduli measurements contain less than 1 mol% GWALP23.

2.5.3 High-cholesterol tieline Ld and Lo

The more compositionally similar Ld and Lo phases at higher cholesterol fractions are more physiologically relevant, given the typical cholesterol content of 40-50 mol% in the animal cell membrane (52). The difference in bending moduli between Ld and Lo at higher cholesterol content becomes small for all of the lipid-only cases. The difference in bending moduli at the high cholesterol compositions is greatest for DSPC/POPC/chol. Because of the shape of the two-phase region for this mixture, the compositions chosen for comparison at a higher tieline are farther apart in compositional space. Further, these DSPC/POPC/chol compositions nearer to the critical point did not contain as much cholesterol as the other “high cholesterol” compositions, Figure A.1

The phase boundaries for the high cholesterol compositions of DSPC/DOPC/chol with up to 1 mol% GWALP23 did not differ from the phase boundaries without peptide, as observed for the low cholesterol compositions. The

peptide still favors the Ld phase although the K_p of 3 at high cholesterol is about 4-fold lower than the K_p of 13 at low cholesterol. A similar change in K_p was also observed for FAST DiO. This is, perhaps, not surprising given the greater similarity of the Ld and Lo compositions.

The transmembrane peptide increased the rigidity of the DSPC/DOPC/chol Ld phase at high cholesterol fraction. The bending modulus of Ld with 4 mol% peptide is 2-fold greater than that of the lipid-only Ld phase and 1.4-fold greater than that of the Lo phase. Further, using the measured peptide K_p of 3, the Ld phase with 4 mol% GWALP23 becomes more rigid than the Lo phase with 1 mol% GWALP23, where the respective fractions of peptide are representative of distribution between Ld and Lo when they coexist. At near physiological cholesterol content and with a significant fraction of the membrane volume being occupied by transmembrane helices, the bending modulus of the disordered phase is greater than that of the ordered phase.

2.5.4 Increased membrane bending rigidity with GWALP23

Both simulation and experimental data have indicated that WALP peptides could alter bilayer thickness (44, 64). Deviations from the equilibrium bilayer thickness would undoubtedly contribute to increased membrane bending rigidity. However the changes in bilayer thickness observed experimentally are slight and likely do not account for the entirety of the increase in bending moduli of Ld phases with GWALP23.

GWALP23 has been shown experimentally and in molecular dynamics simulations to change the size of domains (34, 64). Molecular dynamics simulations of the peptide in membrane compositions mimicking those used here suggest that the

peptide increases domain registration and is depleted from the domain interface (64). Both the increase in domain size and the interface depletion imply increased line tension. However, as the EPR data show, Figure A.4 and Table A.3, these changes are not accomplished through changes in ordering in the phase. Increased domain registration in the two leaflets, as observed in simulations in the presence of peptide, could point to a mechanism for increased rigidity of the Ld phase.

By spanning the bilayer, the peptide could reduce the ability of the leaflets to slide relative to each other. Rather than the bilayer consisting of two elastic sheets fluctuating somewhat independently, a bilayer with fully coupled leaflets is effectively one elastic sheet of double the thickness with a bending modulus greater than the uncoupled bilayer (14, 65). The bending moduli of the four different Ld phases showed increases ranging from 2- to 3.5-fold with 4 mol% GWALP23.

2.5.5 Simplified mixtures are not representative of coexisting phases

The measurements discussed above were for the lower and high-cholesterol tielines of the two-phase region. We also compared these ternary Ld and Lo compositions to commonly used single- component or binary mixtures. From Figure 2.9, we see that the simplified phases are only representative in the case of the DSPC/DOPC/chol lower cholesterol compositions. The bending moduli of the ternary Ld and Lo phases of bSM/DOPC/chol and bSM/POPC/chol differed significantly from the simplified models. The Ld phases had bending moduli up to three times greater than the simple Ld phases, and the actual Lo phases in the Ld + Lo coexistence region had bending moduli ~10% smaller than the simple Lo phase outside this region. Thus these

simplified models are perhaps less representative of the more physiological Ld or Lo phases that would coexist.

2.6 Conclusions

In this work, we begin to address how a transmembrane α -helical peptide influences bilayer mechanical properties. GWALP23 exhibits a preference for the Ld phase, but does not change phase boundaries. We determined the rigidity of the Ld and Lo phases that coexist by independently measuring the rigidity of single-phase GUVs of the compositions at the tieline endpoints. GWALP23 transmembrane peptide causes a striking increase in the bending modulus of the Ld phase for all mixtures in this study. We examined the effects of the peptide at high, more physiological cholesterol content and found that the peptide causes the bending modulus of the Ld phase to surpass that of the Lo phase. We compared the rigidity of these lipid-only lower tieline compositions to the rigidity of the Ld+Lo phases coexisting at higher cholesterol content, and to simplified Ld and Lo compositions. We found that the ternary mixtures differed significantly from the simplified phases, and the difference in Ld and Lo rigidity decreases at high cholesterol content.

2.7 Author contributions

Figure 2.1 FRET trajectory data from RDU and TAE

Table 2.1 Bending rigidity measurements by RDU

Figure 2.2 FRET trajectories by RDU

Figure 2.3 Bending rigidity measurements by RDU (DSPC/DOPC/chol, DSPC/POPC/chol, bSM/DOPC/chol Lo, bSM/POPC/chol Lo) and SPW (bSM/DOPC/chol Ld, bSM/POPC/chol Ld)

Figure 2.4 GWALP:Lipid ratio from fluorescence by RDU

Figure 2.5 CD and Oriented CD by VPN

Table 2.2 Bending rigidity measurements by RDU

Figure 2.6 FRET trajectories by RDU

Figure 2.7 Kp determination by RDU

Figure 2.8 Bending rigidity measurements by RDU

Figure 2.9 Bending rigidity measurements by RDU

Edge detection in analysis of bending rigidity data provided by DGA

2.8 References

1. McMahon, H.T., and J.L. Gallop. 2005. Membrane curvature and mechanisms of dynamic cell membrane remodelling. *Nature*. 438: 590–596.
2. Roux, A., D. Cuvelier, P. Nassoy, J. Prost, P. Bassereau, and B. Goud. 2005. Role of curvature and phase transition in lipid sorting and fission of membrane tubules. *EMBO J*. 24: 1537–45.
3. Aimon, S., A. Callan-Jones, A. Berthaud, M. Pinot, G.E.S. Toombes, and P. Bassereau. 2014. Membrane shape modulates transmembrane protein distribution. *Dev. Cell*. 28: 212–8.
4. Feigenson, G.W., and J.T. Buboltz. 2001. Ternary phase diagram of dipalmitoyl-PC/dilauroyl-PC/cholesterol: nanoscopic domain formation driven by cholesterol. *Biophys. J*. 80: 2775–88.

5. Zhao, J., J. Wu, F. a Heberle, T.T. Mills, P. Klawitter, G. Huang, G. Costanza, and G.W. Feigenson. 2007. Phase studies of model biomembranes: complex behavior of DSPC/DOPC/cholesterol. *Biochim. Biophys. Acta.* 1768: 2764–76.
6. Heberle, F.A., J. Wu, S.L. Goh, R.S. Petruzielo, and G.W. Feigenson. 2010. Comparison of three ternary lipid bilayer mixtures: FRET and ESR reveal nanodomains. *Biophys. J.* 99: 3309–18.
7. Konyakhina, T.M., J. Wu, J.D. Mastroianni, F.A. Heberle, and G.W. Feigenson. 2013. Phase diagram of a 4-component lipid mixture: DSPC/DOPC/POPC/chol. *Biochim. Biophys. Acta.* 1828: 2204–14.
8. Marsh, D. 2009. Cholesterol-induced fluid membrane domains: A compendium of lipid-raft ternary phase diagrams. *Biochim. Biophys. Acta - Biomembr.* 1788: 2114–2123.
9. Veatch, S.L., K. Gawrisch, and S.L. Keller. 2006. Closed-loop miscibility gap and quantitative tie-lines in ternary membranes containing diphytanoyl PC. *Biophys. J.* 90: 4428–36.
10. Uppamoochikkal, P., S. Tristram-Nagle, and J.F. Nagle. 2010. Orientation of tie-lines in the phase diagram of DOPC/DPPC/cholesterol model biomembranes. *Langmuir.* 26: 17363–8.
11. Petruzielo, R.S., F.A. Heberle, P. Drazba, J. Katsaras, and G.W. Feigenson. 2013. Phase behavior and domain size in sphingomyelin-containing lipid bilayers. *Biochim. Biophys. Acta.* 1828: 1302–13.
12. Bezlyepkina, N., R.S. Gracià, P. Shchelokovskyy, R. Lipowsky, and R. Dimova. 2013. Phase Diagram and Tie-Line Determination for the Ternary Mixture DOPC/eSM/Cholesterol. *Biophysj.* 104: 1456–1464.
13. Gracià, R.S., N. Bezlyepkina, R.L. Knorr, R. Lipowsky, and R. Dimova. 2010. Effect of cholesterol on the rigidity of saturated and unsaturated membranes: fluctuation and electrodeformation analysis of giant vesicles. *Soft Matter.* 6: 1472.
14. Marsh, D. 2006. Elastic curvature constants of lipid monolayers and bilayers. *Chem. Phys. Lipids.* 144: 146–59.
15. Baumgart, T., S. Das, W.W. Webb, and J.T. Jenkins. 2005. Membrane Elasticity in Giant Vesicles with Fluid Phase Coexistence. *Biophys. J.* 89: 1067–1080.
16. Simons, K., and G. Van Meer. 1988. Lipid sorting in epithelial cells. *Biochemistry.* 27: 6197–6202.

17. Brügger, B., B. Glass, P. Haberkant, I. Leibrecht, F.T. Wieland, and H.-G. Kräusslich. 2006. The HIV lipidome: a raft with an unusual composition. *Proc. Natl. Acad. Sci. U. S. A.* 103: 2641–6.
18. Takamori, S., M. Holt, K. Stenius, E.A. Lemke, M. Grønborg, D. Riedel, H. Urlaub, S. Schenck, B. Brügger, P. Ringler, S.A. Müller, B. Rammner, F. Gräter, J.S. Hub, B.L. De Groot, G. Mieskes, Y. Moriyama, J. Klingauf, H. Grubmüller, J. Heuser, F. Wieland, and R. Jahn. 2006. Molecular anatomy of a trafficking organelle. *Cell.* 127: 831–46.
19. Hering, H., C.-C. Lin, and M. Sheng. 2003. Lipid Rafts in the Maintenance of Synapses, Dendritic Spines, and Surface AMPA Receptor Stability. *J. Neurosci.* 23: 3262–3271.
20. Dinic, J., P. Ashrafzadeh, and I. Parmryd. 2013. Actin filaments attachment at the plasma membrane in live cells cause the formation of ordered lipid domains. *Biochim. Biophys. Acta - Biomembr.* 1828: 1102–1111.
21. Beloribi-Djefafli, S., S. Vasseur, and F. Guillaumond. 2016. Lipid metabolic reprogramming in cancer cells. *Oncogenesis.* 5: e189.
22. Cross, S.E., Y.-S. Jin, J. Rao, and J.K. Gimzewski. 2007. Nanomechanical analysis of cells from cancer patients. *Nat. Nanotechnol.* 2: 780–783.
23. Killian, J.A., I. Salemink, M.R.R. de Planque, G. Lindblom, R.E. Koeppe, and D. V. Greathouse. 1996. Induction of Nonbilayer Structures in Diacylphosphatidylcholine Model Membranes by Transmembrane α -Helical Peptides: Importance of Hydrophobic Mismatch and Proposed Role of Tryptophans. *Biochemistry.* 35: 1037–1045.
24. Vostrikov, V. V, A.E. Daily, D. V Greathouse, and R.E. Koeppe. 2010. Charged or aromatic anchor residue dependence of transmembrane peptide tilt. *J. Biol. Chem.* 285: 31723–30.
25. Andersen, O.S., and R.E. Koeppe. 2007. Bilayer thickness and membrane protein function: an energetic perspective. *Annu. Rev. Biophys. Biomol. Struct.* 36: 107–130.
26. Gleason, N.J., V. V Vostrikov, D. V Greathouse, C. V Grant, S.J. Opella, and R.E. Koeppe. 2012. Tyrosine replacing tryptophan as an anchor in GWALP peptides. *Biochemistry.* 51: 2044–53.
27. Sparks, K.A., N.J. Gleason, R. Gist, R. Langston, D. V Greathouse, and R.E. Koeppe. 2014. Comparisons of interfacial Phe, Tyr, and Trp residues as determinants of orientation and dynamics for GWALP transmembrane peptides. *Biochemistry.* 53: 3637–45.

28. Mortazavi, A., V. Rajagopalan, K.A. Sparks, D. V. Greathouse, and R.E. Koeppe. 2016. Juxta-terminal Helix Unwinding as a Stabilizing Factor to Modulate the Dynamics of Transmembrane Helices. *ChemBioChem*. 17: 462–465.
29. Almén, M.S., K.J. V Nordström, R. Fredriksson, and H.B. Schiöth. 2009. Mapping the human membrane proteome: a majority of the human membrane proteins can be classified according to function and evolutionary origin. *BMC Biol*. 7: 50.
30. Krogh, A., B. Larsson, G. von Heijne, and E.L. Sonnhammer. 2001. Predicting transmembrane protein topology with a hidden Markov model: application to complete genomes. *J. Mol. Biol.* 305: 567–80.
31. Sharpe, H.J., T.J. Stevens, and S. Munro. 2010. A comprehensive comparison of transmembrane domains reveals organelle-specific properties. *Cell*. 142: 158–69.
32. Kingsley, P. B., Feigenson, G.W. 1979. The Synthesis of a Perdeuterated Phospholipid: 1,2-dimyristoyl-sn-glycero-3-phosphocholine-d72. *Chem. Phys. Lipids*. 24: 135–147.
33. Akashi, K., H. Miyata, H. Itoh, and K. Kinoshita. 1996. Preparation of giant liposomes in physiological conditions and their characterization under an optical microscope. *Biophys. J.* 71: 3242–50.
34. Usery, R.D., T.A. Enoki, S.P. Wickramasinghe, M.D. Weiner, W.-C. Tsai, M.B. Kim, S. Wang, T.L. Torng, D.G. Ackerman, F.A. Heberle, J. Katsaras, and G.W. Feigenson. 2017. Line Tension Controls Liquid-Disordered + Liquid-Ordered Domain Size Transition in Lipid Bilayers. *Biophys. J.* 112: 1431–1443.
35. Buboltz, J.T., and G.W. Feigenson. 1999. A novel strategy for the preparation of liposomes: rapid solvent exchange. *Biochim. Biophys. Acta - Biomembr.* 1417: 232–245.
36. Buboltz, J.T. 2007. Steady-state probe-partitioning fluorescence resonance energy transfer: A simple and robust tool for the study of membrane phase behavior. *Phys. Rev. E - Stat. Nonlinear, Soft Matter Phys.* 76: 1–7.
37. Wu, Y., H.W. Huang, and G.A. Olah. 1990. Method of oriented circular dichroism. *Biophys. J.* 57: 797–806.
38. Ladokhin, A.S., M. Fernández-Vidal, and S.H. White. 2010. CD Spectroscopy of Peptides and Proteins Bound to Large Unilamellar Vesicles. *J. Membr. Biol.* 236: 247–253.
39. Heberle, F.A., R.S. Petruzielo, J. Pan, P. Drazba, N. Kučerka, R.F. Standaert,

- G.W. Feigenson, and J. Katsaras. 2013. Bilayer thickness mismatch controls domain size in model membranes. *J. Am. Chem. Soc.* 135: 6853–9.
40. Thomas, R., V. V Vostrikov, D. V Greathouse, and R.E. Koeppe II. 2009. Influence of Proline upon the Folding and Geometry of the WALP19 Transmembrane Peptide. *pubs.acs.org/Biochemistry*. .
 41. Killian, J.A. 2003. Synthetic peptides as models for intrinsic membrane proteins. *FEBS Lett.* 555: 134–138.
 42. Kelly, S.M., T.J. Jess, and N.C. Price. 2005. How to study proteins by circular dichroism. *Biochim. Biophys. Acta - Proteins Proteomics.* 1751: 119–139.
 43. Beaven, A.H., A.J. Sodt, R.W. Pastor, R.E. Koeppe, O.S. Andersen, W. Im, and W. Im. 2017. Characterizing Residue-Bilayer Interactions Using Gramicidin A as a Scaffold and Tryptophan Substitutions as Probes. *J. Chem. Theory Comput.* 13: 5054–5064.
 44. De Planque, M.R.R., D. V. Greathouse, R.E. Koeppe, H. Schäfer, D. Marsh, and J.A. Killian. 1998. Influence of lipid/peptide hydrophobic mismatch on the thickness of diacylphosphatidylcholine bilayers. A ²H NMR and ESR study using designed transmembrane α -helical peptides and gramicidin A. *Biochemistry.* 37: 9333–9345.
 45. Francis, A. 1963. *Liquid-liquid equilibria*. New York: Interscience Publishers.
 46. Rawicz, W., K.C. Olbrich, T. McIntosh, D. Needham, and E. Evans. 2000. Effect of chain length and unsaturation on elasticity of lipid bilayers. *Biophys. J.* 79: 328–39.
 47. Bermúdez, H., D.A. Hammer, and D.E. Discher. 2004. Effect of Bilayer Thickness on Membrane Bending Rigidity. *Langmuir.* 20: 540–543.
 48. Pécrcéaux, J., H.G. Döbereiner, J. Prost, J.F. Joanny, and P. Bassereau. 2004. Refined contour analysis of giant unilamellar vesicles. *Eur. Phys. J. E.* 13: 277–290.
 49. Pan, J., S. Tristram-Nagle, and J.F. Nagle. 2009. Effect of cholesterol on structural and mechanical properties of membranes depends on lipid chain saturation. *Phys. Rev. E. Stat. Nonlin. Soft Matter Phys.* 80: 21931.
 50. Quehenberger, O., A.M. Armando, A.H. Brown, S.B. Milne, D.S. Myers, A.H. Merrill, S. Bandyopadhyay, K.N. Jones, S. Kelly, R.L. Shaner, C.M. Sullards, E. Wang, R.C. Murphy, R.M. Barkley, T.J. Leiker, C.R.H. Raetz, Z. Guan, G.M. Laird, D.A. Six, D.W. Russell, J.G. McDonald, S. Subramaniam, E. Fahy, and E.A. Dennis. 2010. Lipidomics reveals a remarkable diversity of lipids in

- human plasma. *J. Lipid Res.* 51: 3299–305.
51. Sampaio, J.L., M.J. Gerl, C. Klose, C.S. Ejsing, H. Beug, K. Simons, and A. Shevchenko. 2011. Membrane lipidome of an epithelial cell line. *Proc. Natl. Acad. Sci.* 108: 1903–1907.
 52. van Meer, G., D.R. Voelker, and G.W. Feigenson. 2008. Membrane lipids: where they are and how they behave. *Nat. Rev. Mol. Cell Biol.* 9: 112–124.
 53. Evans, E., and W. Rawicz. 1990. Entropy-Driven Tension and Bending Elasticity in Condensed-Fluid Membranes. 64.
 54. Khelashvili, G., B. Kollmitzer, P. Heftberger, G. Pabst, and D. Harries. 2013. Calculating the Bending Modulus for Multicomponent Lipid Membranes in Different Thermodynamic Phases. *J. Chem. Theory Comput.* 9: 3866–3871.
 55. Semrau, S., T. Idema, L. Holtzer, T. Schmidt, and C. Storm. 2008. Accurate Determination of Elastic Parameters for Multicomponent Membranes. *Phys. Rev. Lett.* 100: 88101.
 56. Pan, J., S. Tristram-Nagle, N. Kučerka, and J.F. Nagle. 2008. Temperature Dependence of Structure, Bending Rigidity, and Bilayer Interactions of Dioleoylphosphatidylcholine Bilayers. *Biophys. J.* 94: 117–124.
 57. Henriksen, J., A.C. Rowat, and J.H. Ipsen. 2004. Vesicle fluctuation analysis of the effects of sterols on membrane bending rigidity. *Eur. Biophys. J.* 33: 732–741.
 58. Sengupta, P., A. Hammond, D. Holowka, and B. Baird. 2008. Structural determinants for partitioning of lipids and proteins between coexisting fluid phases in giant plasma membrane vesicles. *Biochim. Biophys. Acta - Biomembr.* 1778: 20–32.
 59. Sevcsik, E., M. Brameshuber, M. Fölser, J. Weghuber, A. Honigmann, and G.J. Schütz. 2015. GPI-anchored proteins do not reside in ordered domains in the live cell plasma membrane. *Nat. Commun.* 6: 6969.
 60. Kahya, N., D.A. Brown, and P. Schwille. 2005. Raft partitioning and dynamic behavior of human placental alkaline phosphatase in giant unilamellar vesicles. *Biochemistry.* 44: 7479–7489.
 61. Levental, I., D. Lingwood, M. Grzybek, U. Coskun, and K. Simons. 2010. Palmitoylation regulates raft affinity for the majority of integral raft proteins. *Proc. Natl. Acad. Sci. U. S. A.* 107: 22050–4.
 62. Dupuy, A.D., and D.M. Engelman. 2008. Protein area occupancy at the center of the red blood cell membrane. *Proc. Natl. Acad. Sci. U. S. A.* 105: 2848–52.

63. Sheetz, M.P. 1993. Glycoprotein motility and dynamic domains in fluid plasma membranes. *Annu. Rev. Biophys. Biomol. Struct.* 22: 417–31.
64. Ackerman, D.G., and G.W. Feigenson. 2016. Effects of Transmembrane α -Helix Length and Concentration on Phase Behavior in Four-Component Lipid Mixtures: A Molecular Dynamics Study. *J. Phys. Chem. B.* 120: 4064–4077.
65. Bloom, M., E. Evans, and O.G. Mouritsen. 1991. Physical properties of the fluid lipid-bilayer component of cell membranes: a perspective. *Q. Rev. Biophys.* 24: 293–397.

Chapter 3

Line tension controls liquid-disordered + liquid-ordered domain size transition in lipid bilayers*

3.1 Abstract

To better understand animal cell plasma membranes, we studied simplified models, namely four-component lipid bilayer mixtures. Here we describe the domain size transition in the region of coexisting liquid-disordered (Ld) + liquid-ordered (Lo) phases. This transition occurs abruptly in composition space with domains increasing in size by two orders of magnitude, from tens of nanometers to microns. We measured the line tension between coexisting Ld and Lo domains close to the domain size transition for a variety of lipid mixtures, finding that in every case the transition occurs at a line tension of ~ 0.3 pN. A computational model incorporating line tension and dipole repulsion indicated that even small changes in line tension can result in domains growing in size by several orders of magnitude, consistent with experimental observations. We find that other properties of the coexisting Ld and Lo phases do not change significantly in the vicinity of the abrupt domain size transition.

*Usery R ^Δ, Enoki T ^Δ, Wickramasinghe S, Weiner M, Tsai W, Kim M, Torng T, Ackerman D, Heberle F, Katsaras J, Feigenson G. 2017. Line Tension Controls Liquid-Disordered + Liquid-Ordered Domain Size Transition in Lipid Bilayers. *Biophys J.* 112(7):1431-1443.

^ΔRebecca D. Usery and Thais A. Enoki contributed equally to this work.

3.2 Introduction

Phase separation in the plasma membrane (PM) would have important implications for the life of a cell. PM properties could then change sharply over a small range of temperature or composition. Any factor that changes the energy per unit length of the interface (i.e., the line tension) could drive changes in interface length and thus domain size. However, the characterization of phase separation in cells has remained elusive due in part to the complexity of the PM: the lipid and protein components are numerous and diverse (1–4), the two bilayer leaflets have very different compositions, and leaflet coupling is poorly understood (5).

The complexity of the PM makes chemically well-defined model membranes a valuable tool for studying principles governing phase coexistence. Phase diagrams are useful for describing the phase regions and the compositional ranges relevant to the PM. As shown in Figure 3.1, coexistence of liquid-ordered (Lo) and liquid-disordered (Ld) phases occurs in mixtures of high melting temperature (highT_m) lipids, low melting temperature (lowT_m) lipids, and cholesterol (chol) (6–9). Domain size in the Ld + Lo region can be tuned by composition alone in mixtures of this type (10). At one extreme, domain growth is limited to the nanometer size scale, as found for 1,2-distearoyl-*sn*-glycero-3-phosphocholine (DSPC)/1-palmitoyl-2-oleoyl-*sn*-glycero-3-phosphocholine (POPC)/chol (11, 12). At the other extreme, domain growth is limited only by vesicle size; in these mixtures, domains in giant unilamellar vesicles (GUVs) are many microns in diameter, as with DSPC/1,2-dioleoyl-*sn*-glycero-3-phosphocholine (DOPC)/chol (7).

For convenience, we refer to these extreme cases as nanodomains and macrodomains, respectively.

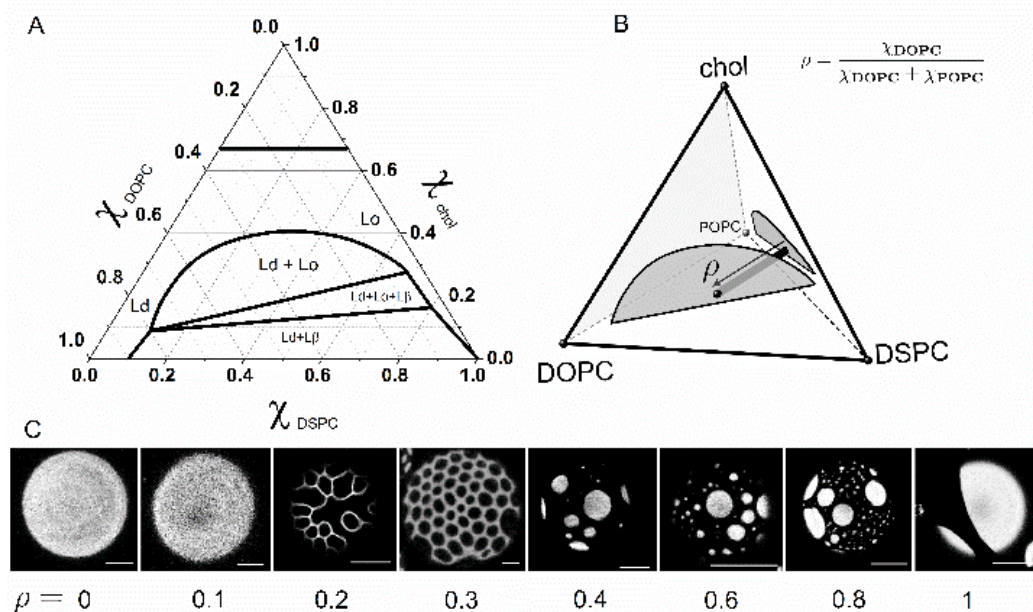


FIGURE 3.1. Phase diagrams and phase morphologies in four-component mixtures. (A) Ternary phase diagram of DSPC/DOPC/Chol at 23°C (9). (B) Partial quaternary (tetrahedral) phase diagram of DSPC/DOPC/POPC/chol showing the Ld+Lo regions (shaded) of DSPC/DOPC/chol (near face) and DSPC/POPC/chol (far right face) (9). Sample series referred to in the main text as “ ρ trajectories” connect a composition on the DSPC/POPC/chol face ($\rho = 0$, nanodomains) to a composition on the DSPC/DOPC/chol face ($\rho = 1$, macrodomains), where ρ represents the ratio of DOPC to total lowTm lipid (i.e., DOPC + POPC). (C) Phase morphologies observed in GUVs along a ρ trajectory in DSPC/DOPC/POPC/chol: uniform ($\rho < 0.2$); modulated ($0.2 \leq \rho < 0.4$); macroscopic round domains ($\rho \geq 0.4$). Images were collected with a confocal microscope using 0.02 mol% C12:0 DiI. Scale bars 10 μm .

Studies of the four-component mixture DSPC/DOPC/POPC/chol revealed that Ld + Lo domains remain nanoscopic at low DOPC fraction until an abrupt 100-fold size change of occurs at higher DOPC fraction (10, 13). As we show here both experimentally and by modeling, increasing line tension drives this nano-to-macro transition. In the course of this size transition, macroscopic patterning of phases or “modulated phase morphology” occurs (10, 14). These patterns result from curvature energies that compete with line tension on a round vesicle to break up domains (15–17). The transition from nanometer-scale to micron-scale domains is apparent by imaging giant vesicles: GUVs appear uniform, then patterned, and then with large rounded domains as the compositional range is traversed (10, 13).

The abrupt domain size change that occurs with changing mixture composition is the main subject of this work. We show in six different mixtures how line tension increases abruptly when visible domains first appear. In contrast, we find that other properties of Ld and Lo phases do not change sharply even when the domain size does. We propose a model for this abrupt transition in which domain size is determined by a competition between line tension and dipole repulsion. Our results have implications for both how cells could potentially change domain size and what interactions could be responsible for the small size of domains in the PM.

3.3 Materials and Methods

3.3.1 Materials

Phospholipids were purchased from Avanti Polar Lipids (Alabaster, AL). Purity of phospholipids was found to be better than 99.5% using thin layer chromatography (TLC). Briefly, about 20 μg of lipid was spotted on washed and activated Adsorbosil TLC plates (Alltech, Deerfield, IL) and developed in the solvent system chloroform/methanol/water = 65/25/4. Phospholipid concentrations were determined by inorganic phosphate assay (18), with an error < 1% from 10 replicates. Chol was from Nu Chek Prep, Inc. (Elysian, MN), and its stock solutions were made at defined concentrations using standard gravimetric procedures. The fluorescent dyes, C12:0 DiI (1,1'-didodecyl-3,3,3',3'-tetramethylindocarbocyanine perchlorate) and Bodipy-PC (2-(4,4-difluoro-5,7-dimethyl-4-bora-3a,4a-diaza-s-indacene-3-pentanoyl)-1-hexadecanoyl-*sn*-glycero-3-phosphocholine), were from Invitrogen (Carlsbad, CA). Concentrations were determined by absorption spectroscopy using extinction coefficients of $143,000 \text{ M}^{-1}\text{cm}^{-1}$ and $91,800 \text{ M}^{-1}\text{cm}^{-1}$, respectively. Spin-labeled lipid 1-palmitoyl-2-(16-doxyyl stearoyl) phosphatidylcholine (16PC) was a gift from Boris Dzikovski of the National Biomedical Center for Advanced Electron Spin Resonance (ESR) Technology at Cornell University. F^{4,5}GWALP23 synthesized according to (19) was a gift from Roger Koeppe and Denise Greathouse. The peptide was dissolved in 2,2,2-trifluoroethanol purchased from Sigma-Aldrich (St. Louis, MO), with the peptide concentration measured by tryptophan absorbance at 280 nm of a 1:500 dilution in methanol, using an extinction coefficient of $5500 \text{ M}^{-1}\text{cm}^{-1}$. The buffer used in fluorescence experiments contained 5 mM PIPES (Sigma-Aldrich), 200 mM KCl (Sigma-Aldrich), and 1 mM EDTA (Sigma-Aldrich), at pH 7.0. Sucrose was from Fisher Scientific (Fair Lawn, NJ), and glucose from Teknova (Hollister, CA).

3.3.2 Composition conventions used

Lipid composition and the phase boundaries of each mixture are the key variables in this work, as shown in Figure 3.1. We studied lipid mixtures of the type highT_m lipid/lowT_m phosphatidylcholines (PCs)/chol: N-palmitoyl-D-*erythro*-sphingosylphosphorylcholine (PSM)/DOPC/POPC/chol; egg sphingomyelin (eSM)/DOPC/1-stearoyl-2-oleoyl-*sn*-glycero-3-phosphocholine (SOPC)/chol; eSM/DOPC/POPC/chol; DSPC/1,2-diphytanoyl-*sn*-glycero-3-phosphocholine (DPhPC)/1,2-dilauroyl-*sn*-glycero-3-phosphocholine (DLPC)/chol; DSPC/DPhPC/POPC/chol; DSPC/DOPC/POPC/chol; brain sphingomyelin (bSM)/DOPC/POPC/chol; bSM/DOPC/1-palmitoyl-2-linoleoyl-*sn*-glycero-3-phosphocholine (16:0,18:2PC)/chol; bSM/DOPC/SOPC/chol; and bSM/1-stearoyl-2-docosahexaenoyl-*sn*-glycero-3-phosphocholine (SDPC)/POPC/chol. For Molecular Dynamics (MD) simulations we used the mixture 1,2-dipalmitoyl-*sn*-glycero-3-phosphocholine (DPPC)/1,2-dilinoleoyl-*sn*-glycero-3-phosphocholine (DUPC)/1-palmitoyl-2-linoleoyl-*sn*-glycero-3-phosphocholine (PUPC)/chol. For all mixtures we define a key compositional parameter, the replacement ratio ρ (10, 13, 17), as the replacement of lowT_m nanodomain-forming PC for lowT_m macrodomain-forming PC. For example, when POPC is replaced by DOPC, $\rho = [\text{DOPC}]/[\text{DOPC} + \text{POPC}]$ (Figure 3.1 B), and when SOPC is replaced by DOPC, $\rho = [\text{DOPC}]/[\text{DOPC} + \text{SOPC}]$. For experiments at a single ρ value, we describe the lipid composition with the mole fraction of each mixture component, e.g. DSPC/DOPC/POPC/chol = 0.39/0.35/0.04/0.22 for $\rho = 0.1$, and for experiments along ρ , composition is noted as DSPC/DOPC+POPC/chol = 0.39/0.39/0.22.

3.3.3 GUV preparation and phase morphology determination

GUVs were made by electroformation (20) with modifications. Briefly, each sample contained ~ 300 nmol of a lipid mixture in 200 μ L chloroform. A lipid film was created by evenly spreading the chloroform solution on indium tin oxide (ITO)-coated microscope slides (Delta Technologies, Stillwater, MN) pre-warmed on a hotplate with surface temperature measured at ~ 50 °C. After residual solvent was removed under vacuum for 2 h at ~ 50 mTorr, ITO slides were sealed with Buna-N O-rings to create a chamber, which was then filled with 100 mM sucrose solution. Films were held above the transition temperature for 2 h in an AC field of 5 Hz, \pm 1 Vpp, using a Wavetek FG2C function generator (Meterman, Everett, WA), followed by cooling to 23 °C using a Digi-sense temperature controller R/S (Cole Palmer, Vernon Hills, IL). Cooling rates for line tension measurements were varied in order to control domain size as described in the Supporting Materials in Appendix B, and line tension was found to be independent of cooling rate (Figure B.4). GUVs were harvested into 100 mM glucose solution then allowed to settle for 1 h to remove debris before microscopy observations at 23 °C. A widefield microscope, Nikon Eclipse Ti (Nikon Instruments, Melville, NY) equipped with a 60x/1.2 NA water immersion objective, was used for all image-based experiments except partition coefficient determination, where a Nikon Eclipse C2+ confocal microscope was used. To keep the harvested GUVs intact, an osmolality difference between the sucrose and glucose solutions of < 5 mOsmol/kg H₂O was ensured with the use of an osmometer (Model 5004, Precision Systems Inc., Natick, MA).

GUVs were visualized at 23 °C using a widefield fluorescence microscope. Sample chambers for observation consisted of a no. 1.5 coverslip and traditional microscope slide separated with a silicone spacer (Sigma-Aldrich, St. Louis, MO) of 0.25 mm thickness. Fields of view were selected with brightfield illumination before fluorescent images were acquired from emission of C12:0-DiI, which partitions into the Ld phase (21). For phase morphology determination we used this probe at 0.02 mol% of total lipid in the sample to limit light-induced artifacts (22). Images were acquired using a Zyla 5.5 sCMOS camera (Andor Technology, Ltd., Belfast, UK). For each field of GUVs appearing to be free of defects (e.g., multiple layers or tethers), a series of approximately five 200 ms exposures was taken to capture the surface of GUVs opposite the coverslip. At various values of ρ for the four-component mixtures in this study, the numbers of GUVs with uniform, modulated, and macroscopic patterns were counted. GUVs appearing uniform but with compositions found by spectroscopic methods to have coexisting Lo and Ld phases (8, 9, 23) were counted as nanoscopic, as in Figure 3.1 C $\rho = 0$ and 0.1. GUVs at intermediate ρ values exhibiting thin stripes or non-rounded small domains were considered to be modulated, as in Figure 3.1 C $\rho = 0.2$ and 0.3. Macroscopic GUVs were counted as those with large, rounded domains.

3.3.4 Line tension measurements

Line tension was measured using the flicker spectroscopy method of Esposito et al. (24). Briefly, the fluctuation spectrum of a phase domain boundary on a GUV is decomposed into Fourier modes that are related to line tension by

$$\langle |u_n|^2 \rangle = \frac{2k_B T}{\sigma \pi R_0 (n^2 - 1)}, \quad (3.1)$$

where n is the mode number, u_n is the mode amplitude, σ is the line tension, R_0 is the radius of a circle yielding the domain area, k_B is the Boltzmann constant, and T is the absolute temperature. For all measurements discussed below, the line tension value was the same whether the fluctuating domain was Ld or Lo and was independent of GUV size or domain size, as shown in more detail in Figure B.5. Additional details of the microscope setup, cooling methods, analysis methodology, and line tension controls are in Appendix B.

3.3.5 Bending energy measurements

Bending moduli were measured by fluctuation analysis of GUVs. Fluctuations at the GUV equator were observed by phase contrast microscopy (Figure B.8 A). Fluctuation spectra obtained from GUV contours were used to calculate the bending modulus through the relationship

$$\langle |u(q)|^2 \rangle = \frac{k_B T}{\kappa q^4 + \sigma q^2}, \quad (3.2)$$

where $u(q)$ is the displacement normal to the membrane, $q = (qx, qy)$ is the wave vector corresponding to the displacement, k_B is the Boltzmann constant, T is the absolute temperature, κ is the bending modulus, and σ is membrane tension. Tension was determined as in (25), and the bending modulus calculated as in (26). Additional information on measurement methods is provided in Appendix B.

The bending moduli of the coexisting phases were determined by measuring *single-phase* *GUVs* at the Ld and Lo tieline endpoint compositions at various values of ρ for DSPC/DOPC/POPC/chol. Tieline endpoint compositions near the lower boundary of the Ld + Lo region were taken from (9) and are provided in Table B.1.

3.3.6 Partition coefficient (K_p) measurements

Determination of 16PC K_p from ESR spectra.

One hundred eleven samples were prepared along a ρ trajectory of DSPC/DOPC + POPC/chol = 0.39/0.39/0.22 from $\rho = 0$ to 1, with all samples having coexisting Ld + Lo phases. Lipid stock solutions were combined with 0.3 mol% of the spin-labeled lipid 16PC. Chloroform was then removed under nitrogen flow, followed by high vacuum for 8 h. Lipid mixtures were hydrated with 18 M Ω -cm water (EMD Millipore, Billerica, MA) at 47 °C for 1 h, vortexing every 15 min. Samples were centrifuged at 14,000 \times g for 30 min to form lipid pellets, and the supernatant removed. Pellets were transferred into ESR capillary sample tubes and centrifuged again with a hematocrit centrifuge at 3,300 \times g for 30 min before the tubes were sealed. Samples were held at room temperature for a minimum of 5 h after centrifugation before recording spectra on a Bruker ELEXSYS E500 CW ESR Spectrometer operated at X-band frequency (9.4 GHz) with 0.5 Gauss modulation. Reported spectra are the average of 16 scans obtained at 20–24 °C.

ESR spectra were modeled as a linear combination of Ld- and Lo-phase spectra with relative amounts corresponding to the relative fraction of 16PC in either phase (27–29). We analyzed the composite Ld + Lo spectrum for each ρ value using the corresponding tieline endpoint Ld and Lo spectra, assuming the tieline endpoint Ld and Lo spectra changed linearly with ρ . In fact, the Ld and Lo spectra changed little over the entire range of ρ from 0 to 1. Fitting was performed by least squares minimization of the entire spectrum. Details of the fitting procedure are found in Appendix B. Using the fitted fractions of 16PC in the two phases, K_p values were determined by comparing the fraction of 16PC in either phase to the phase mole fraction obtained from the Lever-Arm Rule on the corresponding tielines (8). We use the convention that $K_p > 1$ corresponds to preference for Ld phase. For $\rho = 0, 0.3,$ and 1 the tieline endpoint Ld and Lo ESR spectra were simulated (see Figure B.13) with Non-Linear Least Squares (NLSL) Analysis of Slow-Motional ESR Spectra (27–29).

Determination of Bodipy-PC K_p from fluorescence measurements.

Bodipy-PC K_p was measured in bSM/DOPC/POPC/chol both spectrophotometrically in a cuvet, and in GUVs with a confocal fluorescence microscope, in both cases using a dye/lipid ratio of 1/2500. For single-dye fluorescence experiments, typically 61 samples were prepared along a tieline. Phospholipid, chol and dye were added in a glass tube using a repeating dispenser and a glass syringe. Aqueous buffer was added to each sample, and chloroform removed by Rapid Solvent Exchange (RSE) as previously described (30), except that the equilibration started at 55 °C, with cooling at 2 °C/h to 23 °C. Steady-state fluorescence was measured at ambient

temperature (23 °C) with excitation/emission wavelengths at 500/520 nm, slits 5/5 nm, and 10 s integration time using a Hitachi F-7000 FL spectrofluorimeter (Hitachi High Technologies America, Inc., Schaumburg, IL). K_p values were determined as above (8). For microscopy experiments, GUVs of bSM/DOPC+POPC/Chol = 0.40/0.40/0.20 were formed by electroformation. Images were obtained at 23 °C with a 60× water immersion objective. Additional details of K_p determination, including line scan protocols and self-quenching corrections, are described in Appendix B.

3.3.7 Model for calculating equilibrium domain size

Our approach to modeling domain size is to identify an interaction that could compete with line tension but not scale linearly with line tension. Dipole repulsion within the bilayer could be such an interaction, as described by Amazon and Feigensohn (31). An initial question is whether dipoles in one leaflet would have their fields largely cancelled by the opposing dipoles in the other leaflet. This does occur for the terminal methyl dipoles that give rise to long-range repulsion in lipid monolayers (32), but the dipoles of interest in this study are located farther apart in the interfacial region.

To explore the implications of dipole repulsion for domain size, we modeled the total energy of a phase-separated bilayer as a sum of a phase boundary energy from line tension E_{perim} that scales with domain perimeter and an electrostatic potential energy E_{elec} arising from permanent lipid dipoles, with $E_{total} = E_{perim} + E_{elec}$. For N_D domains of total area α , $E_{perim} = 2\pi R_D N_D \sigma$, where σ is the line tension and $R_D =$

$\sqrt{\alpha/(\pi N_D)}$ is the domain radius. For lipids distributed identically in the two bilayer leaflets and dipoles aligned with the bilayer normal, the total electrostatic potential energy of the bilayer is a sum of intra- and interleaflet contributions, i.e. $E_{elec} = 2V_{intra} + V_{inter}$, and

$$V_{intra} = N_D \frac{1}{2} \frac{N_L^2}{4\pi\epsilon\epsilon_0} \int_a^{2R_D} \frac{(\Delta\phi\epsilon\epsilon_0 A_L)^2}{r^3} P(r, R_D) dr, \quad (3)$$

$$V_{inter} = N_D \frac{N_L^2}{4\pi\epsilon\epsilon_0} \int_0^{2R_D} \left[\frac{3(h\Delta\phi\epsilon\epsilon_0 A_L)^2}{(h^2+r^2)^{5/2}} - \frac{(\Delta\phi\epsilon\epsilon_0 A_L)^2}{(h^2+r^2)^{3/2}} \right] P(r, R_D) dr, \quad (4)$$

where N_L is the total number of lipid dipoles per leaflet in the domain, A_L is the average lipid molecular area, h is the separation distance between opposing dipole layers, ϵ_0 is the permittivity of free space, ϵ is the dielectric constant (here, the dielectric constant of the bilayer region near the dipoles), $a = 2\sqrt{A_L/\pi}$ (the lower limit of the V_{intra} integral) is the distance of closest approach between two dipoles, and $\Delta\phi$ is the electrostatic potential difference between the domain and surrounding phase. The distribution of dipole separation distances $P(r, R_D)$ within the domain is given by the pair-distance distribution function for a disk (33),

$$P(r, R_D) = \frac{r}{\pi R_D^3} \left\{ 4R_D \tan^{-1} \left[\frac{R_D}{r} \sqrt{4 - (r/R_D)^2} \right] - r \sqrt{4 - (r/R_D)^2} \right\}. \quad (5)$$

This model does not explicitly treat the influence of the water and ionic strength. Instead, we made use of the finding by Zhou and Schulten that the contribution of the lipid headgroups and the oriented water nearly cancel, so that the measured membrane dipole potential is determined by the lipid ester moieties (34). Additional details and a full derivation are found in Appendix B.

3.3.8 Nanodomain size measurements

Large unilamellar vesicle (LUV) samples for domain size measurements were prepared as follows. Lipid mixtures were prepared by transferring volumes of lipids and chol stocks in chloroform to a glass vial with a glass syringe (Hamilton USA, Reno, NV). Organic solvent was removed with a nitrogen stream and gentle heating, followed by vacuum drying for > 12 h. Dry lipid films were hydrated with a 34.5 % (v/v) D₂O/H₂O mixture preheated to 50 °C and vortexed to generate multilamellar vesicles (MLVs). The MLV suspension was incubated at 50 °C for 1 h, followed by 5 freeze/thaw cycles between -80 and 50 °C. LUVs were prepared using a miniextruder (Avanti Polar Lipids) assembled with a single polycarbonate filter (30, 50, 100, or 200 nm diameter pore size) and heated to 50 °C. Final sample concentrations were 10–20 mg/mL, which allowed for sufficient water between vesicles to eliminate the interparticle structure factor (35).

Small-angle neutron scattering (SANS) experiments were conducted at Oak Ridge National Laboratory (ORNL), using both the CG-3 BioSANS instrument of the High Flux Isotope Reactor (HFIR) and the BL-6 extended Q-range small-angle neutron scattering (EQ-SANS) instrument of the Spallation Neutron Source (SNS). LUV suspensions were loaded into 1 mm path-length quartz banjo cells (Hellma USA, Plainview, NY) and mounted in a temperature-controlled cell holder with ~ 1°C accuracy. BioSANS data were collected at a 14.5 m sample-to-detector distance (SDD) using 6 Å wavelength neutrons (FWHM 15%), resulting in a total scattering vector of

$0.005 < q < 0.06 \text{ \AA}^{-1}$. EQ-SANS data were taken at a 4.0 m SDD with a 6.0–9.5 \AA wavelength band for a total scattering vector of $0.01 < q < 0.1 \text{ \AA}^{-1}$. Scattered neutrons were collected with a two-dimensional ($1 \times 1 \text{ m}$) ^3He position-sensitive detector (ORDELA, Inc., Oak Ridge, TN) with 192×192 pixels (BioSANS) or 256×192 pixels (EQ-SANS). The 2D data were reduced using Mantid software (36). During reduction, data were corrected for detector pixel sensitivity, dark current, and sample transmission, and the background scattering from water was subtracted. The one-dimensional scattering intensity $I(q)$ [$q = 4\pi \sin(\theta)/\lambda$, where λ is the neutron wavelength and 2θ is the scattering angle relative to the incident beam] was obtained by radial averaging of the corrected 2D data.

Nanodomain sizes were determined by analysis of $I(q)$ data using a coarse-grained Monte Carlo method described elsewhere (11, 37). Additional details are found in Appendix B.

3.3.9 Molecular dynamics (MD) simulations

Coarse grained MD simulations were performed to characterize the size, shape, and dynamics of nanodomains. Simulations of phase-separated DPPC/DUPC/PUPC/chol systems with 20,000 total lipids were examined at ρ values 0.5, 0.65, and 0.8. The simulations contained approximately four times as many lipids as previously studied for an identical composition (38), enabling consideration of the effect of system size on measured nanodomain properties. Bilayers were constructed using the CHARMM-GUI tool and then tiled to quadruple system size (39–42). The

Martini force field (version 2.1) was implemented in GROMACS 4.6.6 (43–46) using an NPT ensemble with a 30 fs time step under periodic boundary conditions in a box approximately $74 \times 74 \times 12$ nm. A temperature of 295 K and pressure of 1 atm were maintained by a V-rescale thermostat (time constant 1 ps) and semi-isotropic Parrinello-Rahman barostat (time constant 12 ps), respectively. Temperature bath coupling was separate for lipids and solvent. The GPU-compatible Verlet cutoff scheme was used with electrostatic and van der Waals potentials shifted to reach zero at 1.1 nm. Center of mass motion was removed each 10 time steps. All simulations were conducted on Titan at the Oak Ridge Leadership Computing Facility.

Analysis was performed using a custom Python script incorporating the MDTraj library (47). A Voronoi tessellation of lipids in a single leaflet determined each molecule's nearest neighbors as those with which it shared a Voronoi ridge. Phase determination for each lipid was based on the lipid and its nearest neighbors, with enrichment in DPPC and chol serving as a marker of the Lo phase, and depletion of these lipids a marker of the Ld phase. For details, see Appendix B.

3.4 Results

The mixtures examined here are described by phase diagrams of the type shown in Figure 3.1 A for a three-component lipid mixture of DSPC/DOPC/chol (9). More generally, this phase behavior occurs for mixtures of the type (highTm PC or sphingomyelin)/(lowTm PC)/chol, as found by several researchers (48, 49). Important for our studies is that a mixture is separated into immiscible liquid domains. To study

this behavior, we employ vesicles of different size and lamellarity (LUVs, GUVs, and MLVs) as dictated by the constraints of different experimental techniques. Whereas vesicle size constrains the maximum possible domain size, curvature has no measurable effect on the structure of PC bilayers for vesicle diameters larger than 50 nm (35, 53) as used in this study. Furthermore, although the presence of multiple lamellae increases the cooperativity of phase transitions in single component bilayers, the same transitions are nevertheless seen in LUVs, GUVs and MLVs (50). These findings suggest that vesicle size and curvature do not significantly affect phase behavior.

Phase boundaries, as shown in Figure 3.1 A, have been determined as described elsewhere (7–9, 23), mainly using steady-state fluorescence spectroscopy, fluorescence microscopy, ESR and differential scanning calorimetry. Other researchers have found similar boundaries by use of Nuclear Magnetic Resonance (NMR) and X-ray diffraction (48, 51, 52). The mixture DSPC/POPC/chol is described by a similar phase diagram to that in Figure 3.1 A (9), except that the coexistence of Ld + Lo domains was detected by Förster resonance energy transfer (FRET), ESR, and SANS, but not visualized with optical microscopy, suggesting domains of a size below the optical resolution limit (11, 12). In the four-component lipid mixture DSPC/DOPC/POPC/chol, this transition can be explored with the replacement of POPC by DOPC, where $\rho = [\text{DOPC}]/[\text{DOPC} + \text{POPC}]$, as in Figure 3.1 B. As described below, we measured how physical properties, including domain size, line tension, bending rigidity, order and rotational diffusion of a probe, and probe partitioning, change along this ρ -trajectory.

3.4.1 Domain size exhibits an abrupt transition with composition that is correlated with line tension

We recorded the visual appearance of domains examined in GUVs with fluorescence microscopy. Figure 3.1 *C* shows images of GUVs composed of DSPC/DOPC/POPC/chol having compositions along a ρ trajectory and is a representative example for all mixtures studied. For $\rho = 0$ and 0.1, GUVs appeared uniform, but FRET, ESR and SANS studies revealed nanodomains with sizes below optical resolution (8, 9, 23). At higher ρ values from 0.4–1, GUVs exhibited large, round domains with micron-sized diameters. In the course of the transition between GUVs with uniform appearance and GUVs with large and round domains, we observed a composition range where GUVs showed modulated phase patterns; we previously termed this region the “ ρ -window” (9, 10, 13, 17). Figure 3.1 *C* reveals modulated phases for DSPC/DOPC/POPC/chol at $\rho = 0.2$ and 0.3. These modulated phase patterns mark the first appearance of visible domains, and thus a pronounced change in domain size from tens of nanometers to microns.

Similar abrupt domain size transitions were observed for 12 other mixtures, although at different ρ values for each mixture, as shown in Figure 3.2. The fraction of GUVs exhibiting either modulated phases or round macroscopic domains is indicated by a solid line in Figure 3.2; we emphasize this sum because it better represents the domain size transition from nanodomains (uniform GUVs) to visible domains. For convenience in the following discussion, we define ρ^* as the composition at which half

of GUVs have visible domains. Below, we show that ρ^* is correlated with line tension. As shown in Figure 3.2, the size transition marked by ρ^* depended upon both the highTm and the lowTm lipids. For example, in mixtures of DOPC/POPC/chol with the highTm lipids pSM, eSM, DSPC, or bSM, ρ^* appeared at 0, 0.07, 0.24, and 0.52, respectively (Figure 3.2 *A, C, F, and I*). The nature of the lowTm nanodomain-forming PC also affected ρ^* : For mixtures of bSM/DOPC/chol with the fourth components 16:0,18:2-PC, POPC (16:0-18:1PC), or SOPC (18:0-18:1), ρ^* appeared at 0.45, 0.52, and 0.58, respectively (Figure 3.2 *H, I and J*). Thus, increased unsaturation and shorter acyl chains of the lowTm nanodomain-forming lipid shifted ρ^* to lower values in these mixtures, consistent with a previous report that a thinner Ld phase results in a greater hydrophobic mismatch and possibly a higher line tension (11) inducing the formation of visible domains at lower ρ . Also consistent with thickness mismatch-driven line tension is the observation that lowTm macrodomain-forming PCs with different hydrophobic thickness resulted in different ρ^* values: in mixtures with DSPC/DLPC/chol (Figure 3.2 *D and G*) and DSPC/POPC/chol (Figure 3.2 *E and F*), a smaller amount of DPhPC (hydrophobic thickness 27.2 Å at 30 °C, (53)) compared to DOPC (hydrophobic thickness 29.1 Å at 30 °C, (54)) was needed to form macroscopic domains. Finally, contrary to theoretical predictions that hybrid and non-hybrid lipids should behave differently (55), DLPC and POPC resulted in a nearly identical ρ window (13, 56) in mixtures with DSPC/DOPC/chol (Figure 3.2 *F and G*).

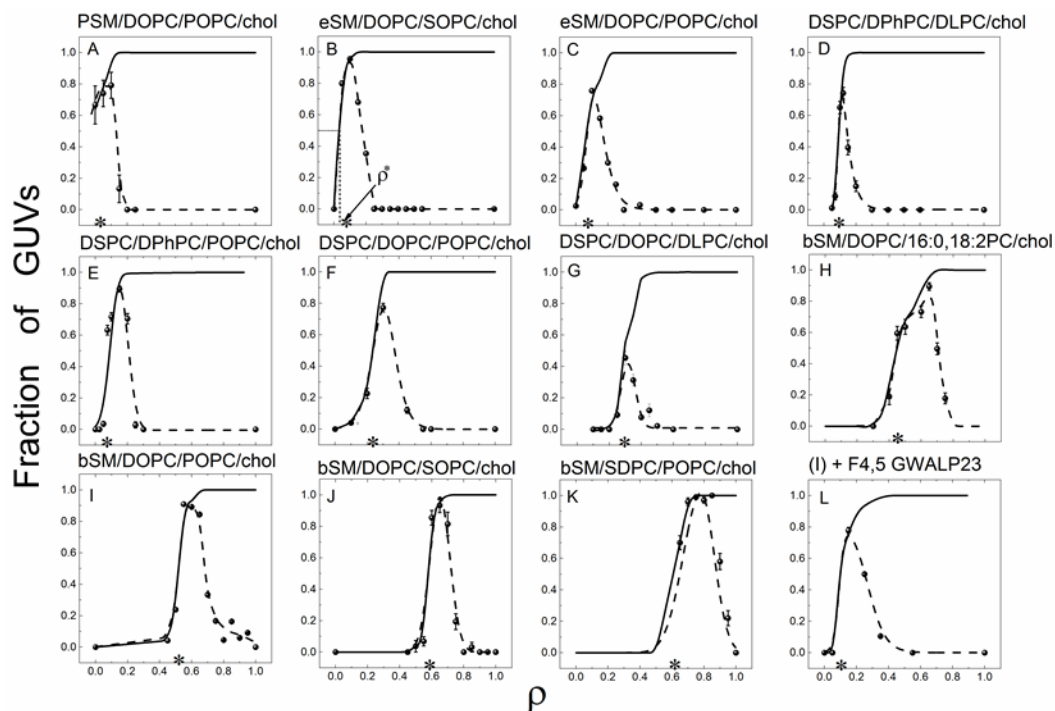


FIGURE 3.2. Morphology of coexisting Ld + Lo domains changes with ρ . In GUVs prepared from four-component lipid mixtures, phase domain morphology changes from uniform (i.e., no visible domains), to modulated patterns, to macroscopic round domains as ρ is varied from 0 to 1. The fraction of GUVs showing modulated domain morphology is plotted as a function of ρ for different four-component lipid mixtures (dashed lines). The solid line is the fraction of GUVs showing modulated phases + the fraction of GUVs showing macroscopic domains. The asterisk marks the mid-point of the domain size transition, denoted as ρ^* . Data for panels F, G and K originally appeared in Refs (56), (13) and (57), respectively.

We also examined mixtures with compositions that are closer to that of the PM. In bSM/SDPC/POPC/chol (57), we found a high ρ^* value of 0.61 (Figure 3.2 K), an indication of enhanced stability of nanoscopic domains. In contrast, a mixture containing an α -helical transmembrane peptide appears to have a markedly increased line tension. Figure 3.2 I and L show the ρ trajectory for bSM/DOPC/POPC/chol in the

absence and presence of 4 mol% of F⁴⁻⁵GWALP23, respectively, revealing a decrease in ρ^* from 0.52 to 0.1 induced by the peptide.

We used GUV flicker spectroscopy to measure line tension for six mixtures, shown in Figure 3.3. Comparing these data to the ρ -windows in Figure 3.2, several trends are apparent: (a) for each of the mixtures, the ρ value where micron-scale domains first appeared corresponds to a line tension of ~ 0.3 pN; (b) large, round domains always correspond to line tensions $> \sim 1.1$ pN; (c) line tension values for highTm sphingomyelins followed the trend pSM $>$ eSM $>$ bSM in mixtures with DOPC/POPC/chol, consistent with a progressively higher ρ -window for SM in this series, with $\rho^* = 0.1, 0.15$ and 0.55 , respectively (Figure 3.2 A, C and I); (d) with the highTm lipid DSPC, similar line tensions and ρ^* values were found in mixtures with DPhPC/DLPC/chol and with DPhPC/POPC/chol, whereas lower line tension and a higher ρ^* were found with DOPC/POPC/chol. We conclude that changes in ρ^* for these lipid mixtures reflect changes in the Ld/Lo line tension.

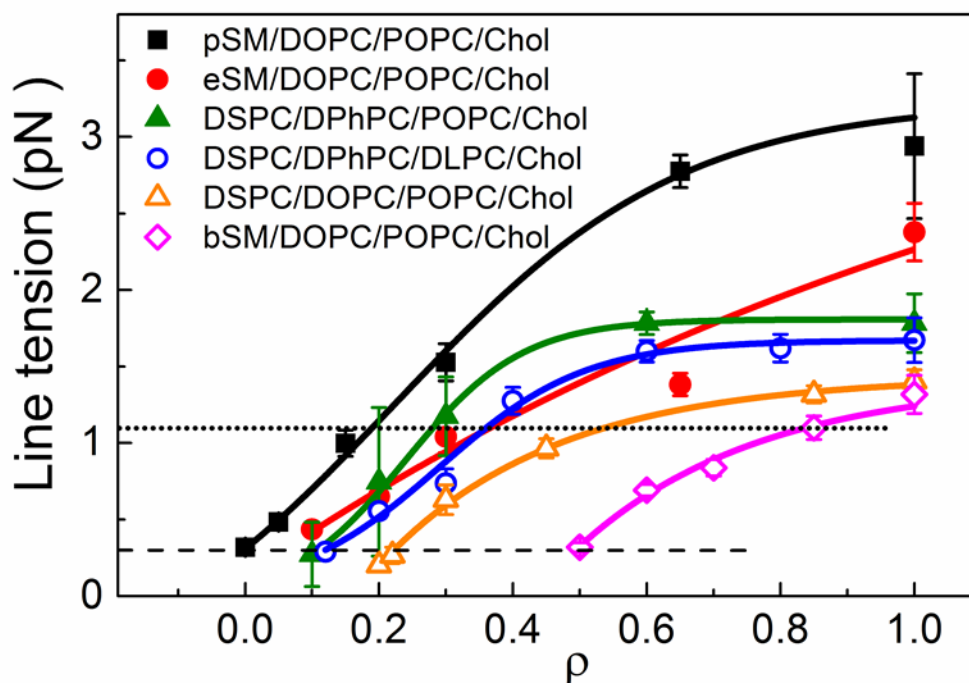


FIGURE 3.3. Line tension increases in a ρ trajectory. Line tension for six four-component lipid mixtures measured with GUV flicker spectroscopy. In all mixtures, visible domains first appear at ~ 0.3 pN (dashed line), while domains become fully rounded at ~ 1.1 pN (dotted line). Line tension was measured by fluctuation analysis of either an Lo or Ld domain using widefield fluorescence microscopy at 23°C with fluorescent dye C12:0-DiI at 0.2 mol %. Error bars correspond to standard error.

3.4.2 Physical and chemical properties of Ld and Lo phases do not change at the abrupt domain size transition

We measured a phase property of the bilayer, the bending modulus κ , for single phase GUVs. These measurements were performed separately for Ld and Lo compositions from the nanoscopic to the macroscopic regime ($\rho = 0$ to 1), including the region where an abrupt domain size transition occurs. Figure 3.4 shows the bending moduli of the Ld and Lo phases, κ_{Ld} and κ_{Lo} , for DSPC/DOPC/POPC/chol. As ρ was

varied from 0 to 1, κ_{Ld} decreased from 1.9 to 1.1×10^{-19} J, while κ_{Lo} increased from 7.3 to 10.4×10^{-19} J. For both the Ld and Lo phases, variation in bending moduli over the entire ρ trajectory was less than two-fold, and only 5-10% within the region of abrupt domain size change indicated by the shaded regions (corresponding to the ρ -window of Figure 3.2 F).

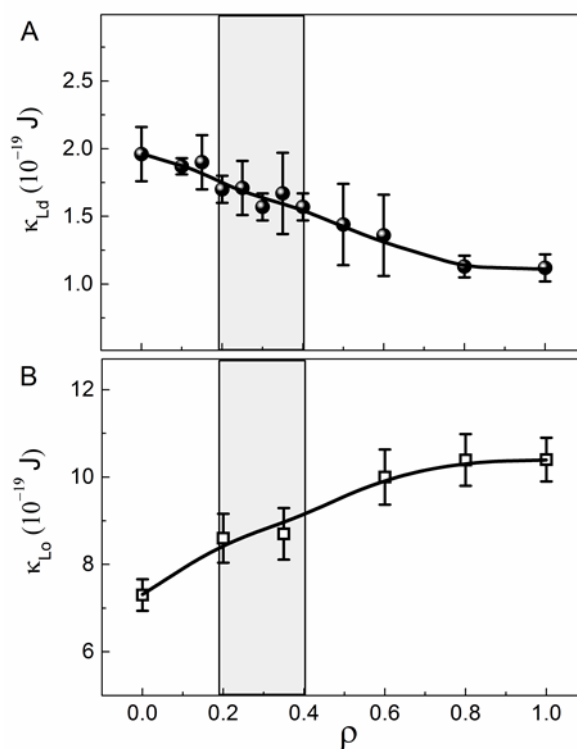


FIGURE 3.4. Lo and Ld bending moduli do not show abrupt transitions in a ρ trajectory. The bending modulus of (A) Ld phase (κ_{Ld}) and (B) Lo phase (κ_{Lo}) measured at different ρ values in DSPC/DOPC/POPC/chol. As POPC is replaced by DOPC (i.e., increasing ρ), κ_{Ld} gradually decreases, while κ_{Lo} gradually increases. Within the ρ -window where domain size exhibits an abrupt increase (shaded region), changes in bending rigidity of either phase are $< 10\%$. Error bars correspond to standard error ($n > 5$).

We also measured the partition coefficient K_p between Ld + Lo domains of a fluorescent probe, Bodipy-PC, and an ESR probe, 16PC, in the composition range $\rho = 0$ to 1. Here, $K_p = [\text{probe}]^{\text{Ld}} / [\text{probe}]^{\text{Lo}}$ and $K_p > 1$ indicates preference for Ld phase. Figure 3.5 A shows the K_p of Bodipy-PC in bSM/DOPC/POPC/chol obtained either from fluorescence microscopy measurements of GUVs (open triangles) or from fluorescence spectroscopic measurements (solid circles), revealing good agreement between these methods. K_p of Bodipy-PC increases from 3 to 9 over the composition range $\rho = 0$ to 1, and by $\sim 30\%$ in the vicinity of the abrupt domain size transition indicated by the shaded region (corresponding to the ρ -window of Figure 3.2 J). For the ESR probe 16PC, K_p values in DSPC/DOPC/POPC/chol increase from 0.7 to 1.8 over the composition range $\rho = 0$ to 1 (Figure 3.5 B). There are no abrupt changes in K_p , and in particular less than a 10% change in the shaded region corresponding to the ρ -window of Figure 3.2 F, where domain size changes hundreds of fold. Moreover, the order parameter S_0 and rotational diffusion coefficient R_{\perp} of 16PC in the Ld and Lo phases hardly changed: Table 3.1 shows nearly constant values of S_0 and R_{\perp} for $\rho = 0, 0.3$ and 1, representative of nanoscopic, transition, and macroscopic compositions. We conclude that physical and chemical properties of Ld and Lo phases do not undergo abrupt changes despite the abrupt change in domain size that occurs along a ρ trajectory.

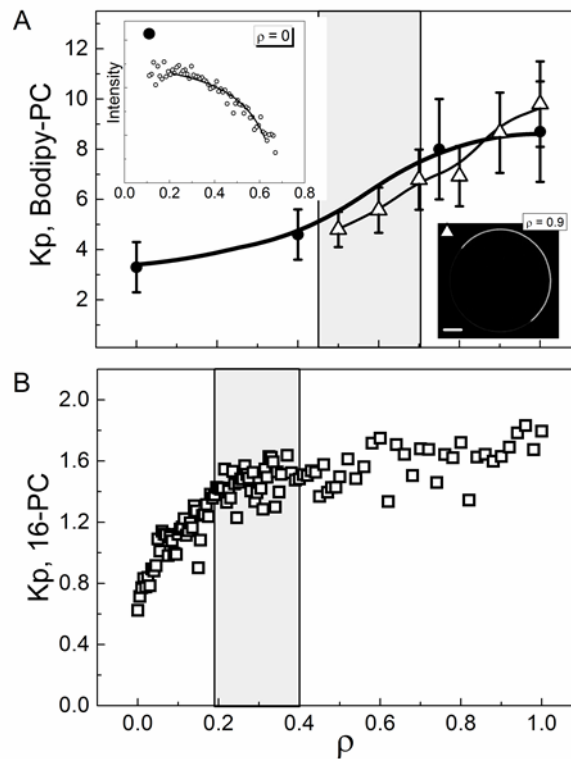


FIGURE 3.5. Probe partition coefficients do not show abrupt transitions along a ρ trajectory. Partition coefficient K_p between Ld and Lo phases for: (A) the fluorescence probe Bodipy-PC in bSM/DOPC/POPC/chol, and (B) the spin-label probe 16PC in DSPC/DOPC/POPC/chol. Within the ρ window where domain size exhibits an abrupt increase (shaded regions), changes in K_p are gradual. Also shown in panel (A) are: (upper left inset) the fluorescence intensity (symbols) and fit to a partitioning model (solid line) of BoDIPY-PC along a thermodynamic tieline at $\rho = 0$, and (lower right inset) fluorescence microgram revealing the partitioning of BoDIPY-PC in a GUV at $\rho = 0.9$ (scale bar 5 μm , temperature 23°C). For details, see Appendix B.

TABLE 3.1. ESR reveals small changes of Ld and Lo phases along the domain size transition. Order parameter, S_0 , and rotational diffusion coefficient, R_λ , of the spin probe 16PC in Ld and Lo phases for different ρ values that represent nanoscopic, transition, and macroscopic lipid compositions.

ρ	Ld phase		Lo phase	
	S_0	R_λ ($\log_{10} \text{s}^{-1}$)	S_0	R_λ ($\log_{10} \text{s}^{-1}$)
0	0.13	8.4	0.36	8.6
0.3	0.12	8.5	0.36	8.6
1.0	0.11	8.5	0.34	8.5

3.4.3 Competing interactions could drive the domain size transition

With no evidence of an abrupt transition in several properties characteristic of Ld and Lo phases, we next explored what kind of interaction could lead to an abrupt transition in domain size. We modeled the dependence of domain size on line tension together with dipole-dipole repulsion that could originate, for example, in the permanent dipoles of the carbonyl-glycerol backbone (Figure B.14). Figure 3.6 A shows the energies of the individual competing interactions (i.e., boundary energy arising from line tension and electrostatic energy arising from dipole-dipole repulsion) as a function of domain radius, calculated for a line tension of 0.25 pN. Figure 3.6 B reveals that the total energy is minimized *at a particular domain size*, which we define as the equilibrium domain radius R_d^* . Figure 3.6 C shows R_d^* as a function of line tension. At very low line tensions, electrostatic repulsion dominates and numerous small domains are favored. At high line tensions, the boundary energy dominates and a single, large

domain is favored. These two competing interactions are balanced at intermediate line tensions, resulting in stable domains with nanoscopic sizes. The precise location of the transition is influenced by the choice of model parameters: for example, increasing the Ld/Lo electrostatic potential difference $\Delta\phi$ from 0.1 V (solid line) to 0.2 V (dot-dashed line) increases domain repulsion, thereby stabilizing nanodomains to higher line tension values.

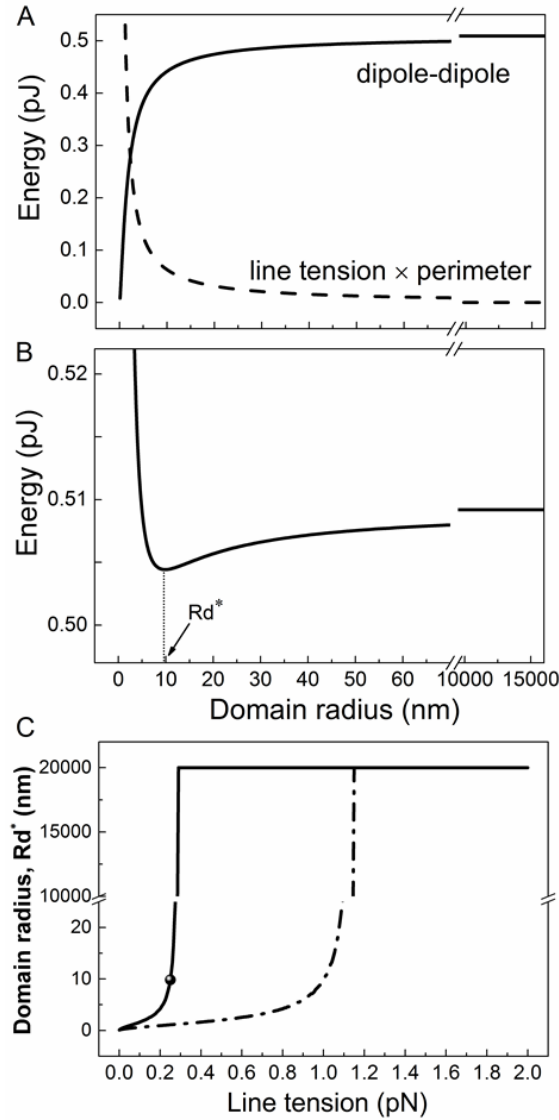


FIGURE 3.6. A model of competing interactions describes the domain size transition. (A) Energetic contributions from domain interface (line tension \times perimeter) and dipole-dipole repulsion as a function of domain radius, calculated for a line tension value of 0.25 pN. (B) The sum of interfacial and electrostatic energy in (A) exhibits a minimum value at domain radius R_d^* . (C) R_d^* plotted vs. line tension reveals an abrupt domain size transition for model parameters $\varepsilon = 8$, $h = 3.0$ nm, $A_L = 60 \text{ \AA}^2$, and $\Delta\phi = 0.1$ V (solid line) or 0.2 V (dot-dashed line). A description of model parameters is found in Appendix B.

We further examined several model parameters to find the line tension value where the domain size transition occurs (Figures B.15 *B* and B.16). The critical line tension value λ^* at which domain size abruptly increases depends strongly on the dipole potential difference: we found that varying $\Delta\phi$ over the range 0.05–0.5 V resulted in λ^* values increasing from 0.08–8 pN. Large changes were also observed upon varying the dielectric constant ε over the range 2–20, which resulted in λ^* increasing from 0.05–0.8 pN. In contrast, varying the separation distance of the dipole layers h , or the area per dipole A_L , had negligible influence on the critical line tension value. Although the precise line tension value at the domain size transition depends on the choice of model parameters, the finding of an abrupt transition is robust. It occurs for a wide range of parameter values, as well as in related models where the domain potential is treated as arising from discrete dipoles, or from pairs of discrete charges, or where the electrostatics of both the domain and the surrounding in a spherical phase-separated vesicle are treated separately. These results are presented in Appendix B.

3.4.4 Nanoscopic domains are not significantly influenced by vesicle size, but have a complex shape

In the nanoscopic regime, GUVs appear uniform (e.g. Figure 3.1 *C*, $\rho = 0$ and 0.1), thus different experimental methods are required to study the coexistence of Ld + Lo domains. We used SANS to measure domain size in 50 and 100 nm diameter LUVs composed of DSPC/DOPC/POPC/chol, finding only a small influence of vesicle size

on nanodomain size as a function of ρ (Figure 3.7). Additional details about the minimal dependence of nanodomain size on LUV size are found in the Appendix B.

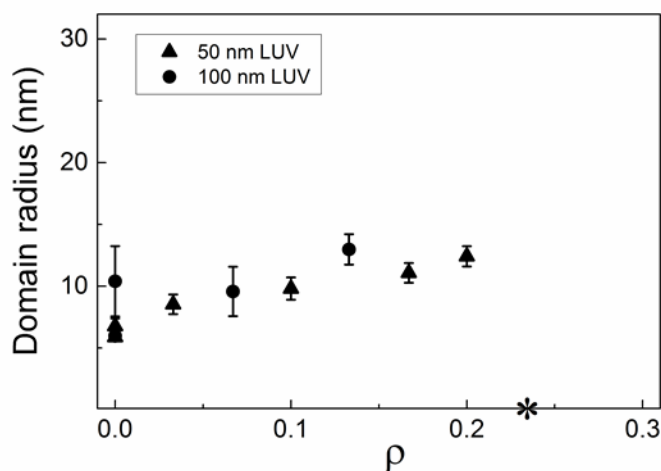


FIGURE 3.7. SANS reveals domain size in the nanoscopic regime along ρ . Domain radius obtained from Monte Carlo modeling of SANS data for LUVs composed of DSPC/DOPC/POPC/chol. Within the nanoscopic regime at $\rho < 0.2$, domain radius increases gradually from 6 to 12 nm for LUVs of either 50 nm diameter (triangles) or 100 nm diameter (circles). The asterisk marks ρ^* , where 50% of the GUVs were observed with modulated phases or with macrodomains.

Our SANS model assumes round nanodomains to facilitate analysis. However, coarse grained MD simulations revealed a more complex domain morphology. Figure 3.8 shows a characteristic simulation snapshot of a nanodomain for $\rho = 0.65$ after 3.6 μ s of simulation, together with a circular outline diameter of approximately 25 nm as a reference. These simulations show that nanodomains are in general not circular. Rather,

they display complex and dynamic morphology, even in an equilibrated system long after separation into coexisting Ld + Lo domains.

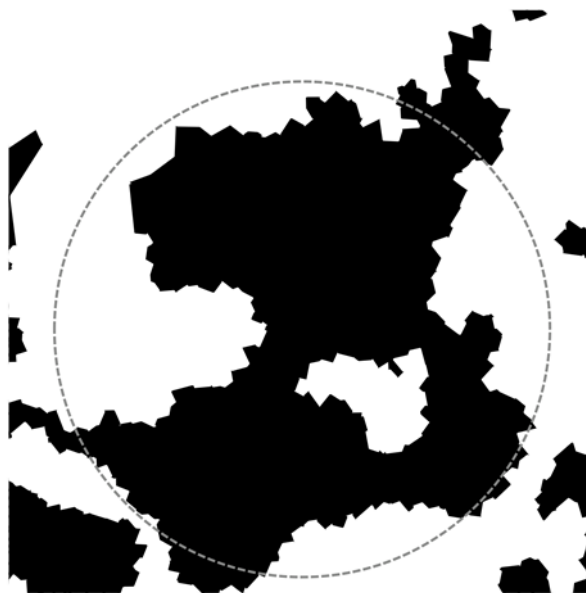


FIGURE 3.8. Simulated nanodomains have a complex morphology. A top-down view of a nanodomain in a coarse-grained MD simulation of DPPC/DUPC/PUPC/chol at $\rho = 0.65$ reveals a complex, non-circular domain shape. Voronoi cells of lipids in the Lo phase are shown in black, while those in the Ld phase are shown in white. The snapshot was obtained after $3.6 \mu\text{s}$ of simulation at a temperature of 22°C . A gray circle of 25 nm diameter is shown as a reference.

3.5 Discussion

As we show in this work, the energy per unit length of the interface (i.e., the line tension) in a phase-separated bilayer can be dramatically influenced by lipid composition, thereby driving changes in interface length and thus domain size. Cells

could control the size of coexisting domains in the PM and thereby modulate signaling simply by changing the high T_m or the low T_m lipids, or any other factors that change line tension. We used four-component mixtures in order to control the transition of coexisting Ld + Lo domains from nanoscopic to macroscopic sizes (10). The high T_m lipids we examined were pSM, bSM, eSM and DSPC, chosen for biological prevalence or because of extensive prior characterization. The low T_m lipids were POPC, DOPC, DLPC, SDPC and DPhPC, chosen either for biological prevalence or because these lipids create macroscopic Ld + Lo domains.

3.5.1 The domain size transition is correlated with line tension

As ρ is increased, Ld and Lo domains in each of the mixtures in Figure 3.2 undergo a change in size of two orders of magnitude at ρ^* , from tens of nanometers in diameter to the visible micron scale. This size increase occurs over a change of only ~ 2–5% in the total lipid composition, which corresponds to ~ 20% variation in ρ . This width of the ρ -window also has a component from the compositional variation of individual GUVs that has been estimated to be ± 5 mol% (58), so the true size change could be even more abrupt.

For the mixtures shown in Figure 3.3, the line tension value where macroscopic domains first appear is in every case ~ 0.3 pN. It is possible that an interaction that competes with line tension, e.g. dipole-dipole repulsion, is overwhelmed by a line tension of 0.3 pN. The domain size just below this ρ value might provide information

on the dipole magnitude and dielectric constant in that region of the bilayer. Another possibility is that below 0.3 pN, thermal fluctuations break up domains.

Comparing Figures 3.2 and 3.3, ρ^* occurs at a line tension of ~ 1.1 pN for each mixture. We previously modeled the domain size transition as arising from a competition between line tension and curvature (17) and found that this model could reproduce experimental observations including modulated phase patterns (10, 13). Bending energy opposes line tension by penalizing large domains of the stiffer Lo phase on curved surfaces, and macroscopic patterns occur when the two interactions are more balanced. Modulated morphology might give way to rounded macroscopic domains at roughly the same value of line tension perhaps because the rigidity difference between Ld and Lo is similar for the mixtures studied here.

Another simple relationship emerges from a comparison of Figures 3.2 and 3.3, namely that smaller values of ρ^* in every case correspond to higher values of the line tension. A higher ρ^* can therefore be a useful surrogate for lower line tension: compared to the conditions needed to determine line tension, a 10-fold lower dye concentration and ~ 10 -fold lower cumulative light exposure are needed to determine ρ^* , resulting in a much lower probability of photochemical artifacts (22). Using ρ^* data we can therefore more readily investigate mixtures containing unstable polyunsaturated lipids. For example, photochemical instability of the 22:6 acyl chain of SDPC precludes measuring line tension, yet phase boundaries (57) as well as ρ^* could be determined for the mixture, bSM/SDPC/POPC/chol, Figure 3.2 K. The strikingly high value of $\rho^* = 0.61$ indicates quite low line tension until the mixture has a high fraction of SDPC. In a

sense, line tension is just barely enough for bSM/SDPC/chol phase domains to be macroscopic. Another interesting case is bSM/DOPC/POPC/chol with a significant fraction of transmembrane helical peptide as a component. Upon adding the α -helical peptide GWALP23 to the otherwise lipid-only mixtures, ρ^* drops from $\rho = 0.52$ to 0.1 for bSM/DOPC/POPC/chol (Figure 2 *I* and *L*), and from $\rho = 0.58$ to 0.3 for bSM/DOPC/SOPC/chol (unpublished data, S. Wickramasinghe). These observations reveal that this peptide significantly increases the line tension. In a previous MD simulation we found that GWALP23 is depleted from the Ld/Lo interface, consistent with the peptide increasing line tension (59).

3.5.2 Properties of Ld and Lo domains do not change abruptly despite the abrupt domain size transition

We studied different properties of Ld and Lo phases along the domain size transition from nanoscopic to macroscopic phase separation. Well-resolved phase diagrams were required for this work. A previously determined four-component phase diagram enabled finding phase boundaries for each ρ value in the representative mixture DSPC/DOPC/POPC/chol (9). Although our compositional trajectories were always within the Ld + Lo coexistence region, the tieline endpoints change with ρ . Accurate phase boundaries are needed to apply the Lever-Arm Rule in order to study Lo and Ld properties such as bending modulus, order parameter, rotational diffusion and probe partition between these phases. Defining ρ^* for each mixture enabled our finding that the abrupt increase in domain size is not accompanied by abrupt changes in any measured Ld and Lo phase properties. A potentially important corollary is that because

no abrupt changes with domain size are observed in the particular properties we chose to measure here, we suggest that measurement of these properties in the macroscopic regime is likely to reflect the properties of the nanoscopic domains. In general, it is more convenient to measure macroscopic domain properties, which we here establish as providing useful information about nanoscopic domain properties.

We measured the bending modulus for both Ld and Lo phases over the entire range of ρ values. In the compositional range where domain size changes dramatically (the shaded regions in Figure 3.4), the bending moduli change by just a few percent. The Ld bending modulus decreases with increasing ρ (i.e., increasing DOPC, Figure 3.4 A), consistent with observations that single-component membranes of lowTm lipids with one saturated chain, like POPC, are rigidified by cholesterol while DOPC membranes are not (25, 26, 60, 61). The DSPC/DOPC/POPC/chol phase diagram (9) indicates that the Ld composition does not depend on ρ , having a similar concentration of DSPC, lowTm lipid, and chol at all ρ values. In contrast, the Lo composition contains proportionally more DSPC and chol, and less lowTm lipid, as ρ increases. Consequently, the Lo phase bending modulus increases with increasing ρ (Figure 3.4 B).

Another phase-dependent property characteristic of coexisting Ld + Lo domains is the partition coefficient K_p for a molecule that can equilibrate between the two environments. We measured K_p for the mixtures DSPC/DOPC/POPC/chol (Figure 3.5 B) and bSM/DOPC/POPC/chol (Figure 3.5 A). For both a paramagnetic ESR probe (16PC) and a fluorescent probe (Bodipy-PC), we observed compositional dependence

as ρ was varied from 0 to 1, with K_p increasing by ~ 3 -fold over the entire range of ρ , but without abrupt changes at the composition ρ^* where domain size changes abruptly in both lipid mixtures. Another finding emerges from the single dye fluorescence experiments performed in the nanoscopic regime: simple, hyperbolic partitioning curves are observed in both the nanodomain region (left inset of Figure 3.5 A) and the macrodomain region (raw data not shown). We conclude that Ld and Lo phase fractions in the nanoscopic regime follow the Lever-Arm Rule just like macroscopic phase separation.

Using ESR, we also examined the order parameter and rotational diffusion rate of 16PC in Ld and Lo phases of DSPC/DOPC/POPC/chol. Changes in these parameters were surprisingly small (Table 3.1), consistent with only gradual variation in phase properties.

3.5.3 Competition between line tension and dipole repulsion drives the domain size transition

What is responsible for the abrupt increase in domain size observed for 12 different mixtures? A simple model of line tension competing with dipole repulsion reproduces the abrupt domain size transition observed in experiments (Figure 3.6). The model relies on the dipoles in each leaflet being far enough apart as not to cancel, having a significant component oriented along the bilayer normal, and being located in a low enough dielectric that the field persists for several lipid neighbors. We do not know the dielectric constant in part because we do not know the actual dipole location. We also

do not know the difference in dipole density between Lo and Ld domains, since that would require measurements of the Lo phase that are not yet reliable. Still, reasonable ranges of these parameters all show an abrupt domain size transition (Figures B.15 and B.16).

We do not know which dipoles might be involved in limiting domain size. We chose to model repulsion that would be consistent with carbonyl groups, in part because experiments with ether-linked chains show a decrease in bilayer potential (62), although such experiments do not rule out the very real possibility that ester- vs. ether-induced conformational changes could influence a measured dipole potential. Also, the carbonyl-carbonyl distances across the bilayer are relatively well-defined and thus suitable to model. An oriented bound water molecule could be a source of dipole-dipole repulsion, if located in a low dielectric region such that the electric field would persist over several lipid neighbors. In these symmetric bilayers, dipoles of the terminal methyls could not be the source of the repulsion as they are in lipid monolayers, because the apposing leaflet methyl dipoles would be so close and of the same type of phase (and thus the same motional and orientational state) as to cancel. However, we do not rule out that in asymmetric bilayers the terminal methyls could contribute to dipole-dipole repulsion. Additionally, the methyl dipoles might contribute significant electrostatic repulsion for nanodomains that are not in register across the leaflets (63). In brief, we have not proven that our treatment of dipole-dipole repulsion correctly describes the interaction that occurs on the tens of nanometer scale to compete with line tension. We have only shown that with reasonable values of key parameters, the difference of dipole potential between Ld and Lo domains and the dielectric constant

near those dipoles, the observed behavior is reproduced in our model: domain size abruptly changes by two orders of magnitude with a small change in line tension.

It could be that for line tension $< \sim 0.3$ pN the amplitudes of thermal fluctuations are sufficient for preventing the coalescence of domains. This could occur, for example, if the fluctuations approached the size of the domains themselves. For example, at $\rho = 0$ domain diameter measured by SANS is ~ 15 nm (Figure 3.7). Fluctuations of this magnitude would occur with a line tension of approximately 0.1 pN (24). However, this consideration does not address the dramatic size change observed experimentally. In this regard, MD simulations have shown that registration of domains together with domain size both dramatically increase at a domain size of ~ 15 nm (38). These findings point to enhanced coupling of the two leaflets and domain stability both enabled at a particular domain size. Because these are observations from MD simulations, which would include implicitly any dipole-dipole effects, we are not able to separate these effects in the simulations.

3.5.4 Hybrid and non-hybrid lipids have similar line activity

We have previously concluded that emphasis on a special behavior of hybrid lipids in forming nanodomains is misleading (56). For five of the six mixtures shown in Figure 3 we used POPC as the nanodomain-forming lowT_m lipid. Starting at $\rho = 1$ where line tension is greatest, the ρ trajectory could be described as substituting a fraction of POPC into the high line tension mixture. In four of the mixtures, POPC hardly lowers line tension until it becomes nearly 40 mol% of the lowT_m lipid. When

the nanodomain-forming lowT_m lipid is DLPC instead of POPC, the same result is observed. These experiments suggest that hybrid lipid POPC behaves similarly to the non-hybrid lipid DLPC to decrease line tension. Both POPC and DLPC might be described as weakly line active.

3.5.5 Nanodomains have a complex morphology

The large MD simulations performed in this study better reveal nanodomain size and morphology. Compared to previous studies (38) our large box size of 74×74 nm allowed for multiple independent L_o nanodomains to exist in the L_d surround in a leaflet of coexisting L_d + L_o phases. We find nanodomain size to be consistent with SANS measurements, on the order of 25 nm. In a 3.6 μ s simulation at $\rho = 0.65$ (see Appendix B simulation snapshots at other ρ values), following the first microsecond of equilibration, nanodomains are easily recognized, but their morphology is highly dynamic throughout the simulation, and it is never circular.

3.6 Summary and Conclusions

We investigated the nature of the abrupt domain size transition observed in four-component lipid mixtures mimicking the PM composition. We find that various L_d and L_o phase properties measured as functions of ρ can be explained by treating L_d + L_o nanodomains as coexisting phase domains, and that the domain size transition does not appear to be a phase transition. However, the more important point is the phenomenon itself, namely that coexisting nanoscopic domains containing hundreds to thousands of

lipids coalesce over a narrow composition range into domains hundreds of times larger. We find that line tension is the key parameter that controls this size transition, and line tension depends strongly on the nature of both the high T_m and low T_m lipids. In summary:

1. The size of coexisting Ld + Lo domains changes abruptly in composition space.
2. Line tension has the decisive role in controlling the abrupt size transition.
3. Ld or Lo phase parameters show only gradual changes even as domain size changes abruptly.
4. Phase behaviors measured for Ld + Lo macrodomains are a good surrogate for behaviors of nanodomains.
5. Hybrid lipids 18:0,22:6-PC, 16:0,18:1-PC, 16:0,18:2-PC, or 18:0,18:1-PC reduce line tension only weakly.
6. Visible Ld + Lo phase domains first appear at line tension ~ 0.3 pN in 6 different lipid mixtures.
7. Dipole repulsion within the bilayer might stabilize nanodomains.
8. MD simulations of a large patch of lipids show that a nanodomain is not round, but has complex and fluctuating morphology.

3.7 Author contributions

Figure 1 A. Previous data included for illustration; B. Image created by TAE; C.

Images acquired by WCT

Figure 2 A-L ρ windows defined by SPW, WCT, MBK, and previous works

Figure 3 Method implementation/development by RDU, analysis implementation/development by DGA, and line tension measurements by SPW, WCT, and MBK.

Figure 4 Membrane bending rigidity measurements by RDU

Figure 5 A. K_p measurements made by TAE; B. K_p measurements by SW

Table 1 ESR data from SW

Figure 6 Dipole repulsion model from DGA and FAH

Figure 7 SANS data from FAH

Figure 8 Molecular dynamics simulation image from MDW

3.8 References

1. Quehenberger, O., A.M. Armando, A.H. Brown, S.B. Milne, D.S. Myers, A.H. Merrill, S. Bandyopadhyay, K.N. Jones, S. Kelly, R.L. Shaner, C.M. Sullards, E. Wang, R.C. Murphy, R.M. Barkley, T.J. Leiker, C.R.H. Raetz, Z. Guan, G.M. Laird, D.A. Six, D.W. Russell, J.G. McDonald, S. Subramaniam, E. Fahy, and E.A. Dennis. 2010. Lipidomics reveals a remarkable diversity of lipids in human plasma. *J. Lipid Res.* 51: 3299–305.
2. Sampaio, J.L., M.J. Gerl, C. Klose, C.S. Ejsing, H. Beug, K. Simons, and A. Shevchenko. 2011. Membrane lipidome of an epithelial cell line. *Proc. Natl. Acad. Sci.* 108: 1903–1907.
3. Takamori, S., M. Holt, K. Stenius, E.A. Lemke, M. Grønberg, D. Riedel, H. Urlaub, S. Schenck, B. Brügger, P. Ringler, S.A. Müller, B. Rammner, F. Gräter, J.S. Hub, B.L. De Groot, G. Mieskes, Y. Moriyama, J. Klingauf, H. Grubmüller, J. Heuser, F. Wieland, and R. Jahn. 2006. Molecular anatomy of a trafficking organelle. *Cell.* 127: 831–46.
4. Lomize, M.A., A.L. Lomize, I.D. Pogozheva, and H.I. Mosberg. 2006. OPM: orientations of proteins in membranes database. *Bioinformatics.* 22: 623–5.
5. Lin, Q., and E. London. 2015. Ordered Raft Domains Induced by Outer Leaflet Sphingomyelin in Cholesterol-Rich Asymmetric Vesicles. *Biophys. J.* 108: 2212–2222.
6. Feigenson, G.W., and J.T. Buboltz. 2001. Ternary phase diagram of dipalmitoyl-PC/dilauroyl-PC/cholesterol: nanoscopic domain formation driven by cholesterol. *Biophys. J.* 80: 2775–88.
7. Zhao, J., J. Wu, F. a Heberle, T.T. Mills, P. Klawitter, G. Huang, G. Costanza, and G.W. Feigenson. 2007. Phase studies of model biomembranes: complex behavior of DSPC/DOPC/cholesterol. *Biochim. Biophys. Acta.* 1768: 2764–76.
8. Heberle, F.A., J. Wu, S.L. Goh, R.S. Petruzielo, and G.W. Feigenson. 2010. Comparison of three ternary lipid bilayer mixtures: FRET and ESR reveal nanodomains. *Biophys. J.* 99: 3309–18.
9. Konyakhina, T.M., J. Wu, J.D. Mastroianni, F.A. Heberle, and G.W. Feigenson. 2013. Phase diagram of a 4-component lipid mixture: DSPC/DOPC/POPC/chol. *Biochim. Biophys. Acta.* 1828: 2204–14.
10. Konyakhina, T.M., S.L. Goh, J. Amazon, F.A. Heberle, J. Wu, and G.W. Feigenson. 2011. Control of a nanoscopic-to-macroscopic transition: modulated phases in four-component DSPC/DOPC/POPC/Chol giant unilamellar vesicles. *Biophys. J.* 101: L8-10.
11. Heberle, F.A., R.S. Petruzielo, J. Pan, P. Drazba, N. Kučerka, R.F. Standaert, G.W. Feigenson, and J. Katsaras. 2013. Bilayer thickness mismatch controls domain size in model membranes. *J. Am. Chem. Soc.* 135: 6853–9.

12. de Wit, G., J.S.H. Danial, P. Kukura, and M.I. Wallace. 2015. Dynamic label-free imaging of lipid nanodomains. *Proc. Natl. Acad. Sci. U. S. A.* 112: 12299–303.
13. Goh, S.L., J.J. Amazon, and G.W. Feigenson. 2013. Toward a better raft model: Modulated phases in the four-component bilayer, DSPC/DOPC/POPC/CHOL. *Biophys. J.* 104: 853–862.
14. Goh, S.L., J.J. Amazon, and G.W. Feigenson. 2013. Toward a better raft model: modulated phases in the four-component bilayer, DSPC/DOPC/POPC/CHOL. *Biophys. J.* 104: 853–62.
15. Lee, D.W., Y. Min, P. Dhar, A. Ramachandran, J.N. Israelachvili, and J.A. Zasadzinski. 2011. Relating domain size distribution to line tension and molecular dipole density in model cytoplasmic myelin lipid monolayers. *Proc. Natl. Acad. Sci. U. S. A.* 108: 9425–9430.
16. García-Sáez, A.J., S. Chiantia, and P. Schwille. 2007. Effect of line tension on the lateral organization of lipid membranes. *J. Biol. Chem.* 282: 33537–33544.
17. Amazon, J.J., S.L. Goh, and G.W. Feigenson. 2013. Competition between line tension and curvature stabilizes modulated phase patterns on the surface of giant unilamellar vesicles: a simulation study. *Phys. Rev. E. Stat. Nonlin. Soft Matter Phys.* 87: 22708.
18. Kingsley, P. B., Feigenson, G.W. 1979. The Synthesis of a Perdeuterated Phospholipid: 1,2-dimyristoyl-sn-glycero-3-phosphocholine-d72. *Chem. Phys. Lipids.* 24: 135–147.
19. Gleason, N.J., V. V Vostrikov, D. V Greathouse, C. V Grant, S.J. Opella, and R.E. Koeppe. 2012. Tyrosine replacing tryptophan as an anchor in GWALP peptides. *Biochemistry.* 51: 2044–53.
20. Angelova, M., S. Soleau, and P. Méléard. 1992. Preparation of giant vesicles by external AC electric fields. Kinetics and applications. *Trends Colloid and interface Science VI* 89: 127–131.
21. Baumgart, T., G. Hunt, E.R. Farkas, W.W. Webb, and G.W. Feigenson. 2007. Fluorescence probe partitioning between Lo/Ld phases in lipid membranes. *Biochim. Biophys. Acta.* 1768: 2182–2194.
22. Morales-Pennington, N.F., J. Wu, E.R. Farkas, S.L. Goh, T.M. Konyakhina, J.Y. Zheng, W.W. Webb, and G.W. Feigenson. 2010. GUV preparation and imaging: minimizing artifacts. *Biochim. Biophys. Acta.* 1798: 1324–32.
23. Petruzielo, R.S., F.A. Heberle, P. Drazba, J. Katsaras, and G.W. Feigenson. 2013. Phase behavior and domain size in sphingomyelin-containing lipid bilayers. *Biochim. Biophys. Acta.* 1828: 1302–13.
24. Esposito, C., A. Tian, S. Melamed, C. Johnson, S.-Y. Tee, and T. Baumgart.

2007. Flicker spectroscopy of thermal lipid bilayer domain boundary fluctuations. *Biophys. J.* 93: 3169–3181.
25. Pécéréaux, J., H.G. Döbereiner, J. Prost, J.F. Joanny, and P. Bassereau. 2004. Refined contour analysis of giant unilamellar vesicles. *Eur. Phys. J. E.* 13: 277–290.
 26. Gracià, R.S., N. Bezlyepkina, R.L. Knorr, R. Lipowsky, and R. Dimova. 2010. Effect of cholesterol on the rigidity of saturated and unsaturated membranes: fluctuation and electrodeformation analysis of giant vesicles. *Soft Matter.* 6: 1472.
 27. Budil, D.E., S. Lee, S. Saxena, and J.H. Freed. 1996. Nonlinear-Least-Squares Analysis of Slow-Motion EPR Spectra in One and Two Dimensions Using a Modified Levenberg–Marquardt Algorithm. *J. Magn. Reson. Ser. A.* 120: 155–189.
 28. Ge, M., and J.H. Freed. 1999. Electron-Spin Resonance Study of Aggregation of Gramicidin in Dipalmitoylphosphatidylcholine Bilayers and Hydrophobic Mismatch. *Biophys. J.* 76: 264–280.
 29. Dzikovski, B., and J. Freed. 2013. Membrane Fluidity. In: Roberts GCK, editor. *Encyc Biophys.* Berlin, Germany: Springer Verlag. pp. 1440–1446.
 30. Buboltz, J.T., and G.W. Feigenson. 1999. A novel strategy for the preparation of liposomes: rapid solvent exchange. *Biochim. Biophys. Acta* 1417: 232–245.
 31. Amazon, J.J., and G.W. Feigenson. 2014. Lattice simulations of phase morphology on lipid bilayers: Renormalization, membrane shape, and electrostatic dipole interactions. *Phys. Rev. E - Stat. Nonlinear, Soft Matter Phys.* 89: 1–11.
 32. McConnell, H.M. 1991. Structures and Transitions in Lipid Monolayers at the Air-Water Interface. *Annu. Rev. Phys. Chem.* 42: 171–195.
 33. Distances In Bounded Regions.
<http://www.mathpages.com/home/kmath324/kmath324.htm>.
 34. Zhou, F., and K. Schulten. 1995. Molecular Dynamics Study of a Membrane-Water Interface. *J. Phys. Chem.* 99: 2194–2207.
 35. Kučerka, N., J. Pencser, J.N. Sachs, J.F. Nagle, and J. Katsaras. 2007. Curvature Effect on the Structure of Phospholipid Bilayers. *Langmuir.* 23: 1292–1299.
 36. Arnold, O., J.C. Bilheux, J.M. Borreguero, A. Buts, S.I. Campbell, L. Chapon, M. Doucet, N. Draper, R. Ferraz Leal, M.A. Gigg, V.E. Lynch, A. Markvardsen, D.J. Mikkelsen, R.L. Mikkelsen, R. Miller, K. Palmén, P. Parker, G. Passos, T.G. Perring, P.F. Peterson, S. Ren, M.A. Reuter, A.T. Savici, J.W. Taylor, R.J. Taylor, R. Tolchenov, W. Zhou, and J. Zikovsky. 2014. Mantid—Data analysis and visualization package for neutron scattering and μ SR

- experiments. *Nucl. Instruments Methods Phys. Res. Sect. A Accel. Spectrometers, Detect. Assoc. Equip.* 764: 156–166.
37. Pan, J., F.A. Heberle, R.S. Petruzielo, and J. Katsaras. 2013. Using small-angle neutron scattering to detect nanoscopic lipid domains. *Chem. Phys. Lipids.* 170: 19–32.
 38. Ackerman, D.G., and G.W. Feigenson. 2015. Multiscale modeling of four-component lipid mixtures: Domain composition, size, alignment, and properties of the phase interface. *J. Phys. Chem. B.* 119.
 39. Qi, Y., H.I. Ingólfsson, X. Cheng, J. Lee, S.J. Marrink, and W. Im. 2015. CHARMM-GUI Martini Maker for Coarse-Grained Simulations with the Martini Force Field. *J. Chem. Theory Comput.* 11: 4486–4494.
 40. Lee, J., X. Cheng, J.M. Swails, M.S. Yeom, P.K. Eastman, J.A. Lemkul, S. Wei, J. Buckner, J.C. Jeong, Y. Qi, S. Jo, V.S. Pande, D.A. Case, C.L. Brooks, A.D. MacKerell, J.B. Klauda, and W. Im. 2016. CHARMM-GUI Input Generator for NAMD, GROMACS, AMBER, OpenMM, and CHARMM/OpenMM Simulations Using the CHARMM36 Additive Force Field. *J. Chem. Theory Comput.* 12: 405–413.
 41. Brooks, B.R., C.L. Brooks, A.D. Mackerell, L. Nilsson, R.J. Petrella, B. Roux, Y. Won, G. Archontis, C. Bartels, S. Boresch, A. Caflisch, L. Caves, Q. Cui, A.R. Dinner, M. Feig, S. Fischer, J. Gao, M. Hodoscek, W. Im, K. Kuczera, T. Lazaridis, J. Ma, V. Ovchinnikov, E. Paci, R.W. Pastor, C.B. Post, J.Z. Pu, M. Schaefer, B. Tidor, R.M. Venable, H.L. Woodcock, X. Wu, W. Yang, D.M. York, and M. Karplus. 2009. CHARMM: The biomolecular simulation program. *J. Comput. Chem.* 30: 1545–1614.
 42. Jo, S., T. Kim, V.G. Iyer, and W. Im. 2008. CHARMM-GUI: A web-based graphical user interface for CHARMM. *J. Comput. Chem.* 29: 1859–1865.
 43. Hess, B., C. Kutzner, D. van der Spoel, and E. Lindahl. 2008. GROMACS 4: Algorithms for Highly Efficient, Load-Balanced, and Scalable Molecular Simulation. *J. Chem. Theory Comput.* 4(3): 435–447.
 44. Siewert J. Marrink, H. Jelger Risselada, Serge Yefimov, and D. Peter Tieleman, and A.H. de Vries. 2007. The MARTINI Force Field: Coarse Grained Model for Biomolecular Simulations. *J. Phys. Chem. B.* 111 (27): 7812–7824.
 45. Monticelli, L., S.K. Kandasamy, X. Periole, R.G. Larson, D.P. Tieleman, and S.-J. Marrink. 2008. The MARTINI Coarse-Grained Force Field: Extension to Proteins. *J. Chem. Theory Comput.* 4: 819–834.
 46. Melo, M.N., H.I. Ingólfsson, and S.J. Marrink. 2015. Parameters for Martini sterols and hopanoids based on a virtual-site description. *J. Chem. Phys.* 143: 243152.
 47. McGibbon, R.T., K.A. Beauchamp, M.P. Harrigan, C. Klein, J.M. Swails, C.X.

- Hernández, C.R. Schwantes, L.-P. Wang, T.J. Lane, and V.S. Pande. 2015. MDTraj: A Modern Open Library for the Analysis of Molecular Dynamics Trajectories. *Biophys. J.* 109: 1528–1532.
48. Marsh, D. 2009. Cholesterol-induced fluid membrane domains: A compendium of lipid-raft ternary phase diagrams. *Biochim. Biophys. Acta.* 1788: 2114–2123.
 49. Feigenson, G.W. 2009. Phase diagrams and lipid domains in multicomponent lipid bilayer mixtures. *Biochim. Biophys. Acta.* 1788: 47–52.
 50. Kreuzberger, M.A., E. Tejada, Y. Wang, and P.F. Almeida. 2015. GUVs Melt Like LUVs: The Large Heat Capacity of MLVs Is Not Due to Large Size or Small Curvature. *Biophys. J.* 108(11): 2619–2622.
 51. Veatch, S.L., K. Gawrisch, and S.L. Keller. 2006. Closed-loop miscibility gap and quantitative tie-lines in ternary membranes containing diphytanoyl PC. *Biophys. J.* 90: 4428–36.
 52. Uppamoochikkal, P., S. Tristram-Nagle, and J.F. Nagle. 2010. Orientation of tie-lines in the phase diagram of DOPC/DPPC/cholesterol model biomembranes. *Langmuir.* 26: 17363–8.
 53. Kučerka, N., M.-P. Nieh, and J. Katsaras. 2011. Fluid phase lipid areas and bilayer thicknesses of commonly used phosphatidylcholines as a function of temperature. *Biochim. Biophys. Acta.* 1808: 2761–2771.
 54. Kučerka, N., J. Gallová, D. Uhríková, P. Balgavý, M. Bulacu, S.-J. Marrink, and J. Katsaras. 2009. Areas of Monounsaturated Diacylphosphatidylcholines. *Biophys. J.* 97: 1926–1932.
 55. Palmieri, B., and S.A. Safran. 2013. Hybrid Lipids Increase the Probability of Fluctuating Nanodomains in Mixed Membranes. *Langmuir.* 29: 5246–5261.
 56. Heberle, F.A., M. Doktorova, S.L. Goh, R.F. Standaert, J. Katsaras, and G.W. Feigenson. 2013. Hybrid and nonhybrid lipids exert common effects on membrane raft size and morphology. *J. Am. Chem. Soc.* 135.
 57. Konyakhina, T.M., and G.W. Feigenson. 2016. Phase diagram of a polyunsaturated lipid mixture: Brain sphingomyelin/1-stearoyl-2-docosahexaenoyl-sn-glycero-3-phosphocholine/cholesterol. *Biochim. Biophys. Acta.* 1858: 153–161.
 58. Baykal-Caglar, E., E. Hassan-Zadeh, B. Saremi, and J. Huang. 2012. Preparation of giant unilamellar vesicles from damp lipid film for better lipid compositional uniformity. *Biochim. Biophys. Acta.* 1818: 2598–2604.
 59. Ackerman, D.G., and G.W. Feigenson. 2016. Effects of Transmembrane α -Helix Length and Concentration on Phase Behavior in Four-Component Lipid Mixtures: A Molecular Dynamics Study. *J. Phys. Chem. B.* 120: 4064–4077.
 60. Pan, J., T.T. Mills, S. Tristram-Nagle, and J.F. Nagle. 2008. Cholesterol

Perturbs Lipid Bilayers Nonuniversally. *Phys. Rev. Lett.* 100: 198103.

61. Marsh, D. 2006. Elastic curvature constants of lipid monolayers and bilayers. *Chem. Phys. Lipids.* 144: 146–59.
62. Gawrisch, K., D. Ruston, J. Zimmerberg, V.A. Parsegian, R.P. Rand, and N. Fuller. 1992. Membrane dipole potentials, hydration forces, and the ordering of water at membrane surfaces. *Biophys. J.* 61: 1213–23.
63. Travesset, A. 2006. Effect of dipolar moments in domain sizes of lipid bilayers and monolayers. *J. Chem. Phys.* 125: 84905.

Chapter 4

Calculation of liquid-disordered/liquid-ordered line tension from pairwise lipid interactions*

4.1 Abstract

The energy penalty for membrane phase domain interfaces, line tension, is an important quantity in describing domain size and dynamics. In this work, we sought to connect the compositional differences between coexisting liquid-disordered (Ld) and liquid-ordered (Lo) phases known from phase diagrams with experimentally measured line tensions. We determined pairwise lipid interaction energies for various ternary mixtures by using the compositional differences between coexisting Ld and Lo phases. We find that experimentally measured Ld/Lo line tension can be explained by the sum of pairwise interactions at the interface including a small Gibbs (line) excess, or compositional adjustment to minimize unfavorable contacts.

*R.D. Usery, S. Hiraki, G.W. Feigenson. 2018. Calculation of liquid-disordered/liquid-ordered line tension from pairwise lipid interactions. *Biophysical Journal* (submitted)

4.2 Introduction

The lipid raft hypothesis describes how the plasma membrane could organize its many protein and lipid components in order to carry out the many necessary functions for life (1). The size and dynamics of “rafts” in the plasma membrane could strongly impact membrane trafficking, the cytoskeleton, signal transduction and viral assembly (2–5). Line tension, the energy penalty for interface, describes the propensity for membrane domains to coalesce, always favoring larger domains. A change in line tension via local composition change for example drives changes in interface length and thus, domain size. Changes in raft size would have many implications for plasma membrane function by altering the capacity of membrane domains to accommodate proteins that must interact for signaling.

Model membranes with coexisting liquid disordered (Ld) and liquid ordered (Lo) phases provide a chemically simplified and compositionally well-defined model of raft+non-raft behavior in the plasma membrane (6). Coexistence of Ld and Lo minimally requires a high melting temperature (highT_m) lipid, a low melting temperature (lowT_m) lipid, and cholesterol (chol) (6, 7). Well-resolved phase diagrams can be constructed for model systems, allowing the phase boundaries, phase fractions, and tielines to be utilized in understanding membrane behavior.

Phase behavior for various highT_m/lowT_m/chol mixtures has been mapped (8–12). The boundaries of the two-phase region reflect the partitioning between coexisting phases of each component as illustrated in Figure 4.1. Within the Ld + Lo coexistence region, the light grey compositions coexist with the dark grey

compositions. The pair of coexisting Ld and Lo compositions that is known directly from FRET data used in phase boundary determinations is that of A and B at the lowest tieline of the two-phase region, Figure 4.1 (9, 10, 12).

These ternary mixtures can exhibit domains that are microns in diameter, termed macroscopic phase separation, or domains that are nanometers in diameter, termed nanoscopic phase separation. Whereas macroscopic phase separation can be readily observed with optical microscopy, nanoscopic domains are detected by other means such as SANS and FRET (9, 10, 12–14). Model systems have proven useful in investigations relating to line tension by incrementally progressing from a nanoscopic mixture to a macroscopic mixture. In this way, composition can tune domain size (13, 15–17).

In stark contrast to the long history of studies of the 2-dimensional analogue, surface tension, the origins of line tension are not well examined. A primary theoretical model (18) for line tension is based on thickness mismatch and resulting physical deformation at the interface. Due to the packing of lipid chains in the bilayer, the lipids in the “raft-like” Lo phase are more extended and thus the Lo phase is thicker than the Ld phase. Though mismatch is correlated with line tension, rigorous experimental support for the mismatch model is limited by uncertain parameter values. Moreover, the known unfavorable contact of chemically distinct phases is explicitly not addressed by this kind of mechanical model.

Here we explore the origin of line tension using the wealth of thermodynamic information contained in equilibrium compositional phase diagrams. We investigate

the idea that compositional differences of coexisting phases could be sufficient to account for the unfavorable energy where Ld and Lo phases are in contact. Using a straightforward model, we determined the pairwise interaction energies between components in ternary systems from phase boundaries and tielines. We then calculated the total of the pairwise interaction energies along the interface of Ld and Lo, resulting in the chemical contribution to line tension in terms of the pairwise interaction energies. Our calculations enabled determination of the lipid interaction energies from tieline endpoints for six lipid mixtures. For these mixtures at various levels of cholesterol, we calculated the line tension based on the differences in Ld and Lo compositions and interaction energies. We then compared these values to our experimental measurements of line tension obtained with flicker spectroscopy. We found that the pairwise lipid interaction energies are more than sufficient to account for the line tension.

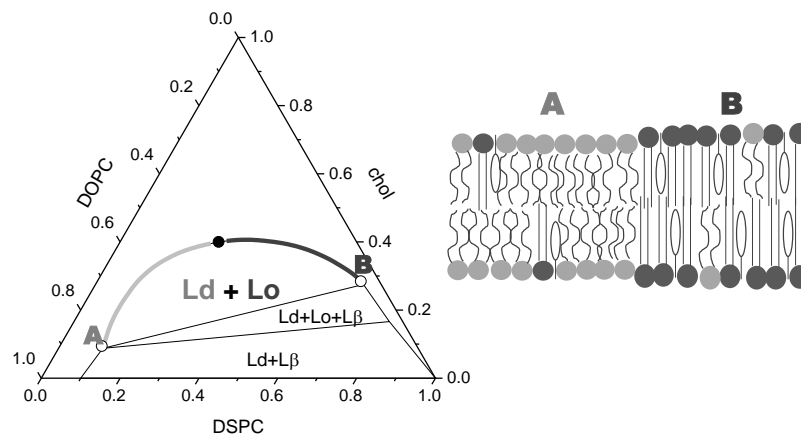


Figure 4.1 Phase diagram of DSPC/DOPC/chol. Boundaries of the Ld+Lo two-phase region are shown in bold. Light grey depicts Ld compositions that coexist with Lo compositions (dark grey) on the opposite phase boundary. The critical point is the solid point as determined in (10). Compositions that coexist along the lowest tieline of the two-phase region, open points, are labelled for Ld (A) and Lo (B). Adjacent to the phase diagram is an illustration of the interface schematically showing the compositions of coexisting Ld and Lo.

4.3 Materials and Methods

4.3.1 Materials

Lipids used in this study are as follows: 1,2-distearoyl-sn-glycero-3-phosphocholine (DSPC), brain sphingomyelin (bSM), or n-palmitoyl-D-erythro-sphingosylphosphorylcholine (PSM), 1,2-dioleoyl-sn-glycero-3-phosphocholine

(DOPC) or 1-palmitoyl-2-oleoyl-sn-glycero-3-phosphocholine (POPC), and chol. Phospholipids were purchased from Avanti Polar Lipids (Alabaster, AL). Purity of phospholipids was found to be better than 99.5% using thin layer chromatography. Briefly, ~20 μg of lipid was spotted on washed and activated Adsorbosil thin-layer chromatography plates (Alltech, Deerfield, IL) and developed in the solvent system chloroform/methanol/water = 65/25/4. Phospholipid concentrations were determined by inorganic phosphate assay (19), with an error < 1% from 10 replicates. Chol was from Nu-Chek Prep (Elysian, MN), and its stock solutions were made at defined concentrations using standard gravimetric procedures. The fluorescent dye 1,1'-didodecyl-3,3',3',3'-tetramethylindocarbocyanine perchlorate (C12:0 DiI) was from Invitrogen (Carlsbad, CA). Concentrations were determined by absorption spectroscopy using extinction coefficients of $143,000 \text{ M}^{-1} \text{ cm}^{-1}$. ACS grade Sucrose was from Fisher Scientific (Fair Lawn, NJ), and Ultra-Pure glucose from Teknova (Hollister, CA).

4.3.2 Model

Our model is strictly pairwise additive; multibody interactions and physical deformations at the interface are not addressed. The thermodynamic parameter needed to describe the interactions of two distinct lipid species, i and j , is the difference between the ij interaction and the average of ii and jj interactions (20–22):

$$\phi_{ij} = \varepsilon_{ij} - \frac{1}{2}(\varepsilon_{ii} + \varepsilon_{jj}) \quad (4.1)$$

where ε are the free energy interaction terms and ϕ_{ij} is the energy of changing of ii and jj pairs for an ij pair.

The sum of the energy of the pairwise interactions for a given system is

$$U = nN \sum_i X_i \varepsilon_{ii} + nN \sum_{ij} X_i X_j \phi_{ij} \quad (4.2)$$

where i, j are the components of the system, A, B, C , etc. X_i are the respective mole fractions, n is the number of nearest neighbors, N is the number of molecules in the system, and ε_{ii} and ϕ_{ij} are the interaction energies of like and non-like pairs, respectively. Modeling the bilayer as a 2D triangular lattice, n is 6. Thus average interaction energy per molecule in a ternary system with components A, B, and C can then be expressed as

$$\mathbf{U} = \frac{U}{nN} = X_A \varepsilon_{AA} + X_B \varepsilon_{BB} + X_C \varepsilon_{CC} + X_A X_B \phi_{AB} + X_B X_C \phi_{BC} + X_A X_C \phi_{AC} \quad (4.3)$$

Ld and Lo coexistence necessarily means there is an interface. To estimate line tension due to the contact of Lo and Ld phases, we consider the contacting process, Figure 4.2. With this process, one Lo/Lo and one Ld/Ld contact lines are lost and two Lo/Ld contact lines are formed in each leaflet of the bilayer. In the boundary region in which the Lo phase is in contact with the Ld phase, we assume that the composition of component i in this region $X_i^L = \bar{X}_i$ is an arithmetic mean value of those in Lo and Ld phases, and the average interaction energy per molecule in this region \mathbf{U}_L is given by $\mathbf{U}_L(X_i^L)$.

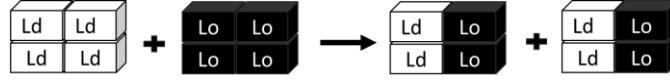


Figure 4.2. Ld/Lo bilayer contacting process. The Ld/Lo bilayer interface is formed by the loss of an Lo/Lo boundary in each leaflet and an Ld/Ld boundary in each leaflet.

There are a line of contacts on each leaflet of the bilayer. Thus, there are two sets of Ld+Lo contacts. The free energy per unit length, τ , associated with the process in Figure 4.2 for a bilayer can then be expressed in terms of pairwise interactions as

$$\tau = n'(2U_L - U_{Lo} - U_{Ld}) \quad (4.4)$$

Here n' is the number of pairs of lipids in one phase in contact with lipids in the neighboring phase at the boundary per unit boundary length. U_{Lo} , U_{Ld} , and U_L are respectively intermolecular interactions between two Lo phases, between two Ld phases, and between Lo and Ld phases. The line tension of each leaflet corresponds to $\frac{1}{2} \tau$. From equations 4.3 and 4.4, we have the following equations:

$$\tau = n' \sum_{ij} \phi_{ij} (2\bar{X}_i \bar{X}_j - X_i^{Lo} X_j^{Lo} - X_i^{Ld} X_j^{Ld}) \quad (4.5)$$

which becomes

$$\tau = -\frac{1}{2} n' \sum_{ij} \phi_{ij} (X_i^{Lo} - X_i^{Ld})(X_j^{Lo} - X_j^{Ld}) \quad (4.6)$$

As enumerated in the SM, our line tension approximation for a ternary system can be written as

$$\begin{aligned} \tau = -\frac{1}{2}n'\{ & (X_A^{Lo} - X_A^{Ld})(X_B^{Lo} - X_B^{Ld})\phi_{AB} + (X_B^{Lo} - X_B^{Ld})(X_C^{Lo} - X_C^{Ld})\phi_{BC} \\ & + (X_A^{Lo} - X_A^{Ld})(X_C^{Lo} - X_C^{Ld})\phi_{AC}\} \end{aligned} \quad (4.7)$$

In order to estimate pairwise interaction energies, we add mixing entropy (23) to equation 4.2, which yields

$$G = nN \sum_i X_i \varepsilon_{ii} + nN \sum_{ij} X_i X_j \phi_{ij} + RT \sum_i N_i \ln X_i \quad (4.8)$$

where

$$N = \sum_i N_i \quad (4.9)$$

and

$$X_i = \frac{N_i}{N} \quad (4.10)$$

The chemical potential of a component in the system can be expressed as

$$\mu_i = \left(\frac{\partial G}{\partial N_i} \right)_{T,P,N_{j \neq i}} \quad (4.11)$$

where temperature (T), pressure (P), and the number of other components ($N_{j \neq i}$) are constants.

With the substitutions of equations 4.10 and 4.11 into equation 4.8, the chemical potential of each component is determined according to equation 4.9. Considering the ternary system at chemical equilibrium, $\mu_i^{Lo} = \mu_i^{Ld}$, yields the following system of equations:

$$\begin{aligned}
RT \ln K_{p(A)} &= \{X_B^{Ld}(1 - X_A^{Ld}) - X_B^{Lo}(1 - X_A^{Lo})\}n\phi_{AB} \\
&+ \{X_C^{Ld}(1 - X_A^{Ld}) - X_C^{Lo}(1 - X_A^{Lo})\}n\phi_{AC} \\
&- \{X_B^{Ld}X_C^{Ld} - X_B^{Lo}X_C^{Lo}\}n\phi_{BC} ,
\end{aligned} \tag{4.12}$$

$$\begin{aligned}
RT \ln K_{p(B)} &= \{X_A^{Ld}(1 - X_B^{Ld}) - X_A^{Lo}(1 - X_B^{Lo})\}n\phi_{AB} \\
&+ \{X_C^{Ld}(1 - X_B^{Ld}) - X_C^{Lo}(1 - X_B^{Lo})\}n\phi_{CB} \\
&- \{X_A^{Ld}X_C^{Ld} - X_A^{Lo}X_C^{Lo}\}n\phi_{CA}
\end{aligned} \tag{4.13}$$

$$\begin{aligned}
RT \ln K_{p(C)} &= \{X_A^{Ld}(1 - X_C^{Ld}) - X_A^{Lo}(1 - X_C^{Lo})\}n\phi_{CA} \\
&+ \{X_B^{Ld}(1 - X_C^{Ld}) - X_B^{Lo}(1 - X_C^{Lo})\}n\phi_{CB} \\
&- \{X_A^{Ld}X_B^{Ld} - X_A^{Lo}X_B^{Lo}\}n\phi_{AB}
\end{aligned} \tag{4.14}$$

where

$$K_{p(i)} = X_i^{Lo} / X_i^{Ld} \tag{4.15}$$

Derivation of equations 4.12 – 4.14 is shown in greater detail in the supporting materials. An alternative expression of equations 4.12 – 4.14 is as follows:

$$k_1 = c_{11}\phi_{AB} + c_{12}\phi_{AC} + c_{13}\phi_{BC} \tag{4.16}$$

$$k_2 = c_{21}\phi_{AB} + c_{22}\phi_{AC} + c_{23}\phi_{BC} \tag{4.17}$$

$$k_3 = c_{31}\phi_{AB} + c_{32}\phi_{AC} + c_{33}\phi_{BC} \tag{4.18}$$

where k_i are the K_p terms and c_{ij} are the various concentration-dependent terms in equations 4.12 – 4.14.

Equivalently,

$$\begin{bmatrix} k_1 \\ k_2 \\ k_3 \end{bmatrix} = \begin{bmatrix} c_{11} & c_{12} & c_{13} \\ c_{21} & c_{22} & c_{23} \\ c_{31} & c_{32} & c_{33} \end{bmatrix} \begin{bmatrix} \phi_{AB} \\ \phi_{AC} \\ \phi_{BC} \end{bmatrix} \quad (4.19)$$

or

$$K = C \phi \quad (4.20)$$

Thus the interaction energies are simply

$$\phi = C^{-1}K \quad (4.21)$$

This formulation can be expanded to many tielines. The whole Ld + Lo coexistence region can thereby be utilized for the pairwise lipid interaction energy determinations.

4.3.3 GUV preparation

GUVs were prepared by electroformation (24) with modifications. Briefly, each sample contained ~300 nmol of a lipid mixture containing 0.2 mol% C12:0 DiI in 200 μ L chloroform. A lipid film was created by evenly spreading the chloroform solution on indium tin oxide-coated microscope slides (Delta Technologies, Stillwater, MN) on a hotplate with surface temperature measured at ~50°C. After residual solvent was removed under vacuum for 2 h at ~50 mTorr, indium tin oxide slides were sealed with Buna-N O-rings to create a chamber, which was then filled with 100 mM sucrose solution. Films were held above the transition temperature for 2 h in an AC field of 5 Hz, \pm 1 Vpp, using a Wavetek Meterrman FG2C Function Generator (Meterrman,

Everett, WA), followed by cooling to 23°C using a Digi-Sense Temperature Controller R/S (Cole Palmer, Vernon Hills, IL). GUVs were harvested into 100 mM glucose solution then allowed to settle for 1 h to remove debris before microscopy observations at 23°C. A wide-field microscope, Eclipse Ti (Nikon Instruments, Melville, NY) equipped with a 60×/1.2 NA water immersion objective, was used line tension measurements. An osmolality difference between the sucrose and glucose solutions of <5 mOsmol/kg H₂O was ensured with the use of an osmometer (model No. 5004; Precision Systems, Natick, MA).

GUVs were visualized at 23°C using a wide-field fluorescence microscope. Sample chambers for observation consisted of a No. 1.5 coverslip and traditional microscope slide separated with a silicone spacer (Sigma-Aldrich) of 0.25 mm thickness. Fields of view were selected with bright field illumination before fluorescent images were acquired with excitation of DiI utilizing a Spectra X Light Engine (Lumencor, Inc.) with a green LED (542/27) and a filter cube with 545/25 excitation filter and 605/70 emission filter. C12:0DiI partitions into the Ld phase (25). Images were acquired using a Zyla 5.5 sCMOS camera (Andor Technology, Belfast, UK).

4.3.4 Line tension measurements

Line tension was measured as in Usery et al. 2017 (15). Briefly, the fluctuation spectrum of a phase domain boundary on a GUV is decomposed into Fourier modes that are related to line tension by

$$\langle |u_n|^2 \rangle = \frac{2k_B T}{\sigma \pi R_0 (n^2 - 1)}, \quad (22)$$

where n is the mode number, u_n is the mode amplitude, σ is the line tension, R_0 is the radius of a circle yielding the domain area, k_B is the Boltzmann constant, and T is the absolute temperature (26). As in Usery et al. 2017 (15), σ is calculated for each mode, an average of modes $n=2-5$ was taken, and only measurements which produced relatively constant values of σ over modes $n = 2-5$ were used.

4.4 Results

The diagram in Figure 4.1 shows the two-phase region of DSPC/DOPC/chol with emphasis on the coexistence of Ld and Lo. The light grey side of the two-phase region reflects Ld compositions that coexist with the Lo compositions shown in dark grey on the opposite side. At the top of the two-phase region, there is a point where the composition of Ld and Lo is identical and the phases spontaneously interconvert. This point, the critical point, is the point in black as determined by Konyakhina et al. (10). The tieline slope in the two-phase region changes from that of the tieline connecting compositions A and B, Figure 4.1, to the slope of the line tangent to the critical point at the top of the two-phase region. The AB tieline is the best determined within the two-phase region. Critical points are known less precisely though thoroughly investigated with observations of DSPC/DOPC/chol and bSM/DOPC/chol GUVs (9, 10). In the case of these two mixtures with visible domains for which a critical point

can be more conclusively identified, this difference in slope results in lines that are nearly parallel. Comparing the tangent at the critical point to the line through the critical point parallel to the lowest tieline, the intersection of the lines with the sides of the ternary diagram differ compositionally by 1%. For our calculations, we have therefore used lines parallel to the lowest tieline to define the compositions of coexisting phases.

Ternary mixtures of the form highT_m/lowT_m/chol examined in this study are as follows: DSPC/DOPC/chol, DSPC/POPC/chol, bSM/DOPC/chol, bSM/POPC/chol, PSM/DOPC/chol, and PSM/POPC/chol. Our interaction energy calculations require accurate compositions of coexisting phases for each, which we have used phase boundaries and tielines to establish. In the determination of interaction energies, we utilized the entire two-phase regions of DSPC/DOPC/chol, DSPC/POPC/chol, bSM/DOPC/chol, and bSM/POPC/chol (9, 10). For interactions in PSM/DOPC/chol and PSM/POPC/chol, boundary compositions (27) from single trajectories were utilized, Figure C1. First, for DSPC/DOPC/chol and bSM/DOPC/chol, equally spaced lines were used to define coexisting compositions. The coexisting compositions defined by these lines begin with the endpoints A and B, Figure 4.1, and continue to compositions adjacent to the critical point. For each set of coexisting compositions, there is a corresponding set of equations solved as enumerated by equation 4.21. The interaction energies of DSPC-DOPC, DSPC-chol, DOPC-chol, bSM-DOPC, and bSM-chol were determined with a system of 180 equations produced with 30 equally-spaced tielines for both DSPC/DOPC/chol and bSM/DOPC/chol in the form of equations 4.12 – 4.14 and solved for each interaction energy as in equation 4.21.

The DPSC-POPC, bSM-POPC, and POPC-chol interaction energies were then determined with the corresponding POPC phase diagrams (9, 10). In this case, the previously determined DSPC-chol and bSM-chol interactions were needed to constrain the calculation perhaps due to the greater uncertainty regarding critical point location and smaller area resulting in effectively shorter boundary length of the DSPC/POPC/chol two-phase region. Because full, well-resolved phase diagrams are not available for PSM/DOPC/chol and PSM/POPC/chol, the POPC-chol and DOPC-chol interactions and the single set of boundary compositions (27), were then used in calculating PSM-POPC, PSM-DOPC, and PSM-chol interaction energies.

Figure 4.1 depicts schematically the domain interface and the compositions of Ld (A) and Lo (B) that would coexist at the lowest tieline of the Ld+Lo two-phase region for these lipid mixtures. This lowest tieline reflects the most different Ld and Lo phases. Accordingly, the partition coefficients of the components between phases are the most extreme there, Table 1. These values were calculated from the corresponding A and B compositions, Figure 4.1, for each mixture (9, 10, 27). As implied by identical composition at the critical point, K_{ps} all approach 1 with increasing cholesterol.

Table 4.1 Partitioning of lipids in various mixtures

<i>Mixture</i>	K_p		
	HighTm Lipid	LowTm Lipid	chol
DSPC/DOPC/chol	6.20	0.06	3.10
DSPC/POPC/chol	5.50	0.18	2.80
bSM/DOPC/chol	3.00	0.04	4.70
bSM/POPC/chol	2.90	0.10	4.00
PSM/DOPC/chol	4.27	0.03	6.80
PSM/POPC/chol	2.61	0.13	3.44

Partition coefficients from the lower boundary of the Ld+Lo two-phase region based on published phase diagrams (1,2) or single sets of boundary compositions (27).

The compositional variables used in determining pairwise interaction energies are all in the context of bilayers. As such, they include any contributions from a tendency for domains to be in register due to the coupling of the leaflets and to some extent, the contribution of mismatch. The pairwise interaction energies, calculated as described above, are shown from most to least favorable in Figure 4.3. Phospholipid interactions with cholesterol are all favorable, and interactions of HighTm and LowTm lipids are all unfavorable. The PSM-chol interaction is, by far, the most favorable at -2.48 kT. The most unfavorable interaction of the pairs we examined is that of DSPC-DOPC at +0.5 kT.

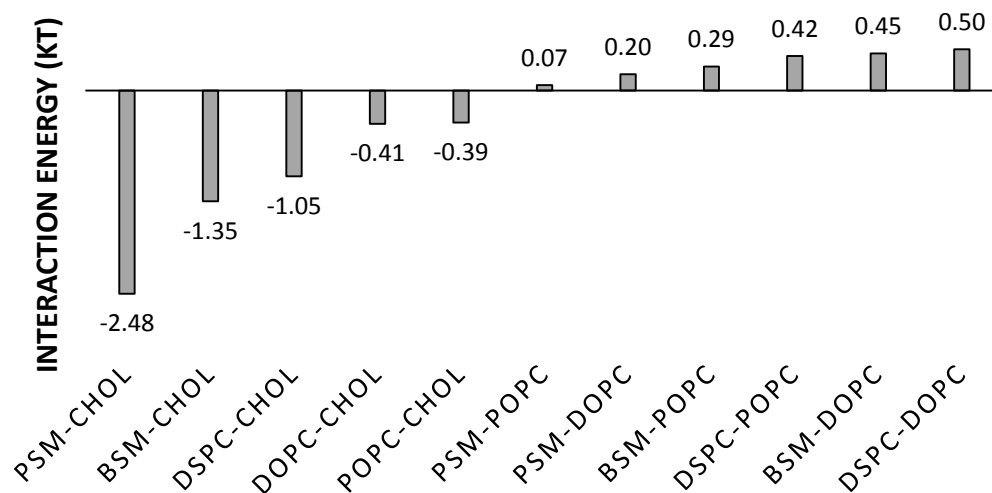


Figure 4.3 Pairwise interaction energies in the mixtures DSPC/DOPC/chol, DSPC/POPC/chol, bSM/DOPC/chol, bSM/POPC/chol, PSM/DOPC/chol, and PSM/POPC/chol. Interaction energies are shown in ascending order, from most to least favorable. Values were determined with equation 4.21 and previously determined phase diagrams (1, 2) as well as the PSM/DOPC/chol and PSM/POPC/chol compositions (27) from trajectories shown in the supporting materials.

We examined parameter sensitivity by systematically fixing each interaction energy and allowing the others to vary in the calculation, Tables S1-6. These values reflect how much each interaction energy responds to a change in the others. In each case, the HighT_m/LowT_m interaction changed the determination of the other parameters the most. The large, favorable HighT_m/chol interactions had the least impact in each case. This implies that other parameters are least sensitive to changes in that interaction.

For the ternary systems for which we determined interaction energies, we calculated values of line tension from pairwise interactions, equation 4.7. Figure 4.4 shows the comparison between calculated and experimentally measured line tensions. Line tension was measured by fluctuation spectroscopy, equation 4.22. We included line tension measurements of DSPC/DOPC/chol and bSM/DOPC/chol at various cholesterol fractions. Measurements of PSM/DOPC/chol and PSM/POPC/chol (15) at the suspected lowest tieline are also shown with the calculated line tension values obtained from one set of boundary compositions (27). The dashed line shows equivalence to aid in comparing measurements to theoretical values. This dataset covers a 10-fold range of line tension measurements from 0.3 pN to nearly 3 pN.

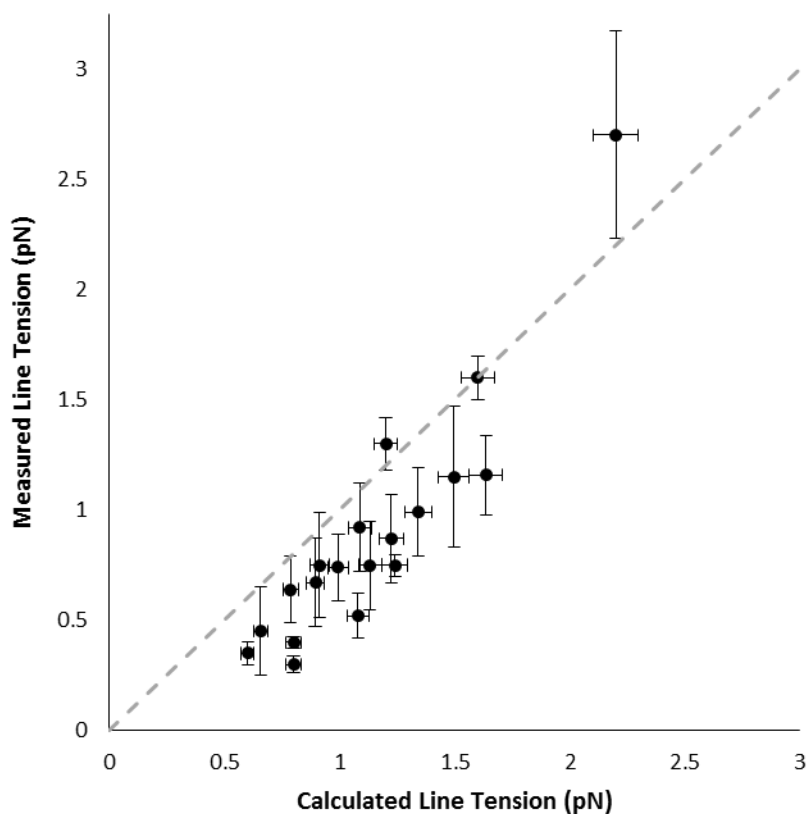


Figure 4.4 Measured and calculated values of line tension for bSM/DOPC/chol, DSPC/DOPC/chol, PSM/DOPC/chol and PSM/POPC/chol. Dashed line shows equivalence for reference.

As noted in equation 4.7, the line tension for ternary mixtures is the sum of three terms, each the product of a pairwise interaction energy and the composition. Each term's relative contribution to the theoretical line tension, defined by the term magnitude as a fraction of the total, is shown in Figure 4.5. Values are based on the lowest tieline, i.e. compositions A and B in Figure 4.1 for each mixture. However, we

observed for DSPC/DOPC/chol and bSM/DOPC/chol that the relative contributions change very little (2%) between the lowest and highest tielines for which we have measurements. The asterisks in Figure 4.5 denote mixtures with nanoscopic phase separation and thus are not represented in Figure 4.4 because line tension measurements cannot be performed on domains with sizes below optical resolution. In all cases, the LowT_m/chol term contributes the least to the line tension calculation. For the DSPC-containing mixtures, the HighT_m/LowT_m term accounts for the majority of the calculated line tension. Given the relative lack of strong interactions with cholesterol, this finding is not unexpected. For the bSM-containing mixtures, the more favorable bSM-chol interaction results in nearly equal contributions of that term and the bSM-LowT_m term. For the PSM-containing mixtures, the HighT_m/chol term is the most significant of the three due to the magnitude of the PSM-chol pairwise interaction energy.

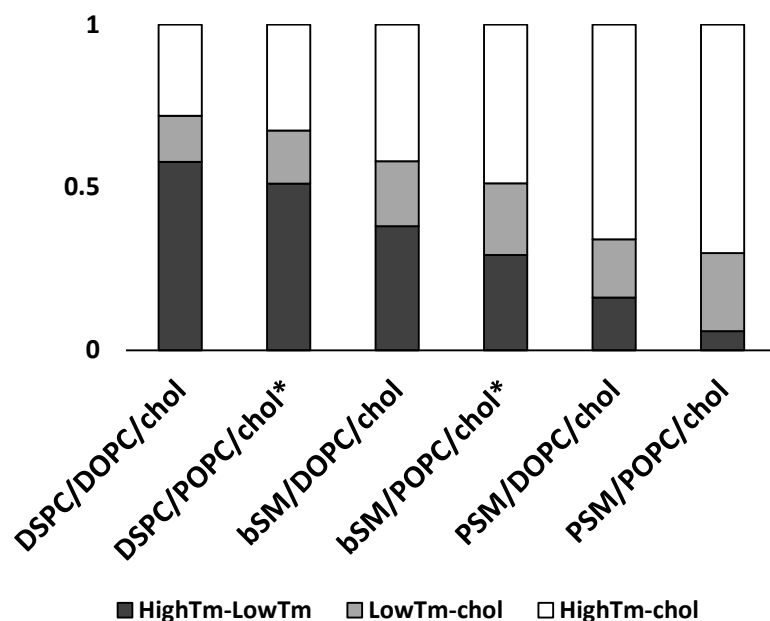


Figure 4.5 Relative contribution of terms in line tension calculations. Dark grey reflects the contribution of the HighTM/LowTm term, the contribution of the LowTm/chol term is in light grey, and the contribution HighTm/chol term is in white. The symbol, *, denotes mixtures for which domains are nanoscopic.

4.5 Discussion

Comparing the phase diagrams and interaction energies for the mixtures examined here provides unique insight into the behavior of the lipids and lipid mixtures examined in this study. For DSPC/DOPC/chol and DSPC/POPC/chol at the lower tieline of the two-phase region (the AB tieline as shown in Figure 4.1) overall Ld compositions are similar and Lo compositions strongly differ (10). Consistent with this difference in tieline length, our calculations yielded similar interaction energies with the largest difference being that of the DSPC-LowTm interactions. For

DSPC/DOPC/chol, the pairwise interaction energies presented here are similar to those produced by Monte Carlo simulation of phase boundaries (28). Compared to DSPC-containing mixtures, the compositions of bSM Ld and Lo phases are more similar as shown by the shorter lowest tieline (9). Despite the bSM interaction with cholesterol being more favorable, the bSM/DOPC+POPC/chol has lower line tension than DSPC/DOPC+POPC/chol for various ratios of DOPC to total LowTm lipid (15). For bSM, the difference between the interaction energies with DOPC and with POPC is also more pronounced due to the bSM-POPC interaction being less unfavorable. For the PSM-containing mixtures, boundaries are similar to the corresponding bSM mixtures (27). Relative to bSM/POPC/chol, PSM/POPC/chol boundaries at the longest tieline moved slightly inward, meaning tielines are shorter and the coexisting phases are more compositionally similar. For PSM/DOPC/chol, boundaries are outside those of the longest tieline of bSM/DOPC/chol, meaning Ld and Lo are less compositionally similar for PSM/DOPC/chol. These changes are consistent with the large favorable interaction of PSM with cholesterol, small unfavorable interactions with DOPC, and very small unfavorable interaction with POPC.

There is a large body of literature on the subject of lipid interaction energies, with considerable disagreement among methods (29). Utilizing entire coexistence regions in our determinations has enabled drawing useful comparisons. From Figure 4.3, it can be seen that all the phospholipid interactions with cholesterol are favorable and all HighTm-LowTm interactions are unfavorable. For the mixtures we examine, the lipids that interact most to least favorably with cholesterol are as follows: PSM > bSM > DSPC > POPC > DOPC. Due to the additional degree of unsaturation, DOPC

would be expected to interact with cholesterol less favorably than POPC, although a larger difference might have been anticipated. DSPC, a fully saturated PC, interacts more favorably with cholesterol than the other PC's as found previously, for example, by Monte Carlo simulation and cholesterol exchange rates (30, 31). All the PC molecules have less favorable interactions with cholesterol than does either PSM or bSM. SM's stronger interaction with cholesterol has been the focus of theoretical discussion regarding rafts and has been observed by a variety of means experimentally (27, 31–34). Regarding the SMs examined here, we find PSM has a much more favorable interaction with cholesterol. Perhaps chain unsaturation contributes to the bSM-chol interaction being less favorable than the PSM-chol interaction since the mixture comprising bSM contains a significant fraction of unsaturated lipids.

Regarding the HighT_m-LowT_m interactions, the HighT_m-DOPC interactions are more unfavorable than the corresponding HighT_m-POPC interactions. The difference between DOPC and POPC interactions with HighT_m lipids might have been expected to be larger on the basis of structure alone, but existing binary phase diagrams indicate similar miscibility with various highT_m lipids, supporting our findings (35). Further, we see that the PSM interactions are less unfavorable with low melting lipids than are those of DSPC and bSM interactions with LowT_m lipids. Perhaps this is due to the chain length. Chain length has been shown to strongly affect interaction with DSPC (36). For bSM, the average fatty acid chains on the sphingosine backbone is also longer than the palmitoyl chain of PSM, though how this would alter interaction energy is unknown. The small magnitude of the PSM-POPC interaction is

supported by the relatively small miscibility gap of PSM/POPC, wherein pure POPC Ld can accommodate up to 50% PSM before gel phase forms (37).

Our observations and interaction energy calculations required various tieline assumptions. For DSPC/DOPC/chol, DSPC/POPC/chol, bSM/DOPC/chol, and bSM/POPC/chol, we utilized a series of tielines parallel to the lowest tieline of the two-phase region rather than interpolating to the slope of the line tangent to the critical point, for reasons previously discussed. For the PSM mixtures, PSM/DOPC/chol and PSM/POPC/chol, the assumption of tieline slope is tenuous since it is unknown if the slope would be similar to that of bSM-containing mixtures as we have assumed here. For DSPC/POPC/chol, the two-phase region is significantly smaller and the critical point is estimated from extrapolating observed critical points in DSPC/DOPC/POPC/chol as the DOPC fraction decreases to 0 mol% (10) thereby limiting our interaction energy determinations. A small error in the interaction energy calculations arises from the compositional uncertainty of the phase diagrams. Our compositional uncertainty for each lipid is less than 1% as determined by inorganic phosphate assay. From equation 4.5, we find the error in interaction energy magnitude due to compositional uncertainty is approximately 2%.

In our examinations of parameter sensitivity, Tables S1-6, we found that in each case, the HighT_m/LowT_m interaction had the greatest impact on the determination of the other parameters. Previous work pointed to this interaction as the most crucial for Ld-Lo phase separation. (28) This observation helps to explain somewhat how DOPC and POPC interactions could differ little but give rise to such

different behavior. In this case, the HighT_m/LowT_m interaction is what differs the most between the two sets of interaction energies. The large, favorable High-T_m/chol interactions had the least impact in each case. In other words, the other parameters were least sensitive to changes in the HighT_m/chol interaction.

Our simple approach to calculating line tension assumes that interactions are pairwise additive and that the compositions at the interface are those of the bulk. We can examine the validity of these assumptions by comparing theoretical and measured values as in Figure 4.4. Most line tension values fall slightly below the dashed line in Figure 4.4, meaning that experimentally measured line tensions are lower than the theoretical values. Therefore the chemical contribution to line tension from pairwise interaction energies overestimates line tension. Points falling above the dashed line, generally being high line tension values, may indicate a greater role of local physical deformation at the interface.

In the study of surface chemistry, adsorption or desorption of a component at the phase boundary is a well-known phenomenon (38). Figure 4.4 shows most calculated values of line tension to be greater than the measured values by approximately 0.2 pN. This over prediction of line tension for most of the compositions examined may point to compositional adjustment at the interface, a Gibbs (line) excess. This means explicitly that unfavorable interactions would be reduced, and favorable interactions increased at the interface. According to Figure 4.3, this would indicate that HighT_m/LowT_m interactions are reduced. It follows that the interface would be somewhat enriched with cholesterol. Experimentally line tension

has been shown to decrease as overall cholesterol content increases and the critical point is approached (39). More cholesterol is likely at the interface as line tension decreases. Further, our findings imply that more cholesterol than indicated by the bulk compositions would be at the interface.

Prior to this work, efforts to calculate line tension have been primarily based on the physical parameters of thickness mismatch, elastic moduli, splay and tilt (18). Physical deformation at the interface is required to minimize unfavorable exposure of hydrophobic regions. However the nature and magnitude of the hydrophobic interaction is still a topic of debate, and models assume exposure of pure hydrocarbon to water. It may be more accurate to view it as exposure of the thicker phase hydrocarbon to the headgroup region of the thinner phase. Values of the physical parameters involved are not readily measured or have a high degree of uncertainty (40). Further, phase separation can be observed where there is little thickness mismatch. Coexistence of Ld and Lo occurs in the mixture DMPC/DOPC/chol at 20C, and thickness mismatch is likely minimal (13, 41). No line tension has been reported in the literature for this mixture.

Aside from being difficult to verify experimentally, there is another crucial consideration, which is explicitly ignored with the mismatch approach: the unfavorable contact of chemically distinct phases as we discuss here. Domain size does scale with thickness mismatch in the nanodomain regime of DSPC/DOPC/POPC/chol (13), but this experimental demonstration includes another consideration, the changing compositions of the phases (10). With increasing domain

size in this mixture, the amount of LowT_m lipid in the L_o phase decreases. The example of DSPC/DOPC/POPC/chol also suggests the partitioning of the various components, and thus the tieline length in the two-phase region, might include the contribution of mismatch to some extent. The DSPC/POPC/chol L_d phase coexisting with L_o near the lowest tieline of the two-phase region is thicker than the DSPC/DOPC/chol L_d phase (13). The coexisting L_o phase accommodates more POPC, making the tielines in the two-phase region shorter (10).

Hybrid lipids have been hypothesized to be enriched at the interface (42). As reported previously, the transition from domains that are nanometers in diameter to those that are microns in diameter corresponds to an increase in line tension (15) but does not require hybrid lipids (43). Our findings here imply that the line tension lowering occurs mainly via changes to the bulk phase composition. Though that doesn't rule out a slight preference of hybrid lipids for the interface, we also previously found that rather than a small, line-active fraction, 30-50 mol% POPC was required to significantly lower line tension starting from DSPC/DOPC/chol, bSM/DOPC/chol, and PSM/DOPC/chol (15). For the ternary nanoscopic mixtures, DSPC/POPC/chol and bSM/POPC/chol, the predicted line tensions at the lowest tieline of the two-phase region are 50% less than those of the macroscopic mixtures. Molecular dynamics studies indicated that nanoscopic systems may have less domain registration (44). Less registration could mean lower line tension than strictly composition would predict.

4.6 Conclusion

In this work, we determine interaction energies for 6 different ternary mixtures from compositions of coexisting Ld and Lo phases. We show how to relate pairwise lipid interaction energies and the compositional differences between coexisting Ld and Lo phases to the line tension. The comparison of our theoretical values to experimental line tension measurements indicates a Gibbs excess, or slight compositional adjustment at the Ld/Lo interface to minimize unfavorable contacts. This model does not address multibody interactions or mismatch, but despite its simplicity, the model demonstrates strong predictive power. Our work addresses a limitation in current theoretical discussion and understanding regarding the chemical contribution to line tension of membrane domains.

3.7 Author Contributions

SH initial line tension model and line tension measurements

RDU final line tension model, figures, and manuscript

4.8 References

1. Lingwood, D., and K. Simons. 2010. Lipid rafts as a membrane-organizing principle. *Science*. 327: 46–50.
2. Dinic, J., P. Ashrafzadeh, and I. Parmryd. 2013. Actin filaments attachment at the plasma membrane in live cells cause the formation of ordered lipid domains. *Biochim. Biophys. Acta - Biomembr.* 1828: 1102–1111.
3. Raghupathy, R., A.A. Anilkumar, A. Polley, P.P. Singh, M. Yadav, C. Johnson, S. Suryawanshi, V. Saikam, S.D. Sawant, A. Panda, Z. Guo, R.A. Vishwakarma, M. Rao, and S. Mayor. 2015. Transbilayer lipid interactions mediate nanoclustering of lipid-anchored proteins. *Cell*. 161: 581–94.
4. Kiessling, V., C. Wan, and L.K. Tamm. 2009. Domain coupling in asymmetric lipid bilayers. *Biochim. Biophys. Acta*. 1788: 64–71.
5. Yang, S.-T., V. Kiessling, and L.K. Tamm. 2016. Line tension at lipid phase boundaries as driving force for HIV fusion peptide-mediated fusion. *Nat. Commun.* 7: 11401.
6. Heberle, F.A., and G.W. Feigenson. 2011. Phase separation in lipid membranes. *Cold Spring Harb. Perspect. Biol.* 3: a004630-.
7. Feigenson, G.W. 2009. Phase diagrams and lipid domains in multicomponent lipid bilayer mixtures. *Biochim. Biophys. Acta - Biomembr.* 1788: 47–52.
8. Marsh, D. 2009. Cholesterol-induced fluid membrane domains: A compendium of lipid-raft ternary phase diagrams. *Biochim. Biophys. Acta - Biomembr.* 1788: 2114–2123.
9. Petruzielo, R.S., F.A. Heberle, P. Drazba, J. Katsaras, and G.W. Feigenson. 2013. Phase behavior and domain size in sphingomyelin-containing lipid bilayers. *Biochim. Biophys. Acta*. 1828: 1302–13.
10. Konyakhina, T.M., J. Wu, J.D. Mastroianni, F.A. Heberle, and G.W. Feigenson. 2013. Phase diagram of a 4-component lipid mixture: DSPC/DOPC/POPC/chol.

- Biochim. Biophys. Acta. 1828: 2204–14.
11. Zhao, J., J. Wu, F. a Heberle, T.T. Mills, P. Klawitter, G. Huang, G. Costanza, and G.W. Feigenson. 2007. Phase studies of model biomembranes: complex behavior of DSPC/DOPC/cholesterol. *Biochim. Biophys. Acta.* 1768: 2764–76.
 12. Heberle, F.A., J. Wu, S.L. Goh, R.S. Petruzielo, and G.W. Feigenson. 2010. Comparison of three ternary lipid bilayer mixtures: FRET and ESR reveal nanodomains. *Biophys. J.* 99: 3309–18.
 13. Heberle, F.A., R.S. Petruzielo, J. Pan, P. Drazba, N. Kučerka, R.F. Standaert, G.W. Feigenson, and J. Katsaras. 2013. Bilayer thickness mismatch controls domain size in model membranes. *J. Am. Chem. Soc.* 135: 6853–9.
 14. Enoki, T.A., F.A. Heberle, and G.W. Feigenson. 2018. FRET Detects the Size of Nanodomains for Coexisting Liquid-Disordered and Liquid-Ordered Phases. *Biophys. J.* 114.
 15. Usery, R.D., T.A. Enoki, S.P. Wickramasinghe, M.D. Weiner, W.-C. Tsai, M.B. Kim, S. Wang, T.L. Torng, D.G. Ackerman, F.A. Heberle, J. Katsaras, and G.W. Feigenson. 2017. Line Tension Controls Liquid-Disordered + Liquid-Ordered Domain Size Transition in Lipid Bilayers. *Biophys. J.* 112: 1431–1443.
 16. Konyakhina, T.M., S.L. Goh, J. Amazon, F.A. Heberle, J. Wu, and G.W. Feigenson. 2011. Control of a nanoscopic-to-macroscopic transition: modulated phases in four-component DSPC/DOPC/POPC/Chol giant unilamellar vesicles. *Biophys. J.* 101: L8-10.
 17. Goh, S.L., J.J. Amazon, and G.W. Feigenson. 2013. Toward a better raft model: Modulated phases in the four-component bilayer, DSPC/DOPC/POPC/CHOL. *Biophys. J.* 104: 853–862.
 18. Kuzmin, P.I., S.A. Akimov, Y.A. Chizmadzhev, J. Zimmerberg, and F.S. Cohen. 2005. Line tension and interaction energies of membrane rafts calculated from lipid splay and tilt. *Biophys. J.* 88: 1120–33.

19. Kingsley, P.B., and G.W. Feigenson. 1979. The synthesis of a perdeuterated phospholipid: 1,2-dimyristoyl-sn-glycero-3-phosphocholine-d72. *Chem. Phys. Lipids*. 24: 135–147.
20. Hill, T.L. 1986. *An introduction to statistical thermodynamics*. Dover Publications.
21. Davis, H.T. (Howard T. 1996. *Statistical mechanics of phases, interfaces, and thin films*. VCH.
22. KAKUDA, Y., E. UCHIDA, and N. IMAI. 1994. A New Model of the Excess Gibbs Energy of Mixing for a Regular Solution. *Proc. Japan Acad. Ser. B Phys. Biol. Sci.* 70: 163–168.
23. Hill, T.L. 1966. *Lectures on Matter and Equilibrium*. New York, Amsterdam: W. A. Benjamin, Inc.
24. Angelova, M.I., S. Soleau, P. Méléard, J.F. Faucon, and P. Botherel. 1992. Preparation of giant vesicles by external AC electric fields. Kinetics and applications. *Prog. Colloid Polym. Sci.* 89: 127–131.
25. Baumgart, T., G. Hunt, E.R. Farkas, W.W. Webb, and G.W. Feigenson. 2007. Fluorescence probe partitioning between Lo/Ld phases in lipid membranes. *Biochim. Biophys. Acta - Biomembr.* 1768: 2182–2194.
26. Esposito, C., A. Tian, S. Melamed, C. Johnson, S.-Y. Tee, and T. Baumgart. 2007. Flicker spectroscopy of thermal lipid bilayer domain boundary fluctuations. *Biophys. J.* 93: 3169–3181.
27. Sodt, A.J., R.W. Pastor, and E. Lyman. 2015. Hexagonal Substructure and Hydrogen Bonding in Liquid-Ordered Phases Containing Palmitoyl Sphingomyelin. *Biophys. J.* 109: 948–955.
28. Dai, J., M. Alwarawrah, M.R. Ali, G.W. Feigenson, and J. Huang. 2011. Simulation of the lo-ld phase boundary in DSPC/DOPC/cholesterol ternary mixtures using pairwise interactions. *J. Phys. Chem. B.* 115: 1662–71.

29. Almeida, P.F.F. 2009. Thermodynamics of lipid interactions in complex bilayers. *Biochim. Biophys. Acta - Biomembr.* 1788: 72–85.
30. Huang, J. 2009. Model membrane thermodynamics and lateral distribution of cholesterol: from experimental data to Monte Carlo simulation. *Methods Enzymol.* 455: 329–64.
31. Lund-Katz, S., H.M. Laboda, L.R. McLean, and M.C. Phillips. 1988. Influence of molecular packing and phospholipid type on rates of cholesterol exchange. *Biochemistry.* 27: 3416–3423.
32. Scherfeld, D., N. Kahya, and P. Schwille. 2003. Lipid Dynamics and Domain Formation in Model Membranes Composed of Ternary Mixtures of Unsaturated and Saturated Phosphatidylcholines and Cholesterol. *Biophys. J.* 85: 3758–3768.
33. Ramstedt, B., and J.P. Slotte. 2002. Membrane properties of sphingomyelins. *FEBS Lett.* 531: 33–37.
34. Demel, R.A., J.W.C.M. Jansen, P.W.M. van Dijck, and L.L.M. van Deenen. 1977. The preferential interactions of cholesterol with different classes of phospholipids. *Biochim. Biophys. Acta - Biomembr.* 465: 1–10.
35. Marsh, D. *Handbook of Lipid Bilayers.* .
36. Nibu, Y., T. Inoue, and I. Motoda. 1995. Effect of headgroup type on the miscibility of homologous phospholipids with different acyl chain lengths in hydrated bilayer. *Biophys. Chem.* 56: 273–280.
37. Ionova, I. V, V.A. Livshits, and D. Marsh. 2012. Phase diagram of ternary cholesterol/palmitoylsphingomyelin/palmitoyl-oleoyl-phosphatidylcholine mixtures: spin-label EPR study of lipid-raft formation. *Biophys. J.* 102: 1856–65.
38. Chattoraj, D.K., and K.S. Birdi. 1984. *Adsorption and the Gibbs Surface Excess.* Boston, MA: Springer US.

39. Tian, A., C. Johnson, W. Wang, and T. Baumgart. 2007. Line tension at fluid membrane domain boundaries measured by micropipette aspiration. *Phys. Rev. Lett.* 98: 208102.
40. Kollmitzer, B., P. Heftberger, M. Rappolt, and G. Pabst. 2013. Monolayer spontaneous curvature of raft-forming membrane lipids. *Soft Matter.* 9: 10877.
41. Kučerka, N., M.-P. Nieh, and J. Katsaras. 2011. Fluid phase lipid areas and bilayer thicknesses of commonly used phosphatidylcholines as a function of temperature. *Biochim. Biophys. Acta - Biomembr.* 1808: 2761–2771.
42. Palmieri, B., and S.A. Safran. 2013. Hybrid Lipids Increase the Probability of Fluctuating Nanodomains in Mixed Membranes. *Langmuir.* 29: 5246–5261.
43. Heberle, F.A., M. Doktorova, S.L. Goh, R.F. Standaert, J. Katsaras, and G.W. Feigenson. 2013. Hybrid and nonhybrid lipids exert common effects on membrane raft size and morphology. *J. Am. Chem. Soc.* 135.
44. Ackerman, D.G., and G.W. Feigenson. 2015. Multiscale modeling of four-component lipid mixtures: Domain composition, size, alignment, and properties of the phase interface. *J. Phys. Chem. B.* 119.

Appendix A

Supporting Material for Chapter 2:

Membrane bending moduli of coexisting liquid phases containing transmembrane peptide*

Contents

A.1 Bending modulus measurement – additional information

A.2 Compositions for Bending Measurements

A.3 Parameters for FRET experiments

A.4 C12:0 DiI Fluorescence Calibration

A.5 GWALP23 K_p in nanoscopic mixtures

A.6 Bending modulus measurements of DOPC + WALP23

A.7 EPR experiments

A.8 Partitioning of FAST DiO at high- and low-cholesterol

A.9 References

* Usery R, Enoki T, Wickramasinghe S, Nguyen V, Ackerman D, Greathouse D, Koeppe R, Barrera F, Feigenson G. 2018. Membrane bending moduli of coexisting liquid phases containing transmembrane peptide. *Biophysical Journal*. 114(9):2152-2164.

A.1 Bending modulus measurement- additional information

Bending modulus measurements were carried out with fluctuation analysis as in (1) implemented in Matlab version 2014b.

To ensure the harvested GUVs were slightly flaccid for fluctuation analysis, an osmolality difference between the sucrose and glucose solutions of 4 - 5 mOsmol/kg H₂O was ensured with the use of an osmometer (Model 5004, Precision Systems Inc., Natick, MA). GUVs were formed in 97 mM sucrose solution and harvested into 101 mM glucose solution. Due to the density difference and potential distortion by gravity, we limited the size of vesicles to those having radii less than 20 μm (2).

Sample chambers for observation consisted of a no. 1.5 coverslip and traditional microscope slide separated with a silicone spacer (Sigma-Aldrich, St. Louis, MO) of 0.25 mm thickness. All observations took place at room temperature of $\sim 23^\circ\text{C}$. 0.02 mol% C12:0 DiI was included in GUV preparations and fluorescence intensity was used to exclude any vesicles having more than one bilayer (3).

Datasets consisted of 1600 1 ms exposures. Contours were defined using Canny edge detection with $\sigma = 2$ in images with a pixel size of 79 nm. To ensure the contours were approximately circular the ratio of enclosed area to total perimeter is compared to the approximate radius in each frame. We excluded frames in which the contour reflected a change in radii greater than 10% compared to previous frames.

A.2 Compositions for Bending Measurements

In Figure A.1, the compositions for each of the four ternary mixtures used in this study are depicted on diagrams with their respective two-phase regions as defined by previous work (4, 5).

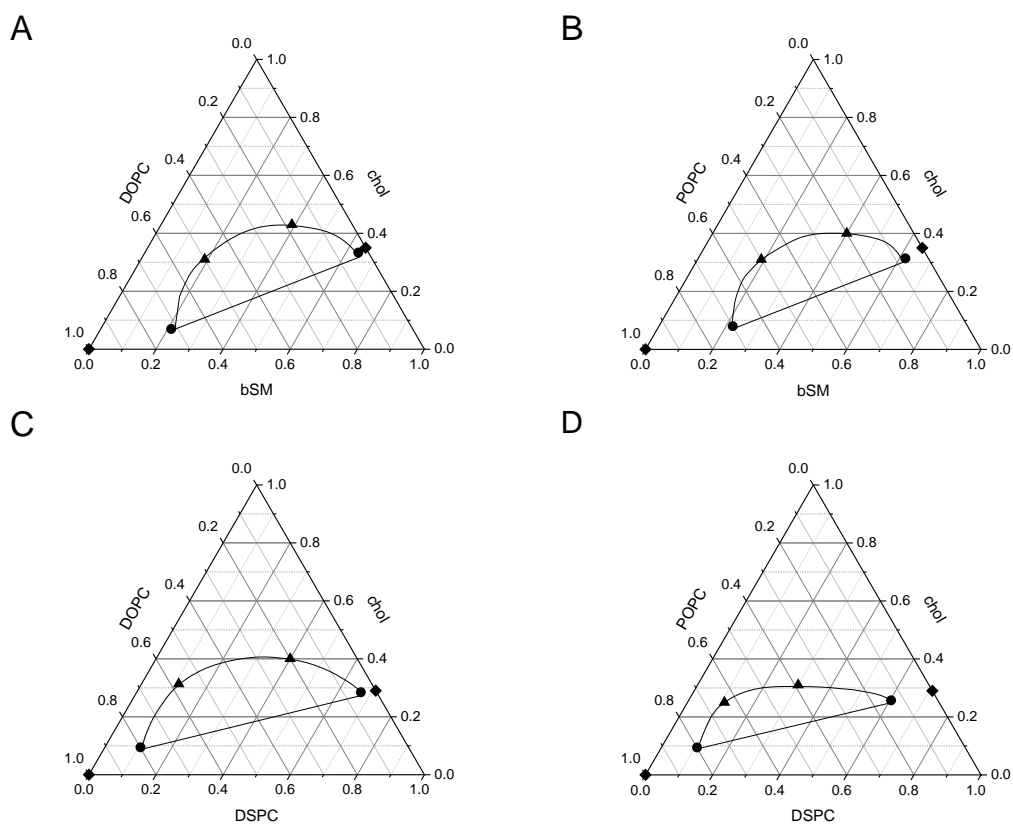


FIGURE A.1 Compositions used for bending moduli measurements. The ternary mixtures examined in this work include bSM/DOPC/chol (A), bSM/POPC/chol (B), DSPC/DOPC/chol (C), and DSPC/POPC/chol (D). For each, the simplified (◆), lower tieline endpoint (●), and high cholesterol tieline endpoint (▲) compositions are shown.

A.3 Parameters for FRET measurements

FRET along compositional trajectories was used to determine phase boundaries as previously described (6, 5, 4). Partition coefficients were also determined by these means and fitting the experimental data was done as described in the main text. In the FRET experiments, the fluorescence of each dye individually is monitored. The excitation and emission wavelengths for the probes used in this study are detailed in Table A.1. The FRET pairs used in this work and corresponding emission and excitation wavelengths monitored are described in Table A.2.

TABLE A.1 Emission (λ_{em}) and excitation (λ_{ex}) wavelengths for individual dye fluorescence.

Probe	λ_{ex}	λ_{em}
Trp	284	335
DHE	327	393
FAST DiO	477	503
BODIPY-PC	500	520

TABLE A.2 Emission (λ_{em}) and excitation (λ_{ex}) wavelengths for FRET pairs used in this study.

Donor	Acceptor	λ_{ex}	λ_{em}
Trp	DHE	284	393
Trp	BODIPY-PC	284	520
DHE	FAST DiO	327	503
DHE	BODIPY-PC	327	520

A.4 GWALP23 K_p in nanoscopic mixtures

We prepared sample trajectories parallel to the lower tieline for the nanoscopic mixtures, DSPC/POPC/chol and bSM/POPC/chol. FRET from GWALP23 tryptophan to BODIPY-PC is shown in Figure A.2. Though the best fit solid lines indicate K_p of the peptide is 4 ± 1 and 3 ± 1 in DSPC/POPC/chol and bSM/POPC/chol, respectively, the actual preference of the peptide for Ld would be larger than this fitting suggests because domain size is near the magnitude of the Förster Radius, R_0 .

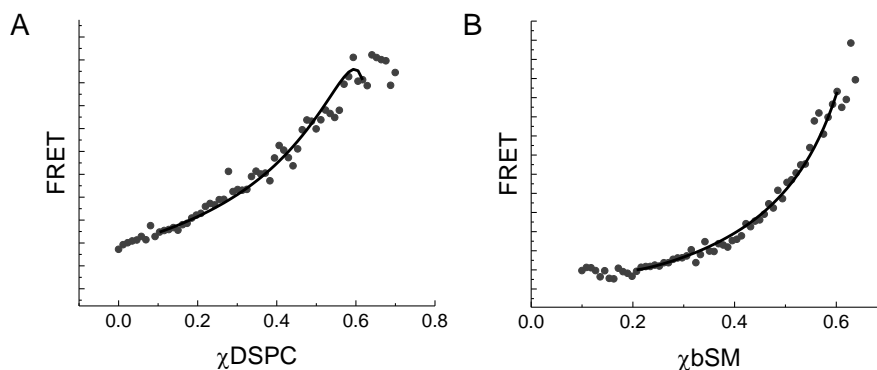


FIGURE A.2 GWALP23 partitions into the Ld phase of mixtures with coexisting nanoscopic Ld + Lo domains. (A) FRET (solid circles, AU) from the GWALP23 tryptophan to BODIPY-PC is plotted with respect to DSPC fraction along the trajectory for DSPC/POPC/chol shown in Figure 2.1A. The best fit (solid line) to Eq. 2 yields $K_p = 4 \pm 1$. (B) FRET (solid circles, AU) from the GWALP23 tryptophan to BODIPY-PC is plotted with respect to bSM fraction along a trajectory parallel to the lower tieline of the two-phase region for bSM/POPC/chol (4) analogous to that shown in Figure 2.1A. The best fit (solid line) to Eq. 2 yields $K_p = 3 \pm 1$. Trajectories included 0.5 mol% GWALP23.

A.5 C12:0 DiI Fluorescence calibration

GUV preparations included 0.1 mol% C12:0 DiI. The sample size was varied and lipid concentration was determined by phosphate assay (7). We collected the fluorescence of C12:0 DiI (547/565 ex/em) for these samples. As anticipated, the steady state fluorescence of C12:0 DiI included at a fixed fraction is directly proportional to the lipid concentration, Figure A.3. Thus, the ratio of GWALP23 Trp fluorescence to C12:0 DiI fluorescence is indicative of the protein:lipid ratio in GUV preparations.

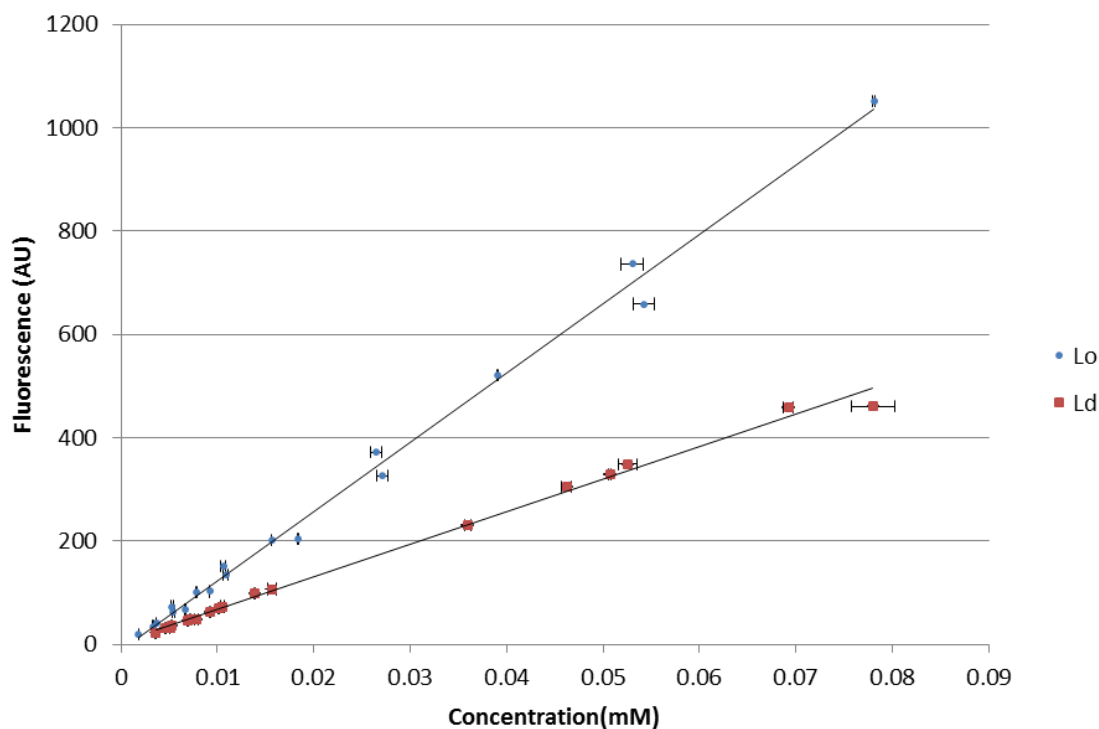


FIGURE A.3 C12:0 DiI fluorescence is directly proportional to the lipid concentration. C12:0 DiI fluorescence in Ld (red squares) and Lo (blue circles) is plotted with respect to lipid concentration.

A.6 EPR experiments

In an effort to understand how GWALP23 affects membrane lipids, we also conducted EPR experiments using 7PC and 16PC probes. EPR spectra are shown in Figure A.4, and the data is summarized in Table A.3. We find the peptide did not significantly affect order along the acyl chains in DSPC/DOPC/chol for Ld. the order and the rate of motion of the acyl chains in Ld did not change in the presence of up to 4 mol% GWALP23. This implies that the significant increase in the bending modulus was not caused by a significant change in the material properties of each leaflet of Ld.

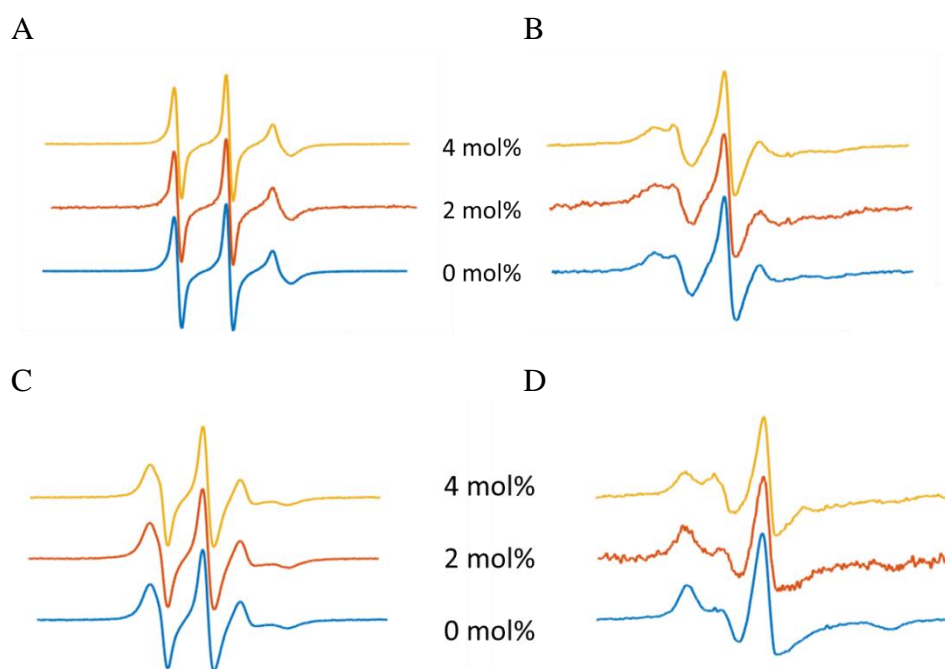


FIGURE A.4 EPR spectra for Ld (A, B) and Lo (C, D) with 16:0-16 Doxyl PC (A, C) and 16:0-7 Doxyl PC (B, D) with 0 (blue), 2 (orange), and 4 (yellow) mol% WALP23.

TABLE A.3 DSPC/DOPC/chol Ld and Lo order parameters (S_{Ld} and S_{Lo} , respectively) with 0, 2, and 4 mol% GWALP23. Order parameter for Lo with GWALP23 not depicted based on OCD experiments.

spin label	GWALP23 (mol%)	S_{Ld}	S_{Lo}
16 Doxyl PC	0	0.13	0.33
	2	0.12	
	4	0.13	
7 Doxyl PC	0	0.29	0.41
	2	0.28	
	4	0.29	

A.7 Partitioning of FAST DiO at high- and low-cholesterol

For the mixture DSPC/DOPC/chol, we determined the partition coefficient of FAST DiO between Ld and Lo at low and high cholesterol content. The K_p of FAST DiO is 12 ± 2 at low cholesterol content and 4 ± 1 at high cholesterol content, Figure A.5. This change in K_p mirrors the change in K_p observed for GWALP23, Figures 2.2.A and 2.7.

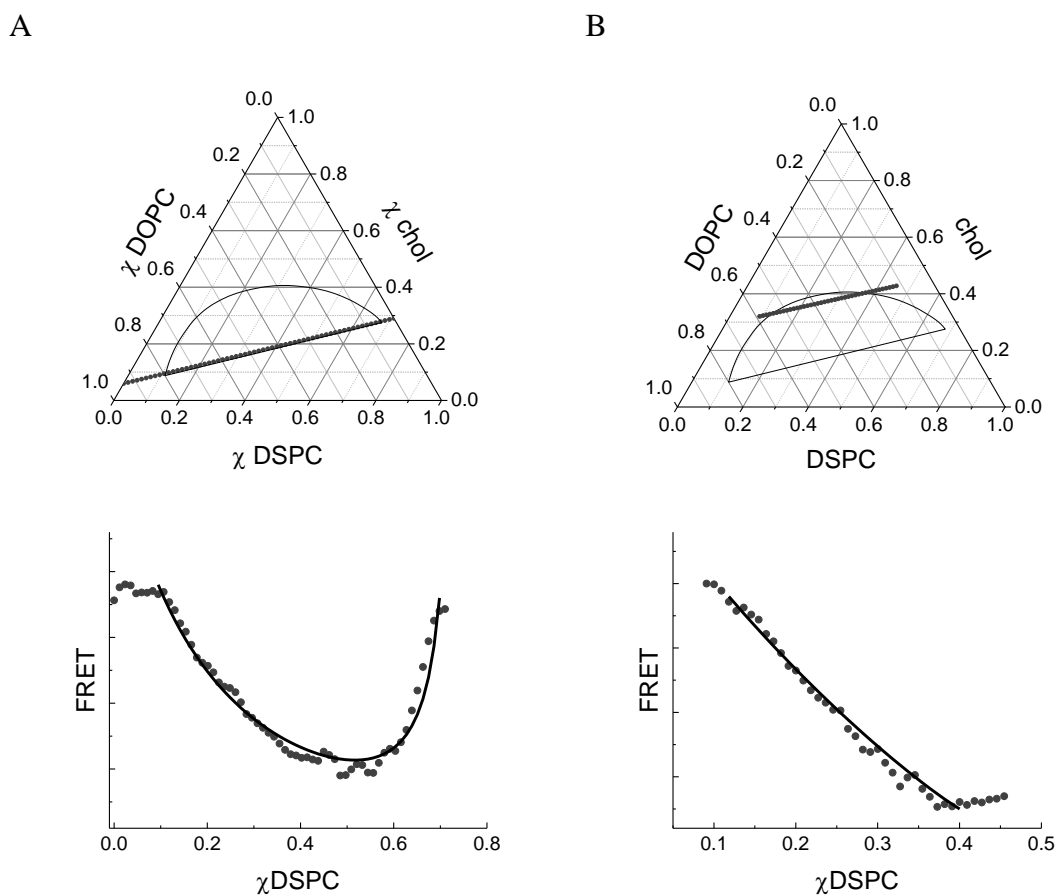


FIGURE A.5 FAST DiO K_p decreases with increased cholesterol content. (A) Diagram showing the sample compositions used in low-cholesterol trajectory coinciding with the lower tie-line of the two-phase region. Intensity of FRET from DHE to FAST DiO along the trajectory is shown in the lower panel. The best fit of the experimental data (solid line) yields $K_p = 12 \pm 2$. (B) Diagram illustrating the compositional space traversed by the high-cholesterol trajectory and the phase

coexistence region (Ld+Lo) for DSPC/DOPC/chol. Lower panel shows the intensity of FRET from DHE to FAST DiO. The best fit of the experimental data (solid line) yields $K_p = 4 \pm 1$.

A.8 Bending modulus of DOPC + GWALP23

For comparison to the ternary mixtures, we measured the bending modulus of a simplified Ld phase, DOPC, with peptide. Like the ternary Ld phases, the bending modulus increased with peptide concentration, but the increase was more gradual. For this simplified Ld phase, GUV yield could be maintained with a higher fraction of peptide.

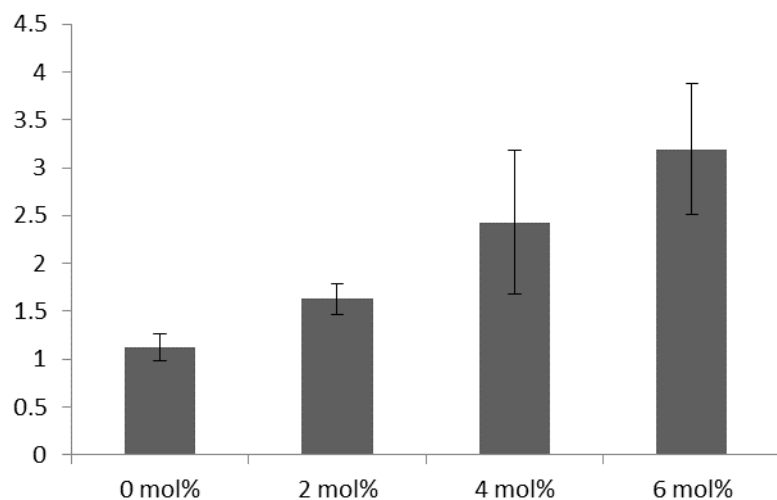


FIGURE A.6 GWALP23 increases the membrane bending rigidity of the DOPC membranes. Bending moduli, κ , in 10^{-19} J of DOPC with 0, 2, 4, and 6 mol% GWALP23.

A.9 References

1. Usery, R.D., T.A. Enoki, S.P. Wickramasinghe, M.D. Weiner, W.-C. Tsai, M.B. Kim, S. Wang, T.L. Torng, D.G. Ackerman, F.A. Heberle, J. Katsaras, and G.W. Feigenson. 2017. Line Tension Controls Liquid-Disordered + Liquid-Ordered Domain Size Transition in Lipid Bilayers. *Biophys. J.* 112: 1431–1443.
2. Henriksen, J.R., and J.H. Ipsen. 2002. Thermal undulations of quasi-spherical vesicles stabilized by gravity. *Eur. Phys. J. E. Soft Matter.* 9: 365–74.
3. Akashi, K., H. Miyata, H. Itoh, and K. Kinoshita. 1996. Preparation of giant liposomes in physiological conditions and their characterization under an optical microscope. *Biophys. J.* 71: 3242–50.
4. Petruzielo, R.S., F.A. Heberle, P. Drazba, J. Katsaras, and G.W. Feigenson. 2013. Phase behavior and domain size in sphingomyelin-containing lipid bilayers. *Biochim. Biophys. Acta.* 1828: 1302–13.
5. Konyakhina, T.M., J. Wu, J.D. Mastroianni, F.A. Heberle, and G.W. Feigenson. 2013. Phase diagram of a 4-component lipid mixture: DSPC/DOPC/POPC/chol. *Biochim. Biophys. Acta.* 1828: 2204–14.
6. Zhao, J., J. Wu, F. a Heberle, T.T. Mills, P. Klawitter, G. Huang, G. Costanza, and G.W. Feigenson. 2007. Phase studies of model biomembranes: complex behavior of DSPC/DOPC/cholesterol. *Biochim. Biophys. Acta.* 1768: 2764–76.
7. Kingsley, P. B., Feigenson, G.W. 1979. The Synthesis of a Perdeuterated Phospholipid: 1,2-dimyristoyl-sn-glycero-3-phosphocholine-d72. *Chem. Phys. Lipids.* 24: 135–147.

Appendix B

Supporting Material for Chapter 3:

Line Tension Controls Liquid-disordered + Liquid-ordered Domain Size Transition in Lipid Bilayers*

Contents

B.1. Line tension measurements	163
B.1. 1. Sample Preparation and cooling procedure	163
B.1. 2. Sample Compositions	166
B.1. 3. Optimizing Probe Concentration	166
B.1. 4. Data Acquisition and Analysis	167
B.1.5. Testing for light-induced effects on line tension	169
B.1.6. Cooling Controls	171
B.1. 7. Size Dependence Controls	172
B. 2. Small Angle Neutron Scattering (SANS)	173
B.3. Molecular Dynamics (MD) simulations	176
B.4. Bending Modulus measurement for DSPC/DOPC/POPC/chol	178
B.4.1. Sample composition	178
B.4.2. Analysis Methods and Validation	179
B.5. Single-Dye Fluorescence Trajectories	180
B.5.1. Phase Diagram and Sample Trajectories	180
B.5.2. Quenching Correction	181
B.5.3. Partition Coefficient Analysis	182
B.6. Probe Partition Coefficient Determination for GUVs	184
B.7. Electron spin resonance (ESR)	186
B.8. Dipole-Dipole Repulsion Model	188
B.9. References	200

* Usery R, Enoki T, Wickramasinghe S, Weiner M, Tsai W, Kim M, Torng T, Ackerman D, Heberle F, Katsaras J, Feigenson G. 2017. Line Tension Controls Liquid-Disordered + Liquid-Ordered Domain Size Transition in Lipid Bilayers. *Biophys J.* 112(7):1431-1443.

B.1. Line tension measurements

B.1. 1. Sample Preparation and cooling procedure

For ρ window measurements, samples contained 0.02 mol% C12:0 DiI; GUVs were made by electroformation with several modifications (1). The lipid films that formed after evaporation in vacuum were swelled at 45°C (when containing bSM, eSM or pSM) or 55°C (when containing DSPC) in 100 mM sucrose under a 5 Hz AC field for 2 h to form the GUVs. To measure ρ windows, the slides were cooled to room temperature (21°C) over 10 h and the vesicles harvested into 100 mM glucose solution in glass test tubes. Samples rested for ~ 1 h so that the sucrose-containing GUVs could settle through the less dense glucose solution. This procedure removes lipid debris, hence background signal, from the GUVs.

To measure line tension, samples contained 0.2 mol% C12:0 DiI, and GUVs were formed as above but were cooled in two different ways to form domains of a suitable size as described in the main text. For low ρ values, circular lipid domains with ~5 μm diameter were obtained by cooling GUVs from 50 to 23°C over ~ 3 h. For higher ρ values, very large round Ld + Lo domains formed over several hours, so the necessary smaller round domains were obtained by faster cooling. In detail, room temperature GUV samples were reheated briefly to 50°C, then 3-4 μl of the sample was deposited into the slide chamber maintained at either room temperature or cooled prior to sample deposition, depending on what was required to obtain ~5 μm diameter domains. Before imaging, GUVs were allowed to settle for 5 minutes on the microscope slide. Circular lipid domains with ~5- μm diameter were then studied at 23°C. The cooling procedure for each sample is summarized in Table B.1, followed by a more detailed description of each protocol.

TABLE B.1 Fast cooling techniques used in different four-lipid systems

Four-lipid systems	Composition	ρ values	Fast cooling setup
DSPC/DPhPC+DLPC/chol	0.5/0.23/0.27	0-0.2	Immediately visualized
		0.3-0.6	Heated up to 45°C and quickly cooled to 23°C
		0.8-1.0	Heated up to 45°C and quickly cooled to 0°C
DSPC/DOPC/POPC/chol	0.39/0.39/0.22	0-0.6	Cooled to room temperature over 10 hours, re-heated up to 50°C and quickly cooled to room temperature
DSPC/DPhPC/POPC/chol	0.39/0.39/0.22	0-0.3	Cooled to room temperature over 10 hours, re-heated up to 50°C and quickly cooled to room temperature
bSM/DOPC+POPC/chol	0.39/0.39/0.22	0.5-0.7	Cooled to room temperature over 10 hours and re-heated up to 50°C and quickly cooled to 0°C
		0.8-1.0	Cooled to room temperature over 10 hours, re-heated up to 50°C and quickly cooled to room temperature
eSM/DOPC+POPC/chol	0.39/0.39/0.22	0.1-0.2	Cooled over 3.5 hours + Heated up to 50°C and quickly cooled to room temperature
		0.3-1.0	Cooled to room temperature over 10 hours and re-heated up to 50°C and quickly cooled
pSM/DOPC+POPC/chol	0.39/0.39/0.22	0.0-0.05	Cooled over 3.5 hours
		0.1-1.0	Cooled to room temperature over 10 hours and re-heated up to 50°C and quickly cooled to room temperature

bSM/DOPC+POPC/chol + 4mol% WALP	0.39/0.39/0.22	0.1-0.25	Cooled over 3.5 hours
		0.35-1.0	Cooled to room temperature over 10 hours and re-heated up to 50°C and quickly cooled to room temperature

Cooled to room temperature over 10 hours and re-heated to 50 °C and quickly cooled to 0 °C:

Cooled from 45 °C to room temperature over 10 hours and harvested into 100 mM glucose and allowed to settle. The samples were heated back up to 50 °C and then 2-3µl were placed on a slide that had been cooled to 0 °C. The slide was allowed to return to room temperature before imaging.

Heated up to 50 °C and quickly cooled to room temperature:

Cooled from 45 °C to room temperature over 10 hours and harvested into 100 mM glucose and allowed to settle. The samples were heated back up to 50 °C and then 2-3µl were placed on a slide and imaged without any further heating or cooling processes.

Cooled over 3.5 hours:

Cooled from 45 °C to room temperature over 3.5 hours and harvested into 100 mM glucose and allowed to settle. 3-4µl were placed on a slide and imaged without any further heating or cooling processes.

B.1. 2. Sample Compositions

Sample compositions for each mixture were chosen based on which compositions produced small isolated domains. These compositions are displayed in Table B.2.

TABLE B.2. Sample composition used in the line tension measurements for six different lipid mixtures.

Mixture	High-T _m	Low-T _m	chol
PSM/DOPC/POPC/chol	0.39	0.39	0.22
eSM/DOPC/POPC/chol	0.39	0.39	0.22
bSM/DOPC/POPC/chol	0.39	0.39	0.22
DSPC/DOPC/POPC/chol	0.55	0.20	0.25
DSPC/DPhPC/POPC/chol	0.45	0.30	0.25
DSPC/DPhPC/DLPC/chol	0.50	0.23	0.27

B.1. 3. Optimizing Probe Concentration

The short exposure times required to capture domain fluctuations for line tension measurements necessitate intense illumination and/or high probe concentration. The potential for light-induced artifacts increases with both of these parameters (2). To limit artifacts during the optimization of probe concentration and data collection, we used a four-component mixture of fully saturated lipids: DSPC/DPhPC/DLPC/chol. DPhPC, when it is the only low-T_m lipid, gives rise to macroscopic phase separation, whereas DLPC as the sole low-T_m lipid yields nanodomains. Here, $\rho = \text{DPhPC} / (\text{DPhPC} + \text{DLPC})$. Initial tests of probe concentration were

carried out at the ρ value where macroscopic phase separation first occurs for this four-component mixture. Increasing concentrations of probes, LR-DOPE and 12:0 DiI, were tested to achieve the best balance of GUV yield and contrast. 0.2 mol% C12:0 DiI proved to be ideal for line tension measurements. Higher probe concentrations tended to reduce yield while at the same time increasing the likelihood of light induced artifacts.

B.1. 4. Data Acquisition and Analysis

All microscopy measurements used an inverted Nikon Eclipse TI-E (Nikon Instruments), with a 60x 1.2 NA water immersion objective, and additional 1.5x intermediate magnifier for line tension measurements. Excitation of DiI was via a Spectra X Light Engine (Lumencor, Inc.) with a green LED (542/27). To narrow the wavelengths of excitation and emission, we used a filter cube with 545/25 excitation filter and 605/70 emission filter. Images were acquired using a Zyla 5.5 sCMOS camera (Andor Tehcnology Ltd) with 6.4 μ m pixels. With a total of 90x magnification for line tension, each pixel represented \sim 71nm. Data acquisition and control of illumination intensity were performed using the software NIS-Elements Basic Research (MVI, Inc).

For reliable line tension measurements, we looked at the top center of a GUV for approximately-circular domains greater than 5 μ m in diameter but less than 1/5th of the diameter of the entire GUV (3). For each domain, we acquired a 15 s time series: 10 ms exposure times with a 30 ms cycle time, yielding \sim 500 frames. A minimum of 10 such domains were imaged for each ρ value. It was a challenge to find domains that were both circular and of a useful size and at the top of the GUV. For all four-component mixtures, we can only start to measure line tension at a ρ value where phase separation is visible under the light microscope and for which circular domains can form. This was often at a ρ value just slightly higher than that at the first

appearance of macroscopic domains. To find such domains, we searched the sample using fluorescence at a low 2% illumination intensity of the Spectra X. Once a useful domain was found, data were collected at 50% illumination intensity. During the acquisition, the Spectra X was triggered by the camera so that the LED was only on during the 10 ms exposure time. During the 20 ms between frames, the LED was off. This reduced light exposure, minimizing light-induced artifacts.

Analysis of domain fluctuations was implemented using Matlab 2010a and followed the basic methodology of Baumgart et al (3). The software located domain boundaries throughout a time series using Matlab's Canny edge detection, taking the largest boundary to define the domain of interest (Figure B.1). A domain in a particular frame was only considered for analysis ("valid") when it was approximately circular and within 3% of the original domain area. The average Fourier transform of the valid boundaries was then used to calculate σ for each mode using Equation 2.1. The line tension of a domain was taken to be the average σ over modes $n = 2 - 5$. Averages were only considered valid if the time series had more than ~ 250 valid frames and produced relatively constant values of σ over modes $n = 2 - 5$.

We used only modes 2-5 for the analysis in part because they were shown by Baumgart et al. to effectively measure line tension, and also because we empirically found them to accurately measure line tensions in fluctuating domain simulations analogous to those described in Baumgart et al (3).

Evidence that this method works is shown in Figure B.1, where it is straightforward to see the differences in measured line tension for domains at low and high ρ . For bSM/DOPC/POPC/chol, macroscopic phase separation is first observed at $\rho \sim 0.50$ with a line tension value of 0.29 ± 0.04 pN (Figure B.1 A, B). At $\rho = 1.00$, the line tension is 1.3 ± 0.1 pN

(Figure B.1 C, D). The greater fluctuation amplitudes visible in A and B are consistent with lower line tensions compared to C and D.

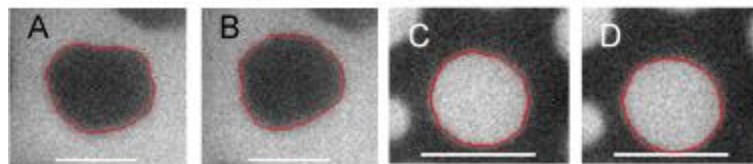


Figure B.1. Snapshots of domains over time, with detected boundaries outlined in red, show differences in line tension. A,B) Domain at $\rho = 0.5$ with an average line tension of 0.29 ± 0.04 pN. The time between A and B is ~ 0.75 s. C,D) Domain at $\rho = 1.00$ with line tension 1.31 ± 0.12 pN. The time between C and D is ~ 0.75 s. Scale bars are $5 \mu\text{m}$.

B.1.5. Testing for light-induced effects on line tension

Since the dye concentration of 0.2% is rather high in order to achieve the required contrast, there is a possibility of light-induced artifacts. These can result in the break-up of domains, the fusion of domains, or a change in the amplitude and frequency of the fluctuations of the domains. Therefore, we always test for any light-induced artifacts by measuring the change in line tension over time. For each domain, the data were split into successive subsets of 100 frames (successive subsets of 3 s time intervals); the first subset containing data from time 0-3 s, the second subset containing data from time 3-6 s, etc. For a given domain, the line tension value for each subset was normalized to the line tension value in the first 100 frames. These data were then averaged together over all domains at each ρ value (Figure B.2). While there were some fluctuations in the normalized line tensions, most ρ values exhibited no illumination- or time-dependent trends. For DSPC/DOPC/POPC/chol, at $\rho = 0.2$, Figure B.2 shows a decrease in line tension by nearly 50% from the first subset to the second, for instance. This unreliable change is considered to be due to light induced artifacts, and this kind of data was then discarded. This composition was carefully remeasured to avoid light induced artifacts.

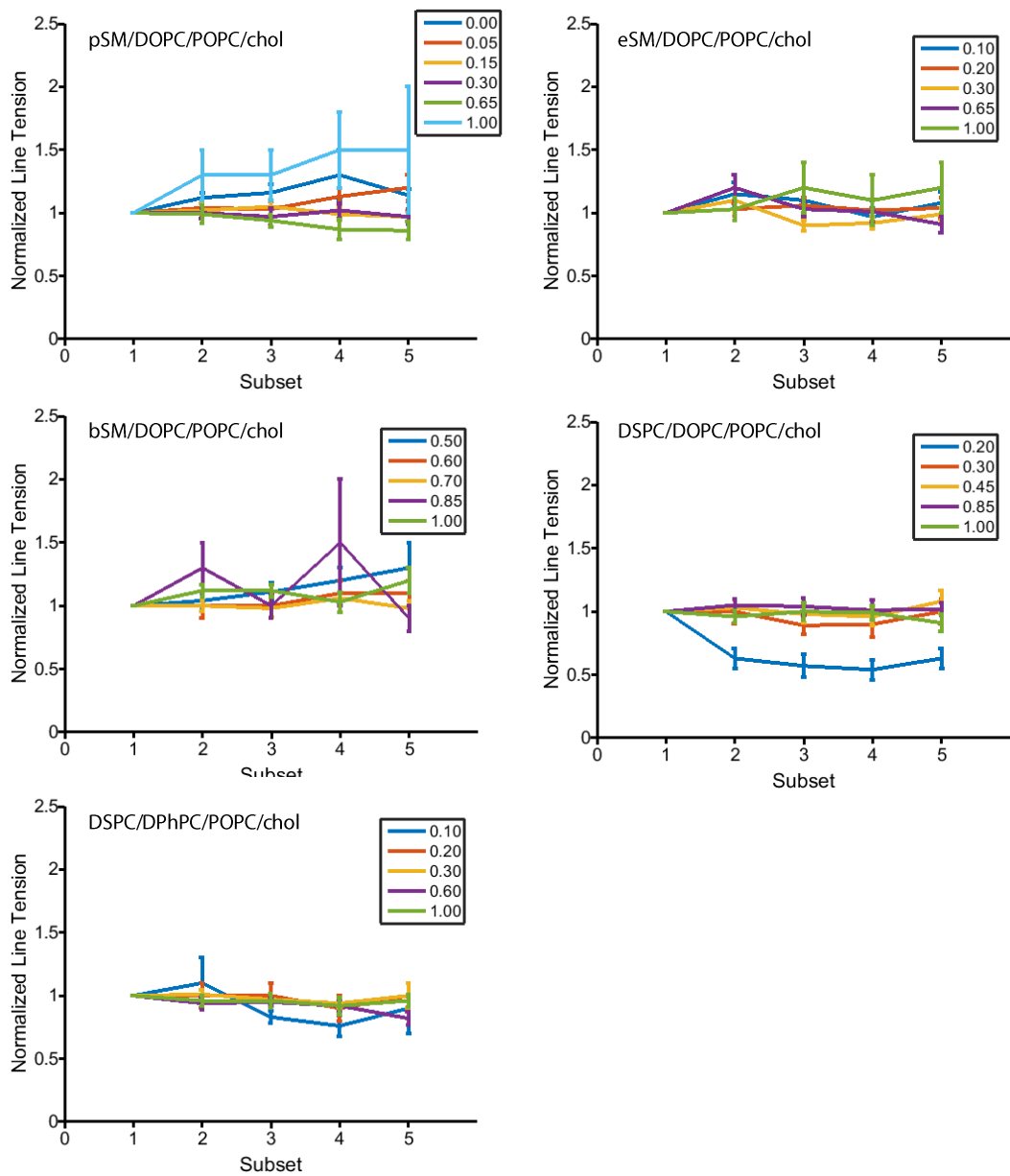


Figure B.2. Light-induced effects can be detected by measuring line tension over time. For these tests, an average line tension of each successive subset of 100 frames is normalized by the line tension in the first 100 frames. The legend indicates the system's ρ value.

The effect of such light-induced artifacts can be clearly seen in Figure B.3, where we show a single domain at this composition throughout its 15 s exposure. While the domain starts off round, by 15 s, its shape is very irregular. This data was discarded.

We note that for each of the 6 mixtures studied, the trend in line tension versus ρ was similar for each subset. This, together with the fact that most ρ values show no trend in line tension over time, allows us to conclude that light-induced effects were negligible.

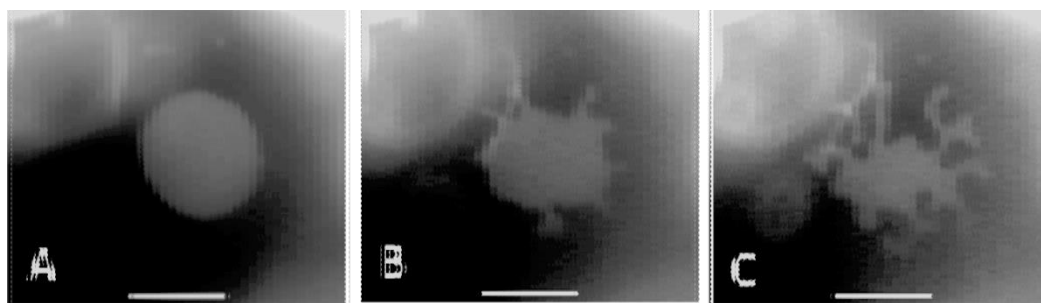


Figure B.3. Domain exhibiting light induced artifacts. Domain at $\rho = 0.2$ for DSPC/DOPC/POPC/chol, at A) $t = 0$ s, B) $t \sim 7.5$ s, and C) $t \sim 15$ s. This domain was not used for analysis, but shows how a round domain can become misshapen over time due to illumination. Scale bars are $5 \mu\text{m}$.

B.1.6. Cooling Controls

To ensure that the measured line tension values did not differ based on the cooling method used — slow cooling over 3.5 hours or fast cooling over a few seconds — the pSM/DOPC/POPC/chol and eSM/DOPC/POPC/chol systems were imaged after making samples using both cooling protocols. Since different methods of cooling were required to obtain suitable domains for different ρ values, only a few ρ values for the pSM and eSM could be imaged using *both* methods of cooling. The line tension values observed show that the values

of the line tension are within the standard error of each other and follow similar trends regardless of slower or faster cooling method (Figure B.4). The line tension values shown in the main text are the values obtained from domains using both cooling methods.

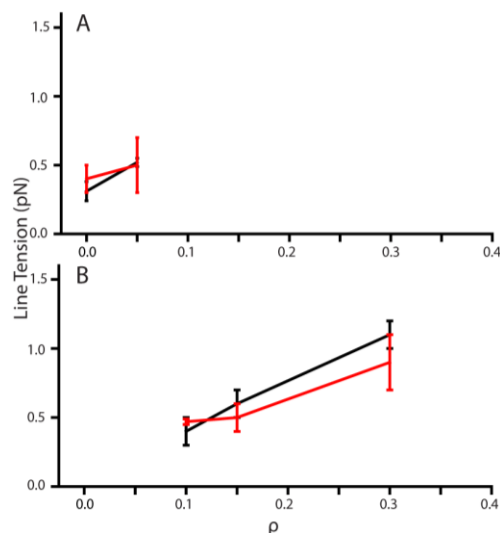


Figure B.4. Line tension measurements using faster (black) or slower cooling (red) are the same for A) pSM/DOPC/POPC/chol and B) eSM/DOPC/POPC/chol. Error bars: mean \pm standard error.

B.1. 7. Size Dependence Controls

GUV and domain radii were recorded for all measurements. To ensure that the line tension measurement itself does not depend on the size of the domain or the size of the GUV it is on, we have compared normalized line tension to size, where line tensions were normalized to the average line tension for a given composition. In Figure B.5 A it can be seen that the normalized line tensions remain close to one, meaning that line tension is independent of domain radius. Similarly, line tension is independent of GUV radius as shown in Figure B.5 B. The ratio of domain size to GUV size is another factor that could cause a distortion in measured line

tension, but importantly, for the domains used in this study, the line tension measurement is independent of this ratio (Figure B.5 C).

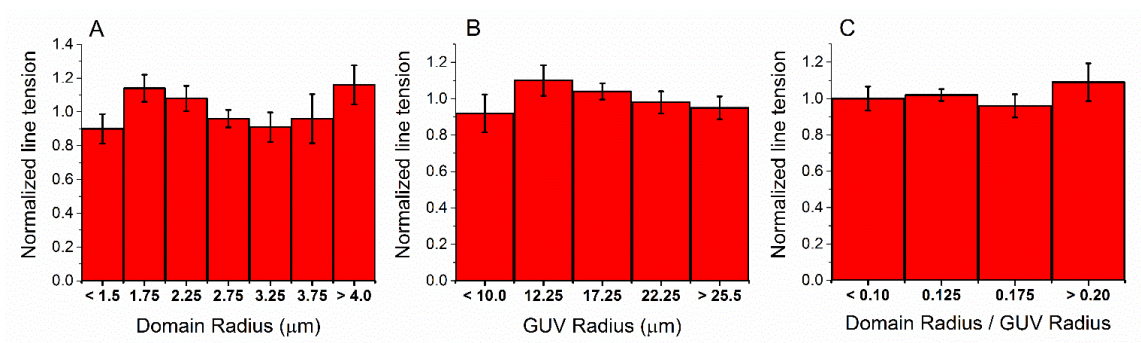


Figure B.5. DSPC/DPhPC/DLPC/chol line tension is independent of domain size and GUV size. At each ρ value each line tension measurement was normalized to the average of all measurements at that ρ value. Normalized line tension was compared to domain radius (A), to GUV radius (B) and to the ratio of the two (C). Bars reflect bins of approximately equal size.

B. 2. Small Angle Neutron Scattering (SANS)

SANS $I(q)$ data were analyzed with a coarse-grained Monte Carlo method described in Heberle et al. (4). Briefly, vesicles were modeled as spherical shells of radius R_v and thickness t_{ac} corresponding to the hydrophobic thickness of the bilayer, with polydispersity assumed to follow a Schulz distribution (5). The shell volume was divided into one or more randomly placed, non-overlapping circular domains of radius R_d . Random points were generated within the shell volume in proportion to the neutron scattering length density (NSLD) contrast of the bilayer phases with the surrounding water using a rejection algorithm (*i.e.*, points were uniformly generated within the shell and tested for inclusion in a domain until both phases accumulated the desired number of points). The NSLD-weighted pair distance distribution $P(r)$

was calculated from the set of random points, and the procedure was repeated for 10^5 vesicles to obtain an ensemble average. The scattering intensity was then calculated as (6):

$$I(q) = 4\pi \int_0^\infty P(r) \frac{\sin qr}{qr} dr. \quad (\text{B.1})$$

For best S/N in SANS measurements we used compositions where area fractions of Ld and Lo were nearly equal. Most trajectories for line tension measurements used the same compositions. Samples were prepared near the lowest-chol tieline of the Ld + Lo region where the compositions of the coexisting phases are well determined, which is a necessity for the bending energy and ESR experiments.

We explored a wider range of LUV size at a single ρ value to find any influence on measured nanodomain size. Figure B.6 shows domain sizes at $\rho = 0$ for DSPC/POPC/chol, obtained from extruded vesicles with nominal extrusion pore sizes ranging from 30 – 200 nm diameter (Figure B.6, open squares). Extrusion of neutral lipids using pore sizes ≥ 100 nm is known to generate a minor population of paucilamellar vesicles (PLVs) that can be eliminated by adding a small fraction of charged lipid to the mixture (7). To test whether Bragg scattering from contaminating PLVs might affect the determination of domain size, samples were also prepared in which 5 mol% of each PC lipid was replaced with its PG counterpart (Figure B.6, diamonds). Within measurement uncertainty, domain size has a negligible dependence on vesicle size at $\rho = 0$: all measured domain radii fall in the range 5.0 – 6.8 nm. The presence of 5 mol% PG resulted in a ~5% decrease in domain size (Figure B.6).

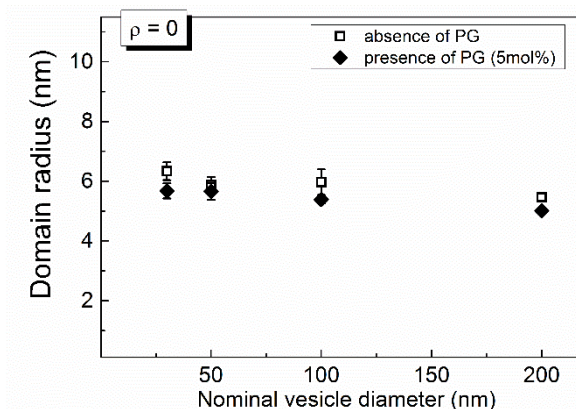


Figure B.6. SANS reveals that nanodomain size is independent of vesicle size. Domain radii obtained from Monte Carlo modeling of SANS data for LUVs composed of DSPC/POPC/chol = 39/39/22. At this $\rho = 0$ composition, the domain radius is independent of vesicle size and does not change significantly upon addition of 5 mol% charged lipid.

Discussion of Nanoscopic Phase Separation

As we discuss in detail in the main text, properties of Ld and Lo phases, such as bending energy, order parameter, rotational diffusion, and probe partitioning between phases gradually change on either side of the dramatic domain size transition and change rather little through the transition itself. In this sense the size transition does not have the hallmarks of a phase transition (8).

Previous experimental observations are consistent with Ld + Lo nanoscopic domains being phase separated mixtures. These mixtures were found to have all of the same phase coexistence regions as mixtures that show macroscopic domains. Indeed, the formation of Lo phase from L β phase occurs at $\chi_{\text{chol}} \approx 0.16$ in all the mixtures we have studied, leading to similarities for different lipid mixtures in this region of the phase diagram (9–11). Of particular importance is the finding that the high-chol "upper" boundary of the Ld + L β coexistence region

in a Gibbs Triangle phase diagram is a straight line in composition space in all the mixtures we have studied (9–11). This is readily explained if the region above $L_d + L_\beta$ is a three-phase coexistence triangle of $L_d + L_\beta + L_o$, which has been directly verified for a macroscopic mixture by fluorescence microscopy observations (12). Because the $L_d + L_\beta$ upper boundary is linear in nanoscopic mixtures (10, 11), there is no critical point, consistent with an adjacent 3-phase region. In turn, this three-phase region must, according to the Phase Rule, be adjacent to a region with either four or two phases, inconsistent with this region being a one-phase microemulsion. Further, Goh et al. measured the areas of the modulated phase domains in GUVs and found the observed area fractions to follow the Lever-Arm Rule. This implies that the uniform surround must itself be a single phase, otherwise the Lever-Arm Rule would fail to describe the area fractions.

B.3. Molecular Dynamics (MD) simulations

Figure B.7 displays the full bilayer of a 20,000-lipid MD simulation at three ρ values: 0.5, 0.65, and 0.8. Each is displayed after phase separation, and the increasing size and connectivity of domains is visible as ρ increases. This increase in size and connectivity means a decrease in interface length between two phases, consistent with rising line tension. A 30 nm x 30 nm portion of the $\rho = 0.65$ plot (Figure B.7 B) which contains a single nanodomain is shown in the main body of this paper and was run for 3.6 μ s. The other simulations represent the system after 1.2 μ s. The additional time was found to not change phase morphology, implying 1.2 μ s is sufficient for equilibration.

Any analysis on such a system depends on how we define a phase in a simulation. In order to prevent very small patches of one or a few lipids from being classified as domains, an

adjustment was implemented: If a majority of a given lipid's nearest neighbors including itself were classified in the first round as being in a particular phase, the lipid was assigned to that phase in the second round. Our method is but one of several based on measuring local enrichment of high-T_m lipid (13, 14). A choice to compare neighboring phases twice is somewhat arbitrary but serves to remove clusters too small to be considered domains. Otherwise, the nonrandom clustering of lipids representing a small component of a phase can be mislabeled. A test of k-means clustering based on local composition revealed nearly identical classifications of lipids into phases. A further study of a large bilayer over a long time scale (> 10 μs), while computationally expensive, would provide further detail into the time-dependent properties of nanodomains, including their changing perimeters and whether individual domains form or disappear in a system already at equilibrium.

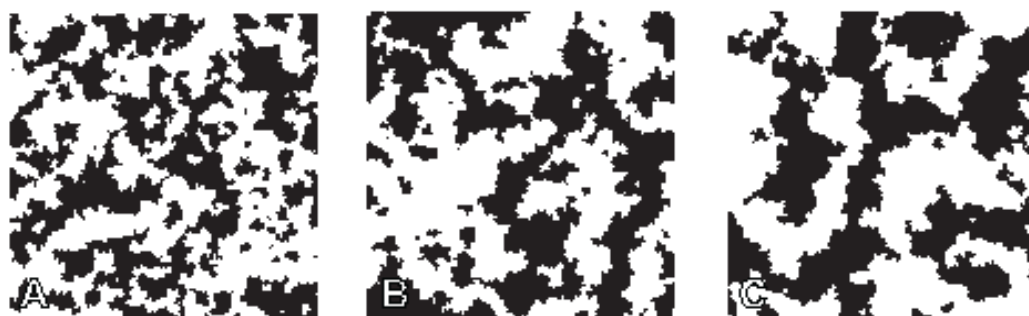


Figure B.7 Size and connectivity of domains increases as ρ increases. Lo is shown in black, and Ld is shown in white. Panels depict increasing ρ with (A) $\rho = 0.5$, (B) $\rho = 0.65$, and (C) $\rho = 0.8$. The visible decrease in interface length is consistent with rising line tension. Each simulation has a box size of approximately 74 nm x 74 nm.

Our Molecular Dynamics movie demonstrates the dynamic shape and evolution of nanodomains. It shows the progression of a single 4-component system as it develops during phase separation and then continues rearranging. The time progression reveals the complex,

non-circular morphology of a domain and its fluctuating nature. Lipids are colored by type (DUPC in blue, PUPC in cyan, DPPC in red, and cholesterol in yellow). Phases are not marked, but the formation of patches rich in DPPC and cholesterol (red and yellow) clearly shows the formation of Lo domains.

B.4. Bending Modulus measurement for DSPC/DOPC/POPC/chol

B.4.1. Sample composition

Bending modulus measurements were performed in DSPC/DOPC/POPC/chol using the lipid composition of Ld phase, DSPC/(DOPC+POPC)/chol = 0.10/0.80/0.10, or Lo phase, as described in Table B.3. It should be noted that the right hand side of DSPC/DOPC/POPC/chol phase diagram changes with ρ . Therefore, the lipid composition used in Lo measurements smoothly change.

TABLE B.3. Sample composition used in bending modulus measurements, showing only Lo phase of DSPC/DOPC/POPC/chol.

ρ	DSPC	(DOPC+POPC)	chol
0	0.58	0.17	0.25
0.2	0.62	0.11	0.26
0.35	0.64	0.09	0.27
0.6	0.67	0.06	0.28
0.8	0.67	0.05	0.28
1	0.68	0.04	0.28

B.4.2. Analysis Methods and Validation

Figure B.8 shows an example of edge detection and the bilayer fluctuations. For these experiments, a 4% difference in osmolality between inner and outer solutions was created, yielding slightly flaccid vesicles suitable for the measurement. Given the density difference of the solutions, vesicles with radii $> 20 \mu\text{m}$ were excluded to avoid significant distortion due to gravity (15). Vesicles of radii $< 10 \mu\text{m}$ have too few pixels defining the contour, leading to poor statistics, and thus were also excluded. Only vesicles exhibiting visible fluctuations and free of defects like tethers, buds, or attachments were imaged. Vesicles contained 0.02 mol% C12 DiI to enable line scans of fluorescent dye intensity to identify and exclude multilayered vesicles.

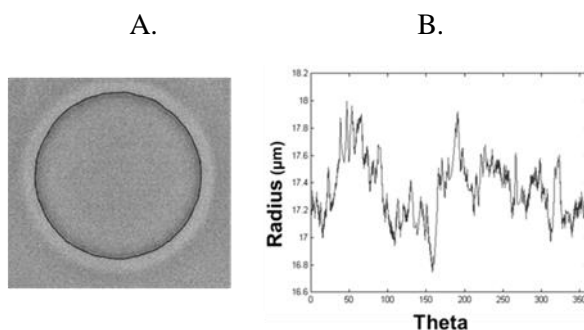


Figure B.8. Fluctuation Spectroscopy Edge Detection. (A) Fluctuations were observed with phase contrast images of the vesicle equator. Contour as defined by Canny edge detection is superimposed in black. (B) Fluctuation spectrum from the contour shown, where theta refers to points on the quasi-circular contour.

Our method for measuring bending moduli closely followed the methods of Gracià et al. (16). Our determination of the range of useful mode numbers hinged on the following considerations: Tension predominates for low modes, and high modes become indistinguishable from noise. Thus an intermediate range of modes, numbers 10 to 20, provides a reliable measure

of the bending modulus (16). Measurements which did not result in a plateau of these modes were considered unreliable and excluded from the composition average.

To determine appropriate exposure times, we analyzed the relaxation time of various modes according to: $(4 \eta R^3)/(\kappa_c m^3)$, where η is viscosity, R is radius, κ is the bending modulus, and m is the mode number (17). We determined that 1 ms is an adequate exposure time for the range of bending moduli in our experiments. The Spectra X white light source used for these experiments was triggered by the camera and remained off for 29 ms of the 30 ms cycle time used. Each dataset per vesicle measured included 1600 exposures. Achieving sufficient contrast requires moderately intense light, so we investigated the possibility of light-induced artifacts. For each measurement, datasets were divided into 200-frame subsets. No trends in these subsets were observed (data not shown). We confirmed that our procedure yields values similar to the bending moduli obtained by others (16, 18).

B.5. Single-Dye Fluorescence Trajectories

B.5.1. Phase Diagram and Sample Trajectories

Figure B.9 shows the phase diagram for bSM/POPC/chol ($\rho = 0$) and bSM/DOPC/chol ($\rho = 1$) and the lipid composition of 61 samples prepared along a thermodynamic tieline (two-phase region). These phase diagrams in Figure B.9 are similar to the ones reported in Ref. (11), but here we updated the boundaries somewhat with new measurements. For the intermediate trajectories obtained for $\rho = 0.4$ and $\rho = 0.75$, we interpolated the phase boundaries linearly with ρ . The K_p determination depends on the L_o and L_d phase fractions. The inserted axis in the phase diagram displays the fraction of L_o phase, χ_{L_o} , which represents the independent variable

of Equation B.3 below. The arrows labeled 1 and 2 point to phase boundaries of the coexistence region and represent pure Ld and Lo phases, respectively.

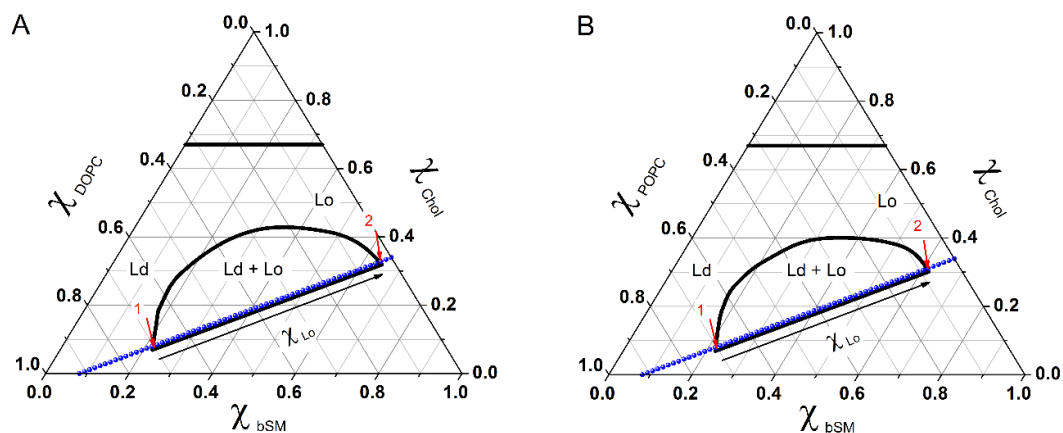


Figure B.9. Phase diagram of (A) bSM/POPC/chol ($\rho = 0$) and (B) bSM/DOPC/chol ($\rho = 1$). Sample trajectories were prepared with the lipid compositions shown in the phase diagram (blue). The inserted axis in the phase diagram displays the fraction of Lo phase, χ_{Lo} , and the arrows labeled 1 and 2 point to the phase boundaries of the coexistence region.

B.5.2. Quenching Correction

For the fluorescence trajectories, dyes were used at a concentration that does not exhibit large self-quenching effects, as displayed in Figure B.10. This study of fluorescence self-quenching is also important for quenching corrections if necessary.

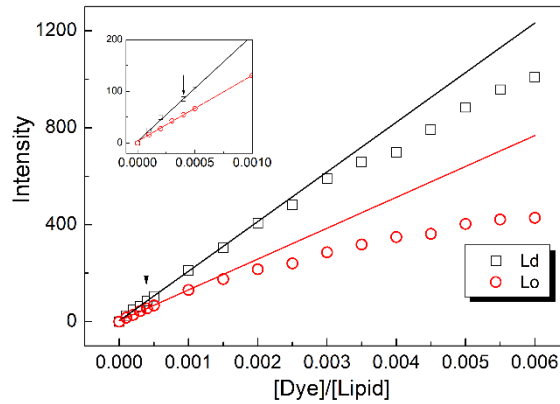


Figure B.10. Fluorescence self-quenching with increasing dye concentration. The self-quenching curve of Bodipy-PC for bSM/DOPC/chol in Ld and Lo phases (composition labeled 1 and 2, respectively, Figure B.9 A) is shown. The inset shows the linearity of Intensity and $[\text{dye}]/[\text{lipid}]$ at low $[\text{dye}]/[\text{lipid}]$ ratios. The small arrow displayed in the graph points to the $[\text{dye}]/[\text{lipid}] = 1/2500$ ratio used in the fluorescence experiments.

B.5.3. Partition Coefficient Analysis

Figure B.11 shows the fluorescence trajectory for bSM/POPC/chol ($\rho = 0$) (also displayed in the inset of Figure 3.2.5). The data were fitted using Equation B.3 below, where χ_{Lo} is the fraction of Lo phase, as shown in Figure B.9.

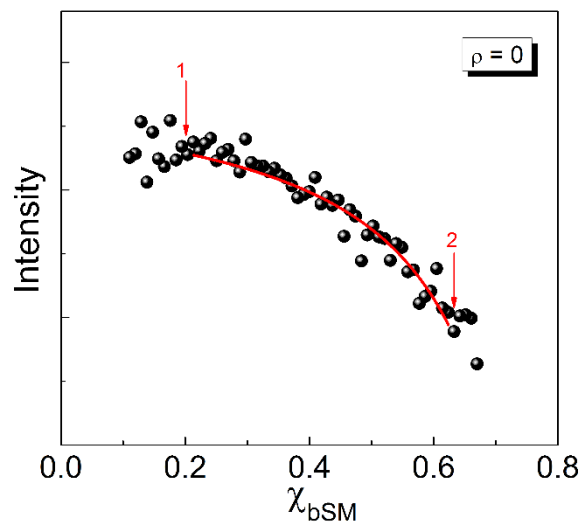


Figure B.11. Fluorescence emission of Bodipy-PC in bSM/POPC/chol. The lipid composition of each sample is displayed in the tieline of Figure B.9. The single dye fluorescence (corrected for quenching effects) was analyzed according to Equation B.2.

The single dye fluorescence along a tieline is given by

$$F = \frac{F_{Ld} Kp (1-\chi_{Lo}) + F_{Lo} \chi_{Lo}}{Kp (1-\chi_{Lo}) + \chi_{Lo}}$$

(B.2)

where F_{Ld} and F_{Lo} are the fluorescence signals from pure Ld and Lo phases, (i.e. the fluorescence at the lipid compositions represented by 1 and 2 in Figure B.11). The partition coefficient is defined by

$$Kp \equiv \frac{n_{Ld}/\chi_{Ld}}{n_{Lo}/\chi_{Lo}} \quad (\text{B.3})$$

such that $Kp > 1$ indicates partitioning that favors the Ld phase, and n_{Ld} and n_{Lo} indicate the fraction of dye in Ld and Lo phase, respectively. The error bars displayed in the Figure 3.5A were calculated by the goodness of fit of Equation B.2.

B.6. Probe Partition Coefficient Determination for GUVs

We used line scans in GUV snapshots to measure the fluorescence intensity ratio between Ld and Lo phases. ImageJ was used to analyze snapshots and record intensity profiles. The intensity ratio between Ld and Lo phases was calculated using the area under the peak in the intensity profiles after subtracting the background intensity. Here, we performed 10 line scans for each phase in a single GUV, and we repeated this procedure for 5-10 different GUVs.

Bodipy-PC is intrinsically brighter in Ld phase compared to Lo phase. It is well known that fluorescent dyes can have different quantum yield (intensities) in different environments (19). Here, we have corrected the intensity ratio between Ld and Lo phases, obtained from the line scans, for the intrinsic fluorescence of the dye in each single phase.

In addition, the partition coefficient obtained by fluorescence trajectories is related to the total fluorescence that comes from Lo and Ld phases. This quantification differs from a single measurement of fluorescent intensity in Ld and Lo phases, as obtained from the line scans. Therefore, in order to compare the partition coefficient obtained using these two different

techniques of fluorescence trajectories and fluorescence microscopy, we considered in our calculations that the Lo phase occupies 30% less area than the Ld phase (20, 21), in order to account for the total intensities from Ld and Lo, observed in the GUVs studies.

Figure B.12 displays an example of the partition coefficient measurement in GUVs. The snapshot in Figure B.12 A represents a typical line scan of Ld and Lo phases. Figure B.12 B displays the 10 different line scans for each phase used in the calculations of the partition coefficient. The error bars displayed in Figure 3.2.5A for K_p measurements on GUVs correspond to standard error of 5-10 GUVs, with 10 line scans for each phase.

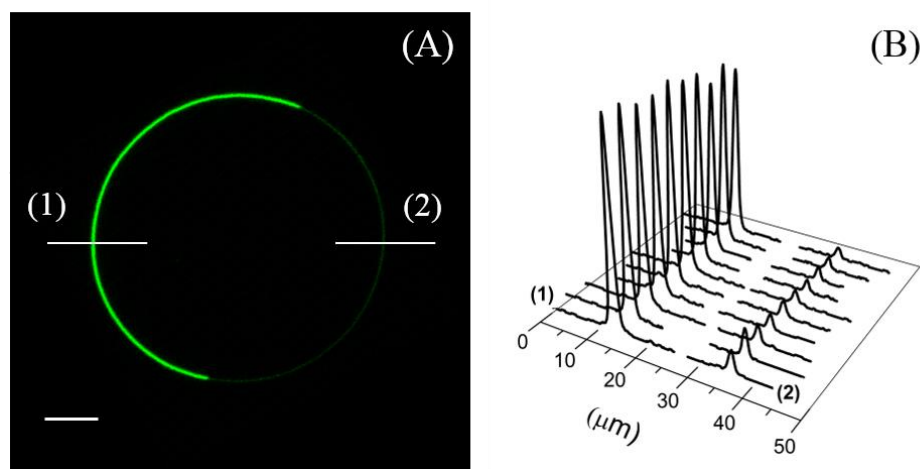


Figure B.12. Intensity profile measurements on GUVs. GUV lipid composition bSM/(DOPC+POPC)/chol = 0.4/0.4/0.2, dye/lipid = 1/2500. (A) Snapshot of a GUV, which exhibits Ld (brighter) and Lo phase separation. Lines labeled by the numbers (1) and (2) are line scans obtained in Ld and Lo phase, respectively. (B) Examples of 10 different line scans measured along Ld (brighter) and Lo phases. Scale bar: 5 μm .

B.7. Electron spin resonance (ESR)

The ESR spectrum of 111 samples measured along ρ for DSPC/DOPC/POPC/chol were analyzed according to equation:

$$S(\rho) = (1 - n_{Lo}) * Ld(\rho) + n_{Lo} * Lo(\rho) \quad (\text{B.4})$$

where $Ld(\rho)$ and $Lo(\rho)$ correspond to the characteristic spectrum of Ld and Lo phase for a certain value of ρ , and $n_{Ld} = (1 - n_{Lo})$ and n_{Lo} represent the fractions of paramagnetic probe in Ld and Lo phase, respectively. Additionally, the characteristic spectra of Ld and Lo phases can be written as a linear combination of the spectra measured in $\rho = 0$ (DSPC/POPC/chol) and $\rho = 1$ (DSPC/DOPC/chol), according to Equations B.5 and B.6.

$$Ld(\rho) = (1 - \rho) * Ld(0) + \rho * Ld(1) \quad (\text{B.5})$$

$$Lo(\rho) = (1 - \rho) * Lo(0) + \rho * Lo(1) \quad (\text{B.6})$$

The partition coefficient is defined according to Equation B.3, except in this case n_{Ld} and n_{Lo} refer to the fraction of 16PC spin label. As mentioned above, χ_{Ld} and χ_{Lo} are the fractions of Ld and Lo phase.

Figure B.13 shows the spectra of (A) Ld phase and (B) Lo phase, for $\rho = 0, 0.3$ and 1 . These spectra represent the phase morphologies of nano domains, modulated phases and macro domains, respectively. We observed small changes in the ESR spectra along ρ reflecting small changes in the order parameter and the rotational diffusion as shown in Table 2.1.

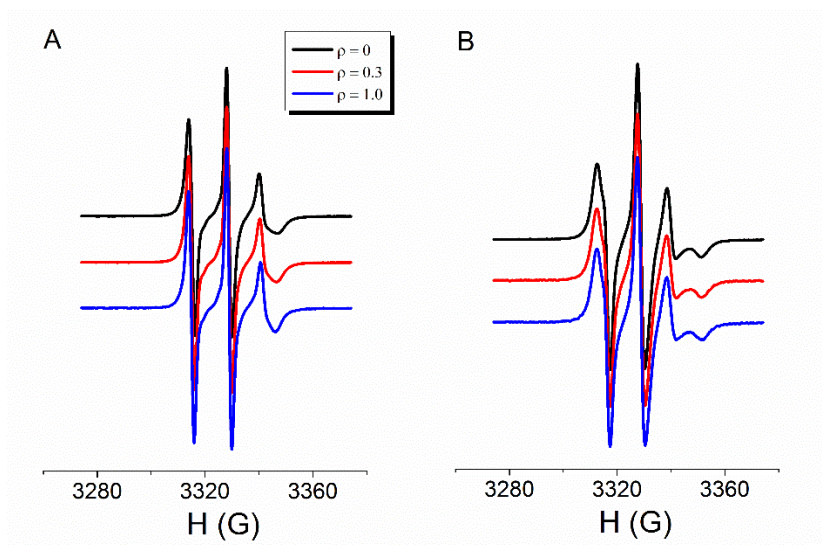


Figure B.13 ESR Spectra change little along ρ for both Ld and Lo. (A) Ld phase spectra. (B) Lo phase spectra. $\rho = 0$ is shown in black, 0.3 in red and 1 in blue. Spectra are shifted for clarity.

B.8. Dipole-Dipole Repulsion Model

In order to explore the implications of dipole repulsion for domain size, we model the total energy of a phase-separated bilayer as a sum of a phase boundary energy from line tension that scales with domain perimeter and an electrostatic potential energy arising from permanent lipid dipoles.

An initial question for these studies is whether dipoles in one leaflet would have their fields largely cancelled by the opposing dipoles in the other leaflet. This does occur for the methyl dipoles that give rise to long-range repulsion in lipid monolayers (22). The dipoles of interest in this study would be farther apart, as shown in Figure B.14, suggesting that the oppositely oriented dipoles would not cancel. This was conclusively shown in the calculations described below and in the main text, wherein two leaflets of oppositely oriented dipoles produce a net repulsive electrostatic interaction when their magnitude and separation distance is comparable to carbonyl groups in a lipid bilayer.

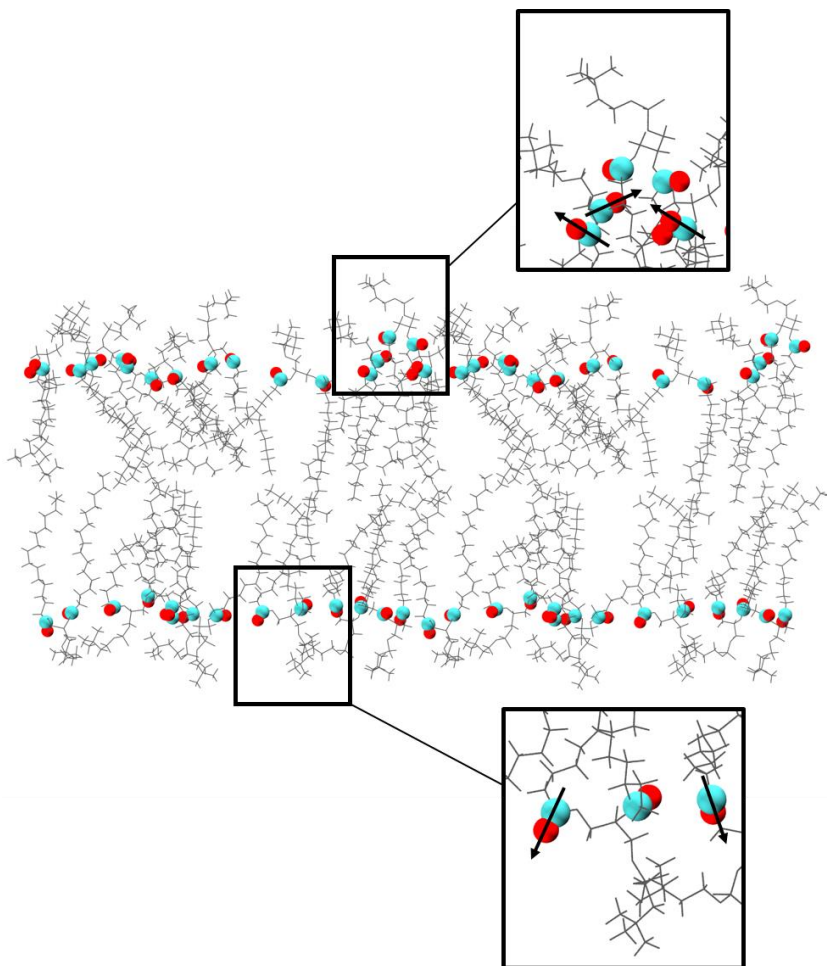


Figure B.14. The direction and location of carbonyl dipoles in a bilayer. Carbonyl groups at the top of each acyl chain are presented as spheres (cyan for carbon and red for oxygen), while the rest of the phospholipid is presented as gray lines. Dipoles drawn pointing from the positive carbon toward the negative oxygen along the bond reveal that the net dipole moment of each leaflet is normal to the bilayer and pointed outward toward the water (inset) and that there is individual variation in the dipole alignment. Phospholipids are displayed in each leaflet as a representation of a system obtained from Molecular Dynamics simulations of a DPPC bilayer.

For the calculations, we needed to determine the energetically favorable domain size for a set of lipid parameters. We therefore chose a fixed total domain area α and varied the number of domains N_D into which that area was divided; assuming circular domains, the domain radius

is given by $R_D = \sqrt{\alpha/(\pi N_D)}$. The energetically favorable domain size R_D^* is defined as that which results in the lowest energy for a given set of parameters defined below.

The energetic contribution from the line tension σ is given by $2\pi R_D N_D \sigma$. To determine the electrostatic contribution, we first considered the electrostatic potential energy for an arbitrary arrangement of discrete dipoles in a membrane:

$$V = \frac{1}{4\pi\epsilon\epsilon_0} \sum_{i=1}^{N_L-1} \sum_{j=i+1}^{N_L} \left[\frac{\overline{\mathbf{p}}_i \cdot \overline{\mathbf{p}}_j}{\|\overline{\mathbf{r}}_{ij}\|^3} - \frac{3(\overline{\mathbf{p}}_i \cdot \overline{\mathbf{r}}_{ij})(\overline{\mathbf{p}}_j \cdot \overline{\mathbf{r}}_{ij})}{\|\overline{\mathbf{r}}_{ij}\|^5} \right], \quad (\text{A.7})$$

where ϵ_0 is the permittivity of free space, ϵ is the dielectric constant (here, the dielectric constant of the bilayer region near the dipoles), N_L is the number of dipoles (here, the number of lipids possessing a permanent dipole), $\overline{\mathbf{p}}_i$ are the dipole moment vectors, $\overline{\mathbf{r}}_{ij}$ are the vectors connecting a pair of dipoles, and $\|\overline{\mathbf{r}}_{ij}\|$ are the distances between these dipole pairs. For lipids distributed identically in the two bilayer leaflets and dipoles aligned with the bilayer normal, the total electrostatic potential energy of the bilayer is a sum of intra- and interleaflet contributions, i.e. $V_{total} = 2V_{intra} + V_{inter}$, with

$$V_{intra} = \frac{1}{4\pi\epsilon\epsilon_0} \sum_{i=1}^{N_L^{top}-1} \sum_{j=i+1}^{N_L^{top}} \left(\frac{(p_i p_j)^2}{\|\overline{\mathbf{r}}_{ij}\|^3} \right), \quad (\text{A.8})$$

$$V_{inter} = \frac{1}{4\pi\epsilon\epsilon_0} \sum_{i=1}^{N_L^{top}} \sum_{j=1}^{N_L^{bot}} \left(\frac{3(h p_i p_j)^2}{\|\overline{\mathbf{r}}_{ij}\|^5} - \frac{(p_i p_j)^2}{\|\overline{\mathbf{r}}_{ij}\|^3} \right). \quad (\text{A.9})$$

Here, N_L^{top} and N_L^{bot} are the number of lipids in the top and bottom leaflets (with one net permanent dipole assigned to each), h is the bilayer thickness, and p_i are the dipole magnitudes. To simplify the calculations, we assumed that the domain and its surround differed only in the magnitudes of their dipoles, and that the main effect of electrostatics on domain size was due to the difference in dipole magnitudes between domain and surround, rather than their absolute values. With these assumptions, we set $p_{sur} = 0$, and replaced p_{dom} with $\Delta\phi\epsilon\epsilon_0A_L$, where $\Delta\phi$ is the electrostatic potential difference between the domain and surround and A_L is the area per lipid in the domain. Our final simplification was to assume that domains are far enough apart that inter-domain energies are negligible. The total intra- and interleaflet contributions can then be rewritten as:

$$V_{intra} = \frac{N_D}{4\pi\epsilon\epsilon_0} \sum_{i=1}^{N_L^{top}-1} \sum_{j=i+1}^{N_L^{top}} \left(\frac{(\Delta\phi\epsilon\epsilon_0A_L)^2}{\|\vec{r}_{ij}\|^3} \right), \quad (A.10)$$

$$V_{inter} = \frac{N_D}{4\pi\epsilon\epsilon_0} \sum_{i=1}^{N_L^{top}} \sum_{j=1}^{N_L^{bot}} \left(\frac{3(h\Delta\phi\epsilon\epsilon_0A_L)^2}{\|\vec{r}_{ij}\|^5} - \frac{(\Delta\phi\epsilon\epsilon_0A_L)^2}{\|\vec{r}_{ij}\|^3} \right), \quad (A.11)$$

where N_L^{top} and N_L^{bot} now refer to lipid dipoles within a single domain.

In the continuum limit, as described in the main text, the discrete summations are replaced by integrals:

$$V_{intra} = N_D \frac{1}{2} \frac{N_L^2}{4\pi\epsilon\epsilon_0} \int_a^{2R_D} \frac{(\Delta\phi\epsilon\epsilon_0 A_L)^2}{r^3} P(r, R_D) dr, \quad (A.12)$$

$$V_{inter} = N_D \frac{N_L^2}{4\pi\epsilon\epsilon_0} \int_0^{2R_D} \left[\frac{3(h\Delta\phi\epsilon\epsilon_0 A_L)^2}{(h^2 + r^2)^{5/2}} - \frac{(\Delta\phi\epsilon\epsilon_0 A_L)^2}{(h^2 + r^2)^{3/2}} \right] P(r, R_D) dr, \quad (A.13)$$

where $a = 2\sqrt{A_L/\pi}$ (the lower limit of the V_{intra} integral) is the distance of closest approach between two dipoles, N_L is the total number of lipid dipoles in one domain leaflet, and $P(r, R_D)$ is the distribution of dipole separation distances derived as follows. Considering a vector $\mathbf{v} = (r \sin \theta, r \cos \theta)$ contained within the domain, the probability density for all vectors of magnitude r is proportional both to r , and to the overlap area A of two disks of radius R_D whose centers are separated by a distance r , as shown by the shaded region in Figure B.15 A. This area is given by:

$$\begin{aligned} A(r, R_D) &= 4 \int_{r/2}^{R_D} dx \sqrt{R_D - x^2} \\ &= 2R_D^2 \tan^{-1} \left[\frac{R_D}{r} \sqrt{4 - \left(\frac{r}{R_D}\right)^2} \right] - \frac{rR_D}{2} \sqrt{4 - \left(\frac{r}{R_D}\right)^2}. \end{aligned} \quad (B.14)$$

The normalized probability distribution is then given by:

$$\begin{aligned}
 P(r, R_D) &= \frac{rA(r, R_D)}{\int_0^{2R_D} rA(r, R_D)dr} \\
 &= \frac{r}{\pi R_D^3} \left\{ 4R_D \tan^{-1} \left[\frac{R_D}{r} \sqrt{4 - (r/R_D)^2} \right] - r \sqrt{4 - (r/R_D)^2} \right\}. \quad (A. 15)
 \end{aligned}$$

Figure B.15 *B* plots Equation B.15 for $R_D = 10$ (solid blue line), as well as a histogram of pair-distances obtained by generating 10^4 random points within a disk of radius 10, demonstrating the validity of the analytical solution.

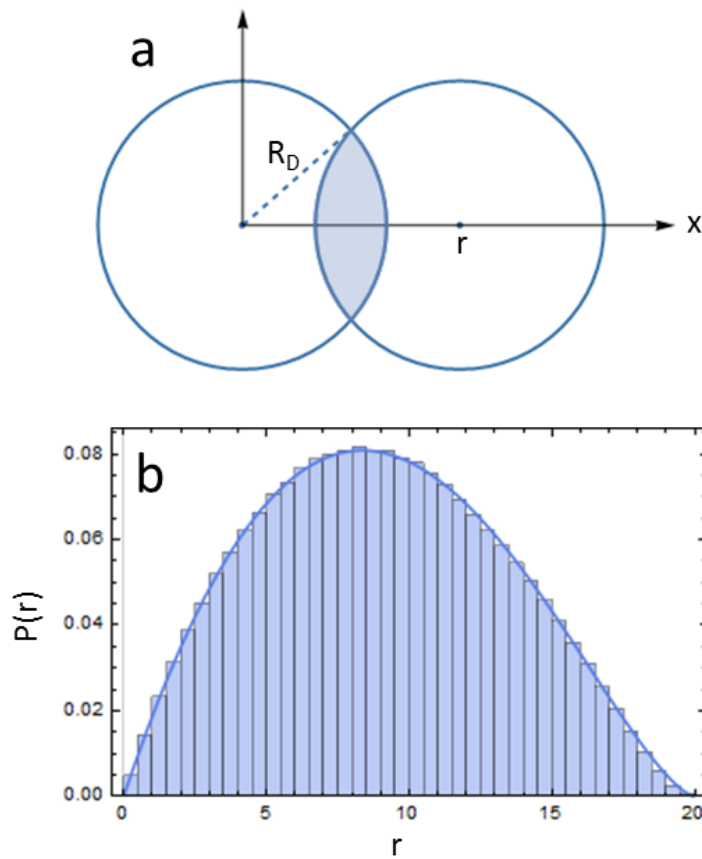


Figure B.15. Analytical solution for the pair-distance distribution function of a disk. *a*, geometric interpretation of the density of vectors of magnitude r contained within a disk of radius R_D as an overlap area. *b*, Equation S15 plotted for $R_D = 10$ (solid blue line) and a corresponding pair-distance histogram generated from random points as described in the text, demonstrating the validity of the analytical solution.

For the calculations presented in the main text, we chose parameters reasonable for model bilayer membranes: $\varepsilon = 8$, $A_L = 60 \text{ \AA}^2$, $h = 3 \text{ nm}$, $\Delta\phi = 0.1$ or 0.2 V , and total domain area $\alpha = \pi 30^2 \text{ \mu m}^2$, corresponding to a single domain with a 30 \mu m radius.

In addition to the dipole continuum model discussed in the main text, we also calculated equilibrium domain sizes using three related models:

1. Modeling more explicitly the SANS experiment, we calculated the energetically favorable domain size for circular domains within a 60 nm diameter spherical vesicle; domain and surrounding membrane were assigned continuous dipole distributions with dipole potentials of 1 V and 0.9 V respectively, giving a dipole difference $\Delta\phi = 0.1$ V, or $\Delta\phi = 0.2$ V as in the isolated domain continuum model of the main text. Monte Carlo sampling was then used to calculate the distance distributions within domain and surround and between domain and surround, from which the electrostatic potential was calculated. The total domain area was fixed at 40% of the vesicle surface for this and the remaining two models.

2. We calculated the energetically favorable domain size as in the main text, but using discrete dipoles rather than the continuum limit. Within the circular domain, dipoles were assigned a magnitude of $0.1 V * (\epsilon\epsilon_0 A_L) = 1.0617$ Debye and distributed approximately uniformly using a Matlab script (23).

3. We replaced the above discrete dipoles with discrete positive and negative charges calculated from the aforementioned dipole magnitude, assuming a dipole length of 1.23 Å (a typical carbonyl bond length), yielding charge magnitudes of $\sim 0.18 e^-$. In each model, h , ϵ and A_L are the same as in the main text.

For all models, we fixed the total domain area and chose reasonable values for membrane electrostatic properties, varying only the number of domains. For the three models discussed above, computational limitations prevent accessing arbitrarily large domain sizes: for these models, we chose a bilayer surface area corresponding to a ~ 60 nm diameter vesicle that resulted in a single “macrodomain” limit of $R_d \sim 40$ nm (to facilitate comparison, we also applied the continuum model to this case).

All four models reveal a sharp transition from many smaller domains, to a single large domain that is limited only by the vesicle size, with increasing line tension. Moreover, for all four models this transition occurs at similar values of line tension. Slight differences between the models are also evident. For example, treating the systems continuously versus discretely results in small differences in the line tension value required to induce the domain size transition. The stepwise nature of the vesicle continuum model arises due to computational limitations in fully sampling all possible numbers of domains, and the steps in the discrete models arises from the constraint that the number of dipoles per domain must be an integer value. Nevertheless, the four models are in good agreement over the range of accessible parameter space. Especially importantly, each model predicts an abrupt domain size transition at intermediate line tensions, indicating that continuum models can faithfully reproduce the discretization of real membranes. Despite differences in the models, we find that the vesicle model produces results which agree with the simplified continuum model, thus supporting the analysis methodologies and assumptions of the main text (namely that the main electrostatic effect is due to differences in electrostatic potential between domain and surround such that the surround can be ignored in favor of more simple analyses involving a flat, isolated domain). These models also show that the nature of the two competing interactions of line tension and electrostatics favor an abrupt

transition in domain size and are not sensitive to the exact values used in the models until they take on unphysically large or small values (Figures B.16 and B.17 described further below).

Model Sensitivity

As mentioned in the main text, the precise line tension value where the domain size transition occurs is sensitive to the choice of model parameters. However, the finding of an abrupt transition is robust, occurring for a wide range of parameter values as described below.

We investigated the influence of the parameters displayed in Table B.4 by independently varying each parameter in the calculations. Figure B.16 plots the equilibrium domain radius as a function of the line tension for different values of dielectric constant, ϵ , while holding other parameter values (A_L , h and $\Delta\phi$) constant as displayed in Table B.4.

Table B.4. Parameters used in the dipole-dipole repulsion simulations.

Parameter	Canonical value	Description
ϵ	8	Dielectric constant
$\Delta\phi$	0.2 V	Dipole potential difference between domain and surrounding phases
h	3.0 nm	Separation distance between dipole planes in opposing leaflets
A_L	60 Å ²	Area per dipole

For convenience, we label the line tension value where the domain size transition occurs as λ^* . We found that, upon increasing the dielectric constant, the line tension value required to form macroscopic domains decreased, as displayed in Figure B.16. This result is physically intuitive, since an increase in the dielectric constant should decrease the influence of electrostatics.

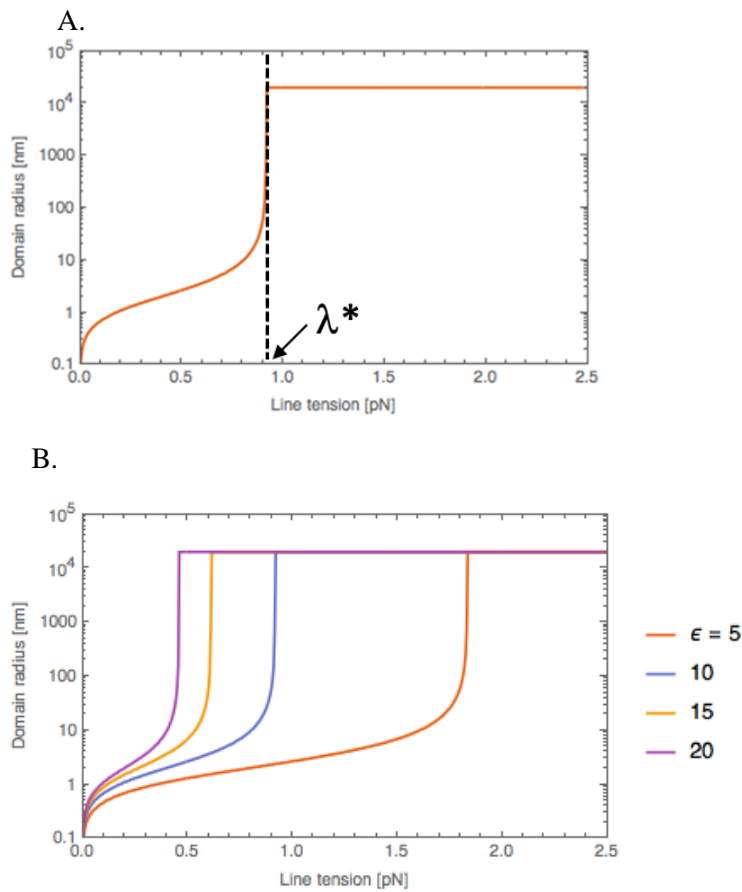


Figure B.16. Sensitivity of the continuum model to dielectric constant. (A) For a given parameter set, we define λ^* as the line tension value where domain size reaches its limiting macroscopic value. (B) Increasing the dielectric constant over a reasonable range while holding other parameter values constant at their “canonical” values (Table B.4) shifts the domain size transition to lower line tensions as the effects of electrostatics are diminished. In addition, we calculated λ^* as a function of each individual parameter— ϵ , A_L , h and $\Delta\phi$ —while all other parameters were fixed, with the results shown in Figure B.17.

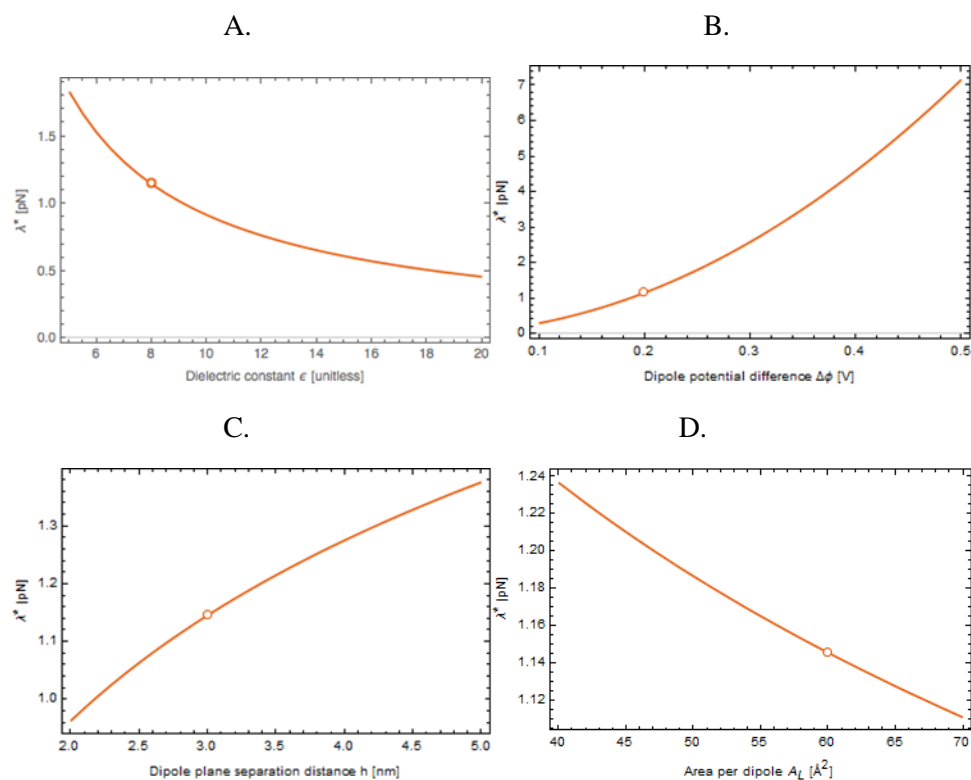


Figure B.17. Sensitivity of the continuum model to parameter values. (A) Varying the dielectric constant, ϵ , (at fixed dipole magnitude) over the range 5-20 results in critical line tension values from 0.45-1.8 pN (4-fold variation). (B) Varying the dipole potential difference, $\Delta\phi$, over the range 0.1-0.5 V results in critical line tension values from 0.2-7 pN (35-fold variation). (C) Varying the dipole plane separation distance, h , over the range 2-5 nm results in critical line tension values from 0.9-1.4 pN (1.5-fold variation). (D) Varying the area per dipole, A_L , over the range 40-70 \AA^2 results in critical line tension values from 1.1-1.25 pN (1.1-fold variation). Open circle depicts λ^* , corresponding to the canonical parameters.

B.9. References

1. Angelova, M., S. Soleau, and P. Méléard. 1992. Preparation of giant vesicles by external AC electric fields. Kinetics and applications. *Trends Colloid* 89: 127–131.
2. Morales-Pennington, N.F., J. Wu, E.R. Farkas, S.L. Goh, T.M. Konyakhina, J.Y. Zheng, W.W. Webb, and G.W. Feigenson. 2010. GUV preparation and imaging: minimizing artifacts. *Biochim. Biophys. Acta.* 1798: 1324–32.
3. Esposito, C., A. Tian, S. Melamed, C. Johnson, S.-Y. Tee, and T. Baumgart. 2007. Flicker spectroscopy of thermal lipid bilayer domain boundary fluctuations. *Biophys. J.* 93: 3169–3181.
4. Heberle, F.A., R.S. Petruzielo, J. Pan, P. Drazba, N. Kučerka, R.F. Standaert, G.W. Feigenson, and J. Katsaras. 2013. Bilayer thickness mismatch controls domain size in model membranes. *J. Am. Chem. Soc.* 135: 6853–9.
5. Heberle, F.A., V.N.P. Anghel, and J. Katsaras. 2015. Scattering from phase-separated vesicles. I. An analytical form factor for multiple static domains. *J. Appl. Crystallogr.* 48: 1391–1404.
6. Feigin, L.A., and D.I. Svergun. 1987. *Structure Analysis by Small-Angle X-Ray and Neutron Scattering.* Boston, MA: Springer US.
7. Kučerka, N., J. Pencser, J.N. Sachs, J.F. Nagle, and J. Katsaras. 2007. Curvature Effect on the Structure of Phospholipid Bilayers. *Langmuir.* 23: 1292–1299.
8. Denbigh, K. 1981. *The Principles of Chemical Equilibrium.* Fourth. Cambridge University Press.
9. Heberle, F.A., J. Wu, S.L. Goh, R.S. Petruzielo, and G.W. Feigenson. 2010. Comparison of three ternary lipid bilayer mixtures: FRET and ESR reveal nanodomains. *Biophys. J.* 99: 3309–18.
10. Konyakhina, T.M., J. Wu, J.D. Mastroianni, F.A. Heberle, and G.W. Feigenson. 2013. Phase diagram of a 4-component lipid mixture: DSPC/DOPC/POPC/chol. *Biochim. Biophys. Acta.* 1828: 2204–14.
11. Petruzielo, R.S., F.A. Heberle, P. Drazba, J. Katsaras, and G.W. Feigenson. 2013. Phase behavior and domain size in sphingomyelin-containing lipid bilayers. *Biochim. Biophys. Acta.* 1828: 1302–13.
12. Zhao, J., J. Wu, F. a Heberle, T.T. Mills, P. Klawitter, G. Huang, G. Costanza, and G.W. Feigenson. 2007. Phase studies of model biomembranes: complex behavior of DSPC/DOPC/cholesterol. *Biochim. Biophys. Acta.* 1768: 2764–76.
13. Sodt, A.J., M.L. Sandar, K. Gawrisch, R.W. Pastor, and E. Lyman. 2014. The Molecular Structure of the Liquid-Ordered Phase of Lipid Bilayers. *J. Am. Chem. Soc.* 136: 725–732.
14. Ackerman, D.G., and G.W. Feigenson. 2015. Multiscale modeling of four-component lipid mixtures: Domain composition, size, alignment, and properties of the phase

- interface. *J. Phys. Chem. B.* 119.
15. Henriksen, J.R., and J.H. Ipsen. 2002. Thermal undulations of quasi-spherical vesicles stabilized by gravity. *Eur. Phys. J. E. Soft Matter.* 9: 365–74.
 16. Gracià, R.S., N. Bezlyepkina, R.L. Knorr, R. Lipowsky, and R. Dimova. 2010. Effect of cholesterol on the rigidity of saturated and unsaturated membranes: fluctuation and electrodeformation analysis of giant vesicles. *Soft Matter.* 6: 1472.
 17. Méléard, P., T. Pott, H. Bouvrais, and J.H. Ipsen. 2011. Advantages of statistical analysis of giant vesicle flickering for bending elasticity measurements. *Eur. Phys. J. E.* 34: 116.
 18. Pécrcéaux, J., H.G. Döbereiner, J. Prost, J.F. Joanny, and P. Bassereau. 2004. Refined contour analysis of giant unilamellar vesicles. *Eur. Phys. J. E.* 13: 277–290.
 19. Lakowicz, J.R. 2006. *Principles of Fluorescence Spectroscopy Principles of Fluorescence Spectroscopy.* .
 20. Mills, T.T., G.E.S. Toombes, S. Tristram-Nagle, D.-M. Smilgies, G.W. Feigenson, and J.F. Nagle. 2008. Order parameters and areas in fluid-phase oriented lipid membranes using wide angle X-ray scattering. *Biophys. J.* 95: 669–81.
 21. Alwarawrah, M., J. Dai, and J. Huang. 2010. A Molecular View of the Cholesterol Condensing Effect in DOPC Lipid Bilayers. *J. Phys. Chem. B.* 114: 7516–7523.
 22. McConnell, H.M. 1991. Structures and Transitions in Lipid Monolayers at the Air-Water Interface. *Annu. Rev. Phys. Chem.* 42: 171–195.
 23. <http://stackoverflow.com/questions/28567166/uniformly-distribute-x-points-inside-a-circle>

Appendix C

Supporting Material for Chapter 4:

Calculation of Ld/Lo line tension from lipid pairwise interactions*

Contents

C.1 Additional information for derivation of eq. 7

C.2 Additional information for derivation of eq. 12

C.3 Parameter sensitivity

C.4 FRET Trajectory method

C.5 PSM phase boundaries

C.6 References

*R.D. Usery, S. Hiraki, G.W. Feigenson. 2018. Calculation of liquid-disordered/liquid-ordered line tension from pairwise lipid interactions. *Biophysical Journal* (submitted)

C.1 Additional information for derivation of eq. 7

$$\begin{aligned}
\tau &= -\frac{1}{2}n'(X_A^{Lo} - X_A^{Ld})(X_B^{Lo} - X_B^{Ld})\phi_{AB} - \frac{1}{2}n'(X_B^{Lo} - X_B^{Ld})(X_C^{Lo} - X_C^{Ld})\phi_{BC} \\
&\quad - \frac{1}{2}n'(X_A^{Lo} - X_A^{Ld})(X_C^{Lo} - X_C^{Ld})\phi_{AC} \\
&\quad (\because) \{ (X_A^{Lo}X_B^{Lo}) + (X_A^{Ld}X_B^{Ld}) - 2(X_A^LX_B^L) \} \phi_{AB} \\
&= \{ X_A^{Lo}(X_B^{Lo} - X_B^L) + X_A^{Ld}(X_B^{Ld} - X_B^L) \} \phi_{AB} \\
&= \frac{1}{2} \{ X_A^{Lo}(X_B^{Lo} - X_B^{Ld}) - X_A^{Ld}(X_B^{Lo} - X_B^{Ld}) \} \phi_{AB}
\end{aligned} \tag{C.1}$$

C.2 Additional information for derivation of eq. 12.

We can express Gibbs energy of a ternary system model as:

$$\begin{aligned}
\frac{G}{n} &= N_A \varepsilon_{AA} + N_B \varepsilon_{BB} + N_C \varepsilon_{CC} \\
&\quad + \frac{RT}{n} \left\{ N_A \ln \left(\frac{N_A}{N_A + N_B + N_C} \right) + N_B \ln \left(\frac{N_B}{N_A + N_B + N_C} \right) \right. \\
&\quad \left. + N_C \ln \left(\frac{N_C}{N_A + N_B + N_C} \right) \right\} + \frac{N_A^2 N_B}{(N_A + N_B + N_C)^2} \phi_{AB} \\
&\quad + \frac{N_A N_B^2}{(N_A + N_B + N_C)^2} \phi_{AB} + \frac{N_B^2 N_C}{(N_A + N_B + N_C)^2} \phi_{BC} \\
&\quad + \frac{N_B N_C^2}{(N_A + N_B + N_C)^2} \phi_{BC} + \frac{N_A N_C^2}{(N_A + N_B + N_C)^2} \phi_{CA} \\
&\quad + \frac{N_A^2 N_C}{(N_A + N_B + N_C)^2} \phi_{CA} + \frac{N_A N_B N_C}{(N_A + N_B + N_C)^2} (\phi_{AB} + \phi_{BC} + \phi_{AC}).
\end{aligned} \tag{C.2}$$

Thus, the chemical potential of component A, μ_A , in a certain phase as expressed by our model is

$$\begin{aligned}
\mu_A &= \left(\frac{\partial G}{\partial N_A} \right)_{T,P,N_B, \text{and } C} \\
&= n\varepsilon_{AA} + RT \ln \left(\frac{N_A}{N} \right) + \left(2 \frac{N_A N_B}{N^2} - 2 \frac{N_A^2 N_B}{N^3} + \frac{N_B^2}{N^2} - 2 \frac{N_A N_B^2}{N^3} \right) n\phi_{AB} \\
&\quad + \left(2 \frac{N_A N_C}{N^2} - 2 \frac{N_A^2 N_C}{N^3} + \frac{N_C^2}{N^2} - 2 \frac{N_A N_C^2}{N^3} \right) n\phi_{CA} \\
&\quad + \left(-2 \frac{N_B^2 N_C}{N^3} - 2 \frac{N_B N_C^2}{N^3} \right) n\phi_{CB} \\
&\quad + \left(\frac{N_B N_C}{N^2} - \frac{2N_A N_B N_C}{N^3} \right) n(\phi_{AB} + \phi_{CB} + \phi_{CA}) \\
&= n\varepsilon_{AA} + RT \ln X_A + (2X_A X_B - 2X_A^2 X_B + X_B^2 - 2X_A X_B^2) n\phi_{AB} \\
&\quad + (2X_A X_C - 2X_A^2 X_C + X_C^2 - 2X_A X_C^2) n\phi_{CA} + (-2X_B X_C^2 - 2X_C X_B^2) n\phi_{BC} \\
&\quad + (X_B X_C - 2X_A X_B X_C) n(\phi_{AB} + \phi_{CB} + \phi_{CA}) \tag{C.3} \\
&= n\varepsilon_{AA} + RT \ln X_A + (2X_A X_B - 2X_A^2 X_B + X_B^2 - 2X_A X_B^2 + X_B X_C - 2X_A X_B X_C) n\phi_{AB} \\
&\quad + (2X_A X_C - 2X_A^2 X_C + X_C^2 - 2X_A X_C^2 + X_B X_C - 2X_A X_B X_C) n\phi_{CA} \\
&\quad + (-2X_B^2 X_C - 2X_B X_C^2 + X_B X_C - 2X_A X_B X_C) n\phi_{CB} \\
(\because) \quad \mu_A &= \left(\frac{\partial G}{\partial N_A} \right)_{T,P,N_B, \text{and } C} \\
&= n\varepsilon_{AA} + RT \ln X_A + X_B(1 - X_A) n\phi_{AB} + X_C(1 - X_A) n\phi_{CA} \\
&\quad - X_B X_C n\phi_{CB} \\
(\because) \quad \mu_B &= \left(\frac{\partial G}{\partial N_B} \right)_{T,P,N_A, \text{and } C} \\
&= n\varepsilon_{BB} + RT \ln X_B + X_A(1 - X_B) n\phi_{AB} + X_C(1 - X_B) n\phi_{CB} \\
&\quad - X_A X_C n\phi_{CA}
\end{aligned}$$

$$\begin{aligned}
(\because) \quad \mu_C &= \left(\frac{\partial G}{\partial N_C} \right)_{T,P,N_A, \text{and } B} \\
&= n\varepsilon_{CC} + RT \ln X_C + X_A(1 - X_C)n\phi_{CA} + X_B(1 - X_C)n\phi_{CB} \\
&\quad - X_A X_B n\phi_{AB} \\
(\because) \quad 2X_A X_B - 2X_A^2 X_B + X_B^2 - 2X_A X_B^2 + X_B X_C - 2X_A X_B X_C \\
&= 2X_A X_B(1 - X_A - X_B) - 2X_A X_B X_C + X_B X_C + X_B^2 \\
(\because) \quad - 2X_B^2 X_C - 2X_B X_C^2 + X_B X_C - 2X_A X_B X_C \\
&= -2X_B X_C(X_B + X_C) + X_B X_C - 2X_A X_B X_C = -X_B X_C
\end{aligned}$$

Under chemical equilibrium condition; $\mu_i^{Lo} = \mu_i^{Ld}$, we gain

$$\begin{aligned}
RT \ln X_A^{Lo} - RT \ln X_A^{Ld} &= RT \ln K_{P(A)}^{Lo/Ld} \\
&= \left\{ (X_B(1 - X_A))^{Ld} - (X_B(1 - X_A))^{Lo} \right\} n\phi_{AB} \\
&\quad + \left\{ (X_C(1 - X_A))^{Ld} - (X_C(1 - X_A))^{Lo} \right\} n\phi_{AC} \\
&\quad - \left\{ (X_B X_C)^{Ld} - (X_B X_C)^{Lo} \right\} n\phi_{BC} ,
\end{aligned}$$

$$\begin{aligned}
RT \ln K_{P(B)}^{Lo/Ld} &= \left\{ (X_A(1 - X_B))^{Ld} - (X_A(1 - X_B))^{Lo} \right\} n\phi_{AB} \\
&\quad + \left\{ (X_C(1 - X_B))^{Ld} - (X_C(1 - X_B))^{Lo} \right\} n\phi_{CB} \\
&\quad - \left\{ (X_A X_C)^{Ld} - (X_A X_C)^{Lo} \right\} n\phi_{CA}
\end{aligned} \tag{C.4}$$

$$\begin{aligned}
RT \ln K_{P(C)}^{Lo/Ld} &= \left\{ (X_A(1 - X_C))^{Ld} - (X_A(1 - X_C))^{Lo} \right\} n\phi_{CA} \\
&\quad + \left\{ (X_B(1 - X_C))^{Ld} - (X_B(1 - X_C))^{Lo} \right\} n\phi_{CB}
\end{aligned}$$

C.3 Parameter Sensitivity

We examined parameter sensitivity by systematically fixing each interaction energy at values from +10X to -10X the actual values and allowing the others to vary in the calculation, Tables S1-6. These values reflect how much each interaction energy responds (dy) to a change in the others (dx). Accordingly values in the tables are dy/dx . No nonlinear effects were observed as expected.

Table C.1 DSPC/DOPC/chol parameter sensitivity

		dx		
		DSPC-DOPC	DOPC-chol	DSPC-chol
dy	DSPC-DOPC	1.0	0.1	0.1
	DOPC-chol	10.4	1.0	0.6
	DSPC-chol	17.9	1.7	1.0

Table C.2 DSPC/POPC/chol parameter sensitivity

		dx		
		DSPC-POPC	POPC-chol	DSPC-chol
dy	DSPC-POPC	1.0	0.1	0.1
	POPC-chol	9.3	1.0	0.6
	DSPC-chol	16.3	1.8	1.0

Table C.3 bSM/DOPC/chol parameter sensitivity

		dx		
		bSM-DOPC	DOPC-chol	bSM-chol
dy	bSM-DOPC	1.0	0.1	0.1
	DOPC-chol	6.7	1.0	0.5
	bSM-chol	12.9	1.9	1.0

Table C.4 bSM/POPC/chol parameter sensitivity

		<i>dx</i>		
		bSM-POPC	POPC-chol	bSM-chol
<i>dy</i>	bSM-POPC	1.0	0.3	0.1
	POPC-chol	3.1	1.0	0.4
	bSM-chol	7.7	2.4	1.0

Table C.5 PSM/DOPC/chol parameter sensitivity

		<i>dx</i>		
		PSM-DOPC	DOPC-chol	PSM-chol
<i>dy</i>	PSM-DOPC	1.0	0.4	0.1
	DOPC-chol	2.9	1.0	0.4
	PSM-chol	7.2	2.5	1.0

Table C.6 PSM/POPC/chol parameter sensitivity

		<i>dx</i>		
		PSM-POPC	POPC-chol	PSM-chol
<i>dy</i>	PSM-POPC	1.0	0.4	0.1
	POPC-chol	2.8	1.0	0.4
	PSM-chol	7.2	2.5	1.0

C.4 FRET trajectory method

We prepared samples by rapid solvent exchange (RSE) (1) along a compositional trajectory that traversed the two-phase region and measured FRET at room temperature. Decreased FRET is observed in the two-phase region when donor and acceptor probes partition into different phases. Phase boundaries are identified from the FRET curve shape as previously described (2–4). Briefly, boundaries are defined by the intersection of linear fits in the regions neighboring an abrupt change in the FRET signal. An internal normalization in the FRET profiles was used to correct variations between samples, such as small differences in sample concentration (5). The fluorescence emission of the acceptor stimulated by the energy transfer of the donor, FRET, was normalized by the donor and acceptor emission in each sample.

C.5 PSM/DOPC/chol and PSM/POPC/chol boundaries

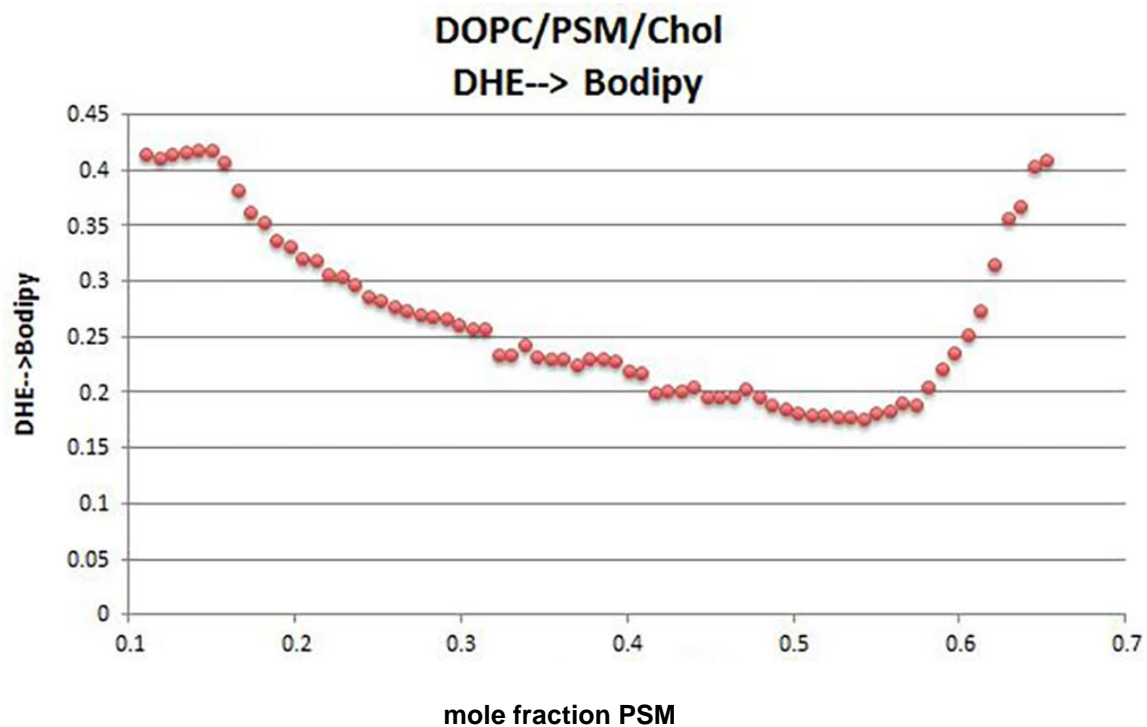


Figure C.1 PSM/DOPC/chol trajectory. Intensity of FRET from DHE to Bodipy along the trajectory through points A and B of Figure 4.1.

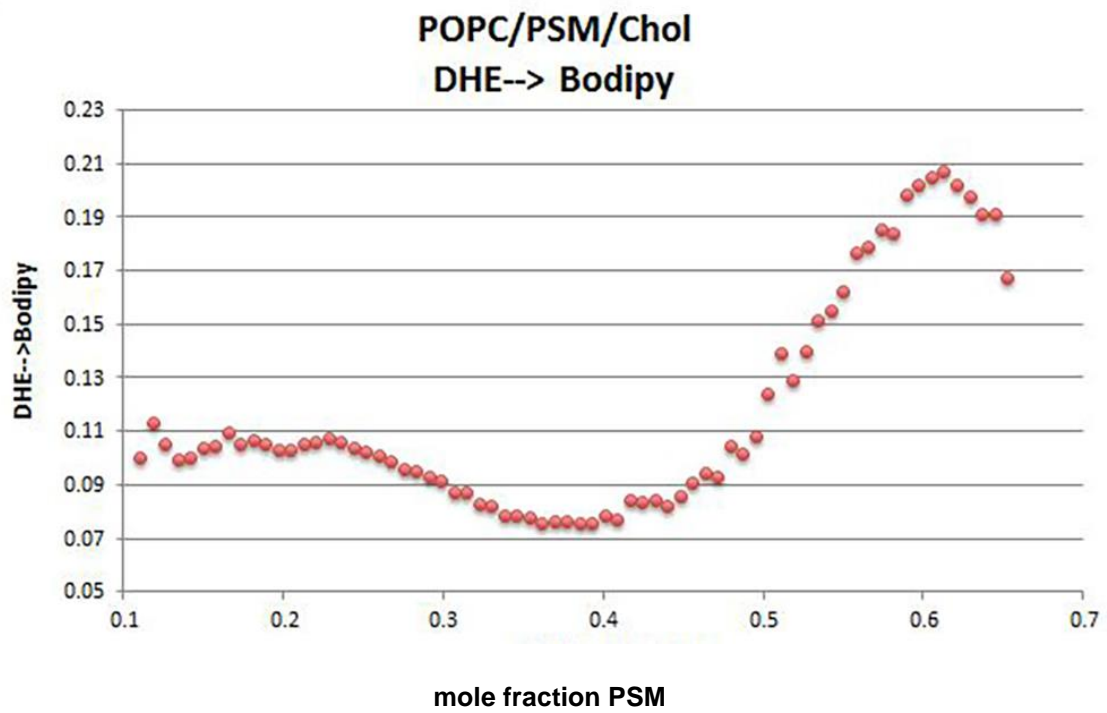


Figure C.2 PSM/POPC/chol trajectory. Intensity of FRET from DHE to Bodipy along the trajectory through points A and B of Figure 4.1.

C.6 References

1. Buboltz, J.T., and G.W. Feigenson. 1999. A novel strategy for the preparation of liposomes: rapid solvent exchange. *Biochim. Biophys. Acta - Biomembr.* 1417: 232–245.
2. Zhao, J., J. Wu, F. a Heberle, T.T. Mills, P. Klawitter, G. Huang, G. Costanza, and G.W. Feigenson. 2007. Phase studies of model biomembranes: complex behavior of DSPC/DOPC/cholesterol. *Biochim. Biophys. Acta.* 1768: 2764–76.
3. Konyakhina, T.M., J. Wu, J.D. Mastroianni, F.A. Heberle, and G.W. Feigenson. 2013. Phase diagram of a 4-component lipid mixture: DSPC/DOPC/POPC/chol. *Biochim. Biophys. Acta.* 1828: 2204–14.
4. Petruzielo, R.S., F.A. Heberle, P. Drazba, J. Katsaras, and G.W. Feigenson. 2013. Phase behavior and domain size in sphingomyelin-containing lipid bilayers. *Biochim. Biophys. Acta.* 1828: 1302–13.
5. Buboltz, J.T. 2007. Steady-state probe-partitioning fluorescence resonance energy transfer: A simple and robust tool for the study of membrane phase behavior. *Phys. Rev. E - Stat. Nonlinear, Soft Matter Phys.* 76: 1–7.

Appendix D:

Bending rigidity of membranes containing nanodomains is determined by the percolating phase

ABSTRACT In a model system in which domains nanometers in size are produced, the mechanical properties of the bilayer as the area fractions of phases change may have implications for the behavior of the cell plasma membrane. We have varied the phase fraction and measured the bending modulus with and without a transmembrane protein component. The continuous phase in this kind of model mixture determines the bending modulus of the membrane, and measurements with peptide are consistent with the partition coefficient.

Membrane rafts are thought to serve as a means to organize the plasma membrane in accomplishing its many necessary functions- signal transduction chief among those. Though the composition of the plasma membrane (PM) is such that phase separation is probable, the time and length scales on which domains would exist are experimentally intractable in cells. We can model raft + non-raft behavior in cells with mixtures of high melting temperature (HighT_m) lipid, low melting temperature (LowT_m) lipid and cholesterol (chol).

In addition to facilitating signaling events, the plasma membrane must also bend. The size scale of bending for budding events is likely greater than the domain size.

Lateral heterogeneity of the plasma membrane is on the size scale of tens of nanometers (1–6) while 40 nm vesicles are among the smallest produced by the cell (7). We can model this nanoscopic heterogeneity with the mixture DSPC/POPC/chol. The region in which Ld and Lo coexist in this mixture is shown in Figure D.1. Domains in this mixture have been found to be 15 nm in diameter.(8, 9)

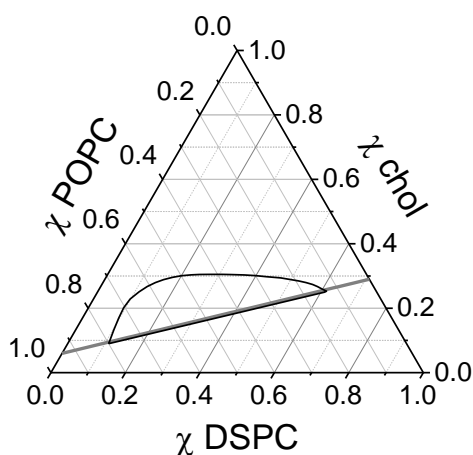


FIGURE D.1. Two-phase region of DSPC/POPC/chol. Compositions measured in this work fall on the line (in grey).

We measured the bending modulus with flicker spectroscopy as previously described. Briefly, GUVs were prepared by gentle hydration (10) and fluctuations at the GUV equator were observed by phase contrast microscopy. Fluctuation spectra from GUV contours were used to calculate the bending modulus through the relationship

$$\langle |u(q)|^2 \rangle = \frac{k_B T}{\kappa q^4 + \sigma q^2}, \quad (1)$$

where $u(q)$ is the displacement normal to the membrane, $q = (qx, qy)$ is the wave vector corresponding to the displacement, k_B is the Boltzmann constant, T is the absolute temperature, κ is the bending modulus, and σ is membrane tension. All measurements were carried out at room temperature.

For a macroscopic mixture, there are few domains per vesicle, resulting in an inhomogeneous, potentially non-spherical vesicle not suitable for this measurement. For a nanoscopic mixture, domains are below the resolution limit and thus the GUV equator should be representative of the entire vesicle. In DSPC/POPC/chol, a mixture where nanoscopic phase separation has been observed (8, 11–13), we were interested in behavior of membranes with coexisting Ld and Lo. We measured bending moduli traversing the two-phase region where the nanoscopic domains change with composition from Lo domains in an Ld matrix, to Ld domains in an Lo matrix. Interestingly, there appear to be two linear regimes, Fig. D.2A. The intersection occurs near where phase fractions are nearly equal. The low slope linear regime appears to coincide with Ld being the percolating phase, and the regime of greater slope at higher DSPC fraction appears to coincide with Lo being the percolating phase. In the DSPC/DOPC/chol mixture, the percolation point was found to be at phase fraction of 0.5 (9). We investigated percolation at $\rho=0.2$ and found the percolating phase changed between $x_{\text{DSPC}} = .3$ and $x_{\text{DSPC}} = .4$, or the phase fraction of Lo at approximately 0.5. This two-regime behavior suggests that the percolating phase dominates the rigidity measurement when phases coexist. Others have measured the bending moduli of mixtures of this type and found an intermediate bending modulus. (14)

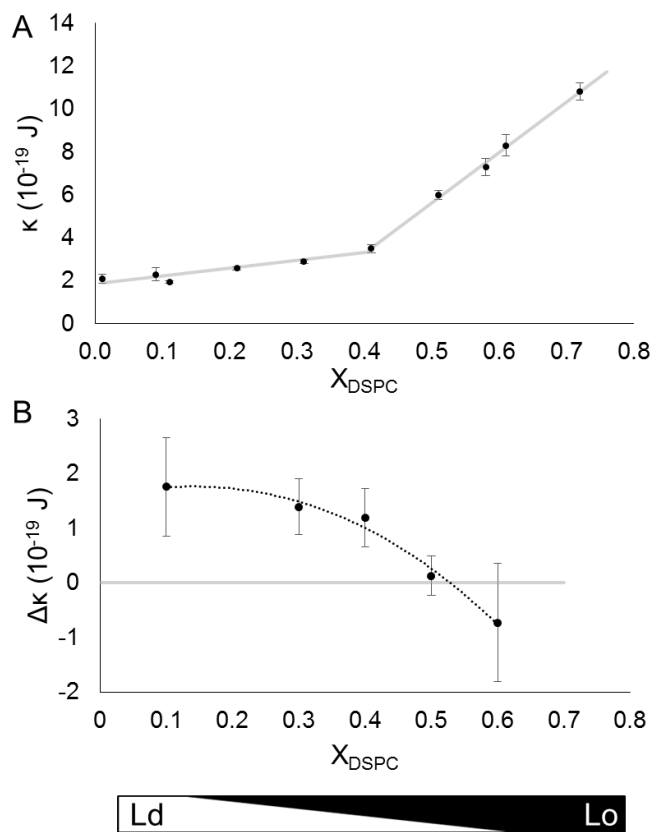


FIGURE D.2 A) DSPC/POPC/chol bending moduli (in 10^{-19} J) traversing the two-phase region. The compositions lie on the line in Fig 1. B) Difference in bending moduli of lipid-only DSPC/POPC/chol and DSPC/POPC/chol with 2 mol% GWALP is zero when Lo is the percolating phase. Bar depicts phase fraction corresponding to the x-axis.

From Fig D.2B it can be seen that the difference between the lipid only and peptide-containing mixture goes to 0 after the percolation point. This finding is consistent with previous findings regarding the large preference of the peptide for the Ld phase and bending modulus measurements with a small amount of peptide in the Lo

phase (15). Previous findings regarding partitioning and incorporation of the peptide led to our decision to confine our measurements with peptide to the two phase region.

Our investigation of bending moduli following the lower tieline of the two phase region for the nanoscopic mixture DSPC/POPC/chol revealed that the percolating phase dominates the bending modulus measurements. Domains along this tieline are nanometers in size. Rather than smoothly increasing along this line through compositional space, which might be expected in the absence of phase separation, we observed two linear regimes. Moving from all Ld to all Lo along the lower tieline, the bending modulus increases gradually and then more sharply. The change appears to occur near where Ld and Lo have equal area fraction, likely the percolation point. The measured values also did not follow what would be predicted based on the change in the mean thickness of the bilayer (8). Fig. D.2 suggests that effects beyond the length scale of nanometers are significant in the consideration of bilayer mechanical properties. This finding may have implications for the behavior of nanodomains in the cell plasma membrane.

References

1. Raghupathy, R., A.A. Anilkumar, A. Polley, P.P. Singh, M. Yadav, C. Johnson, S. Suryawanshi, V. Saikam, S.D. Sawant, A. Panda, Z. Guo, R.A. Vishwakarma, M. Rao, and S. Mayor. 2015. Transbilayer lipid interactions mediate nanoclustering of lipid-anchored proteins. *Cell*. 161: 581–94.
2. Roduit, C., F.G. van der Goot, P. De Los Rios, A. Yersin, P. Steiner, G. Dietler, S. Catsicas, F. Lafont, and S. Kasas. 2008. Elastic membrane heterogeneity of living cells revealed by stiff nanoscale membrane domains. *Biophys. J.* 94: 1521–32.
3. Dinic, J., P. Ashrafzadeh, and I. Parmryd. 2013. Actin filaments attachment at the plasma membrane in live cells cause the formation of ordered lipid domains. *Biochim. Biophys. Acta - Biomembr.* 1828: 1102–1111.
4. Pralle, A., P. Keller, E.L. Florin, K. Simons, and J.K. Hörber. 2000. Sphingolipid-cholesterol rafts diffuse as small entities in the plasma membrane of mammalian cells. *J. Cell Biol.* 148: 997–1008.
5. Sezgin, E., I. Levental, S. Mayor, and C. Eggeling. 2017. The mystery of membrane organization: composition, regulation and roles of lipid rafts. *Nat. Rev. Mol. Cell Biol.* 18: 361–374.
6. Moss, F.R., I. Id, and S.G. Boxer. 2016. Atomic Recombination in Dynamic Secondary Ion Mass Spectrometry Probes Distance in Lipid Assemblies: A Nanometer Chemical Ruler Graphical Abstract HHS Public Access. *J Am Chem Soc.* 138: 16737–16744.
7. Raposo, G., and W. Stoorvogel. 2013. Extracellular vesicles: exosomes, microvesicles, and friends. *J. Cell Biol.* 200: 373–83.
8. Heberle, F.A., R.S. Petruzielo, J. Pan, P. Drazba, N. Kučerka, R.F. Standaert, G.W. Feigenson, and J. Katsaras. 2013. Bilayer thickness mismatch controls domain size in model membranes. *J. Am. Chem. Soc.* 135: 6853–9.

9. Enoki, T.A., F.A. Heberle, and G.W. Feigenson. 2018. FRET Detects the Size of Nanodomains for Coexisting Liquid-Disordered and Liquid-Ordered Phases. *Biophys. J.* 114.
10. Akashi, K., H. Miyata, H. Itoh, and K. Kinoshita. 1996. Preparation of giant liposomes in physiological conditions and their characterization under an optical microscope. *Biophys. J.* 71: 3242–50.
11. Heberle, F.A., J. Wu, S.L. Goh, R.S. Petruzielo, and G.W. Feigenson. 2010. Comparison of three ternary lipid bilayer mixtures: FRET and ESR reveal nanodomains. *Biophys. J.* 99: 3309–18.
12. Konyakhina, T.M., J. Wu, J.D. Mastroianni, F.A. Heberle, and G.W. Feigenson. 2013. Phase diagram of a 4-component lipid mixture: DSPC/DOPC/POPC/chol. *Biochim. Biophys. Acta.* 1828: 2204–14.
13. de Wit, G., J.S.H. Danial, P. Kukura, and M.I. Wallace. 2015. Dynamic label-free imaging of lipid nanodomains. *Proc. Natl. Acad. Sci. U. S. A.* 112: 12299–303.
14. Nickels, J.D., X. Cheng, B. Mostofian, C. Stanley, B. Lindner, F.A. Heberle, S. Perticaroli, M. Feyngenson, T. Egami, R.F. Standaert, J.C. Smith, D.A.A. Myles, M. Ohl, and J. Katsaras. 2015. Mechanical Properties of Nanoscopic Lipid Domains. *J. Am. Chem. Soc.* 137: 15772–15780.
15. Usery, R.D., T.A. Enoki, S.P. Wickramasinghe, V.P. Nguyen, D.G. Ackerman, D. V. Greathouse, R.E. Koeppe, F.N. Barrera, and G.W. Feigenson. 2018. Membrane Bending Moduli of Coexisting Liquid Phases Containing Transmembrane Peptide. *Biophys. J.* 114: 2152–2164.